Magnetization Dynamics in Lithographically Patterned $Ni_{80}Fe_{20}/Ir_{20}Mn_{80}$ Exchange-Biased Square Elements

by

Haitian Xu
B.A., University of Cambridge, 2004
B.Sc., University of Victoria, 2009

A Thesis Submitted in Partial Fulfillment of the
Requirements for the Degree of

MASTER OF SCIENCE

in the Department of Physics and Astronomy

Magnetization Dynamics in Lithographically Patterned $Ni_{80}Fe_{20}/Ir_{20}Mn_{80}$ Exchange-Biased Square Elements

by

Haitian Xu
B.A., University of Cambridge, 2004
B.Sc., University of Victoria, 2009

Supervisory Committee

Dr. Byoung-Chul Choi, Supervisor
(Department of Physics and Astronomy)

Dr. Rogério de Sousa, Departmental Member
(Department of Physics and Astronomy)

Supervisory Committee

Dr. Byoung-Chul Choi, Supervisor
(Department of Physics and Astronomy)

Dr. Rogério de Sousa, Departmental Member
(Department of Physics and Astronomy)

ABSTRACT

The magnetic properties and crystal texture of micron-sized, lithographically patterned ferromagnetic/antiferromagnetic (FM/AF) exchange-coupled elements supporting vortex remanent magnetization states were characterized using experimental and numerical modeling techniques. $10\,\mu\text{m}\times10\,\mu\text{m}$ square elements consisting of $Ni_{80}Fe_{20}/Ir_{20}Mn_{80}$ bilayers prepared on silicon and glass substrates using e-beam lithography and magnetron sputtering were thermomagnetically annealed under various in-plane cooling fields to induce exchange bias. Longitudinal and time-resolved Kerr effect microscopy were employed to measure the quasi-static hysteresis and dynamic response, while X-ray diffraction analysis was used to probe their crystal texture under different deposition and substrate conditions. The FM layer was found to be critical for the development of the necessary texture and spin alignment in the AF for creating interfacial exchange-bias. The exchange-bias field was found to significantly alter the magnetic behavior of the samples, leading to the stabilization of the vortex structure and asymmetric hysteresis loop shift in the quasi-static regime, as well as precessional frequency reduction of the bottom domain in the dynamic regime. Numerical simulations showed good qualitative agreement with both experimental observations and existing literature, and revealed the origin of the precessional frequency reduction as the different spin-wave eigenmodes excited by different remanent magnetization states.

Contents

List of Tables

List of Figures

ACKNOWLEDGEMENTS

I would like to sincerely thank:

Prof. Byoung-Chul Choi, for being the most accommodating, patient, knowledgeable and awesome supervisor.

Prof. Thanassis Speliotis, for his critical assistance with fabrication.

Jonathan Rudge and Joseph Kolthammer, for their support and knowledge, without which I would have gotten nowhere.

Albert Santoni and Rennie Gardner, for their contributions to all aspects of my research.

Prof. Rogério de Sousa and Prof. Pavel Kovtun, for their insight and guidance.

Chris Secord, Nicolas Braam and Neil Honkanen, for their technical assistance.

As for the causes of magnetic movements, referred to in the schools of philosophers to the four elements and to prime qualities, these we leave for roaches and moths to prey upon.

– William Gilbert, *De Magnete*, 1600 A.D.

Chapter 1

Micromagnetics

1.1 Introduction

Magnetism has been known to man since antiquity, a fascinating fact considering its complex nature was not unveiled until the advent of twentieth-century quantum mechanics. Extensive investigation of magnetic systems began in the 1940s when the work of Harvard and MIT physicists led to the invention of magnetic-core memory, the predominant form of computer random access memory (RAM) for the next two decades. The numerous studies on magnetic systems to date have been motivated by their ever-expanding industrial applications [1, 2], particularly since the discovery of the giant magnetoresistance (GMR) effect [3], as well as interests in the fundamental physics at play.

A magnetic system can be characterized by its metastable *equilibrium states* and the *dynamic transitions* between them. Continuing demands for higher storage density and lower access times in magnetoelectronic devices have made critical the thorough understanding of magnetization dynamics in magnetic media at sub-micron/sub-nanosecond scales. Challenges arise however, as dynamic processes typically differ significantly from quasi-static ones [4], and the interplay between low dimensionality and magnetism produce novel effects in laterally confined structures unseen in bulk.

To this end, the focus of my research has been on understanding quasi-static and dynamic behaviors of micron-sized, lithographically patterned magnetic squares with exchange-bias[1] using a variety of experimental and theoretical techniques.

[1]The importance of exchange-bias will be addressed in Chapter 2.

1.1.1 Thesis Overview

This thesis is structured as follows

Chapter 1 contains a brief general introduction, followed by the presentation of the micromagnetic model, including quasi-static equilibrium conditions, uniform reversal, precession dynamics and numerical techniques.

Chapter 2 introduces the exchange bias phenomenology.

Chapter 3 gives a detailed account of the experimental methodology, including sample preparation and characterization techniques.

Chapter 4 contains the bulk of the experimental data from my research.

Chapter 5 analyses and expands upon the experimental data using numerical simulations.

Chapter 6 summarizes the main findings of my research and gives concluding remarks.

1.2 Micromagnetic Free Energy

Quantitative analysis of sub-micron/sub-nanosecond magnetic processes requires a theoretical model with sufficient spatiotemporal resolution. In this section, I will introduce this phenomenological micromagnetic model [5, 6, 7] based on a free energy[2] minimization approach, whereby the energy expressions associated with various magnetic interactions in a ferromagnet body are individually derived and subsequently combined to obtain the static equilibrium conditions through variational minimization.

1.2.1 Magnetic Moments

Elementary particles carry intrinsic magnetic dipole moments $\boldsymbol{\mu}_S$ and $\boldsymbol{\mu}_L$ associated with their spin and orbital angular momenta, $\mathbf{S}$ and $\mathbf{L}$. For an isolated electron with no orbital contribution, this relationship is characterized by the spin gyromagnetic ratio γ_S

[2]The relation between energy E and free energy F is given by $F = E - TS$, where S is the entropy. For $T \ll T_c$, the distinction between energy and free energy is not important [8].

$$\boldsymbol{\mu}_S = -\gamma_S \mathbf{S}, \quad \text{where}$$
$$\gamma_S = g_S \frac{\mu_B}{\hbar}, \quad \mu_B = \frac{|e|\hbar}{2m_e}. \tag{1.1}$$

where $g \simeq 2$ is the dimensionless spin g-factor and μ_B is the Bohr magneton, the natural unit for expressing magnetic dipole moments.

1.2.2 The Continuum Framework

Consider a ferromagnetic body with volume V discretized into unit cells $\mathrm{d}V_{\mathbf{r}}$, with position vector $\mathbf{r} \in V$. Each unit cell contains N elementary magnetic moments $\boldsymbol{\mu}_i$ $(i = 1, ..., N)$ from individual electrons. We assume the following for the dimensions of $\mathrm{d}V_{\mathbf{r}}$:

1. It is small enough such that all $\boldsymbol{\mu}_i$ within each unit cell are uniformly aligned and can be treated a single 'macrospin'.

2. It is large enough such that changes in the total unit cell magnetic moment $\Delta \sum_{i=1}^{N} \boldsymbol{\mu}_i$ between adjacent unit cells is sufficiently small for $\sum_{i=1}^{N} \boldsymbol{\mu}_i$ to be regarded as a continuous quantity.

We now define the magnetization vector field $\mathbf{M}(\mathbf{r})$, equal to the magnet moment per unit cell volume

$$\mathbf{M}(\mathbf{r}) = \frac{\sum_{i=1}^{N} \boldsymbol{\mu}_i}{\mathrm{d}V_{\mathbf{r}}}. \tag{1.2}$$

Under the above assumptions, $\mathbf{M}(\mathbf{r})$ (or $\mathbf{M}(\mathbf{r}, t)$ in the dynamic case) is a *continuous* variable with *constant* magnitude, denoted saturation magnetization M_s, equal to the maximum magnetization when all spins are aligned. Magnetic interactions are expressed in terms of this vector field in our micromagnetic framework.

1.2.3 Exchange Interaction

Ferromagnetism and Weiss Molecular Field

Of all magnetic interactions, the most critical is exchange. It is, after all, the very mechanism responsible for ferromagnetism. In most materials, thermal agitation plays

a predominant role on the arrangement of magnetic dipole moments, leading to either paramagnetic (magnetic permeability μ slightly greater than unity[3]) or diamagnetic (μ slightly less than unity) behavior, corresponding to random orientations of elementary magnetic moments with little overall magnetization. On the other hand, certain metals such as iron, cobalt and nickel possess particular band structures that enable exchange interaction, some 10^4 times stronger than electron dipolar interaction, to overcome thermal energy and align spins over atomic scale. These materials consequently exhibit very large magnetic permeability ($\mu \sim 10^3$) and strong spontaneous magnetization of saturation order, a property referred to as *ferromagnetism*. In the context of micromagnetic theory, exchange interaction is an energy term that favors the formation of small, uniformly magnetized regions known as *magnetic domains*.

The existence of magnetic domains was first postulated by Pierre-Ernest Weiss, who explained the observed temperature dependence of magnetic susceptibility in ferromagnetic materials (Fig. 1.1) using his classical formulation of a molecular field [9].

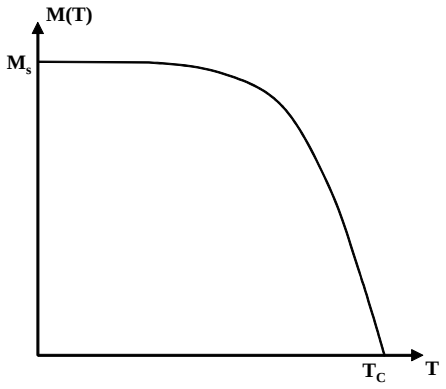

Figure 1.1: Typical temperature dependence of spontaneous magnetization in a ferromagnet.

Weiss' phenomenological explanation was justified decades later by Werner Heisenberg [10] on the basis of the quantum theory of exchange interaction. An outline derivation based on the Hartree-Fock approximation [11] is presented in Appendix A.

The Heisenberg Model

The Heisenberg Hamiltonian derived in Appendix A is given by

[3]Vacuum permeability $\mu_0 = 1$ in the CGS unit system.

$$\mathcal{H}_{\text{ex}} = -J \sum_{k \neq k'} \mathbf{S_k} \cdot \mathbf{S_{k'}}, \tag{1.3}$$

where S_k is the total unpaired electron spin for the atom situated at a lattice site $\mathbf{k}$, and J is a material constant known as the *nearest neighbor exchange integral*. The sum is carried over nearest neighbors only.

A particular material can exhibit either ferromagnetism or anti-ferromagnetism depending on the sign of J:

$J > 0$**: ferromagnetism**, energetically favours alignment of electrons spins over atomic scale.

$J < 0$**: anti-ferromagnetism**, energetically favours anti-parallel alignment of neighboring spins.

Exchange Energy

Assuming exchange interaction dominates on the unit cell level such that nearest neighbor spins are almost parallel, we can expand (1.3) in the small-angle limit

$$\begin{aligned} W &\simeq -2JS^2 \sum_{\text{nnbr}} \cos\theta_{kk'} \simeq -2JS^2 \sum_{\text{nnbr}} (1 - \frac{1}{2}\theta_{kk'}^2) \\ &= const. + JS^2 \sum_{\text{nnbr}} \theta_{kk'}^2 \simeq const. + JS^2 \sum_{\text{nnbr}} (\mathbf{m}_{k'} - \mathbf{m}_k)^2, \end{aligned} \tag{1.4}$$

where $\mathbf{m}_k = \mathbf{S}_k/S$ is the magnetic unit vector field at site k, and $\theta_{kk'}$ is the angle between $\mathbf{m}_k$ and $\mathbf{m}_{k'}$ which, for small angles, is approximately given by

$$|\theta_{kk'}| \simeq |\mathbf{m}_k - \mathbf{m}_{k'}|. \tag{1.5}$$

Since variation in $\mathbf{m}$ between adjacent unit cells k and k' is small, we can express $\mathbf{m}_{k'} - \mathbf{m}_k$ in terms of a relative position vector $\mathbf{r}_{kk'} = \mathbf{r}_{k'} - \mathbf{r}_k$ and a continuous function $\mathbf{m}$

$$\mathbf{m}_{k'} - \mathbf{m}_k = \begin{pmatrix} \mathbf{r}_{kk'} \cdot \nabla m_x \\ \mathbf{r}_{kk'} \cdot \nabla m_y \\ \mathbf{r}_{kk'} \cdot \nabla m_z \end{pmatrix} = \mathbf{r}_{kk'} \cdot \nabla \mathbf{m}, \tag{1.6}$$

(1.4) can now be rewritten as

$$W \simeq const. + JS^2 \sum_{\text{nnbr}} [(\mathbf{r}_{kk'} \cdot \nabla m_x)^2 + (\mathbf{r}_{kk'} \cdot \nabla m_y)^2 + (\mathbf{r}_{kk'} \cdot \nabla m_z)^2]. \tag{1.7}$$

The exchange energy density $\mathcal{E}_{\text{ex}}$ can be obtained from (1.7) by summing over all kk' pairs under the assumption of a cubic lattice, and multiplying the result by the spin density n,

$$\mathcal{E}_{\text{ex}} = A_{\text{ex}}[(\nabla m_x)^2 + (\nabla m_y)^2 + (\nabla m_z)^2]. \tag{1.8}$$

The material constant A_{ex} is referred to as the *exchange stiffness*, commonly used to describe the strength of exchange interaction in ferromagnetic materials. Its relation to J is given by [12, chap. 1]

$$A_{\text{ex}} = \frac{1}{6} nJS^2 \sum_{\text{nnbr}} \Delta \mathbf{r}_{kk'}^2. \tag{1.9}$$

The summation in (1.9) can be particularized for a given lattice geometry. The exchange contribution to the total free energy can be found by integrating the energy density (1.8) over the entire volume occupied by the magnetic body

$$E_{\text{ex}} = \int_V A_{\text{ex}}[(\nabla m_x)^2 + (\nabla m_y)^2 + (\nabla m_z)^2] \, \mathrm{d}V. \tag{1.10}$$

Exchange energy contribution *isotropically* penalizes against inhomogeneities in magnetization, as evident from the *even-powered* gradient terms in (1.10).

1.2.4 Anisotropy

The coupling between magnetic energies and lattice structure as well as shape geometry in a ferromagnetic body can lead to *anisotropic effects*, with its magnetic moments having preferred minimum energy orientations in the absence of an external field. The origin of the anisotropy may be Maxwellian (e.g. shape anisotropy due to geometry-dependent demagnetizing field), or quantum mechanical (e.g. magnetocrystalline anisotropy via spin-orbit coupling). Similar to exchange, the anisotropy contribution can be introduced into our micromagnetic framework by means of a phenomenological free energy term

$$E_{\text{an}} = \int_V \mathcal{E}_{\text{an}}(\mathbf{m})\,\mathrm{d}V, \tag{1.11}$$

where $\mathcal{E}_{\text{an}}(\mathbf{m})$ is the anisotropy energy density and the unit vector field $\mathbf{m}$ is related to the magnetization vector field $\mathbf{M}$ by $\mathbf{M} = M_s\mathbf{m}$. Directions corresponding to the minima of this energy density are called magnetization *easy axes*, while directions corresponding to its maxima as referred to as magnetization *hard axes*.

Uniaxial Anisotropy Energy

If there exists only a single easy axis, the anisotropy is termed *uniaxial*. In this case, $\mathcal{E}_{\text{an}}(\mathbf{m})$ is rotationally symmetric, and depends only on the relative orientation between the easy axis and $\mathbf{m}$. Assuming the easy axis coincides with the cartesian axis z, and expressing $\mathbf{m} = (m_x, m_y, m_z)$ in spherical polar coordinates (θ, ϕ):

$$\begin{aligned} m_x &= \sin\theta\cos\phi \\ m_y &= \sin\theta\sin\phi \\ m_z &= \cos\theta, \end{aligned} \tag{1.12}$$

rotational symmetry implies that $\mathcal{E}_{\text{an}}(\mathbf{m})$ can be expanded as an even function of $m_z = \cos\theta$, or equivalently, $\sin\theta$:

$$\mathcal{E}_{\text{an}}(\mathbf{m}) = K_o + K_1\sin^2\theta + K_2\sin^4\theta + K_3\sin^6\theta + \ldots, \tag{1.13}$$

where K_n are the phenomenological anisotropy constants with dimensions of energy per unit volume (erg/cm^3). I shall limit my calculation to the case where the series expression truncates after the second term

$$\mathcal{E}_{\text{an}}(\mathbf{m}) \simeq K_o + K_1\sin^2\theta, \tag{1.14}$$

after dropping the constant term, the total anisotropy in (1.11) becomes

$$E_{\text{an}} = \int_V K_1[1 - (\mathbf{e}(\mathbf{r})\cdot\mathbf{m}(\mathbf{r}))^2]\,\mathrm{d}V. \tag{1.15}$$

where $\mathbf{e}(\mathbf{r})$ is the easy axis unit vector.

The nature of anisotropy depends on the sign of K_1. As shown in Fig. 1.2, when $K_1 > 0$, the two identical anisotropy energy minima lie along $\pm z$; when $K_1 < 0$,

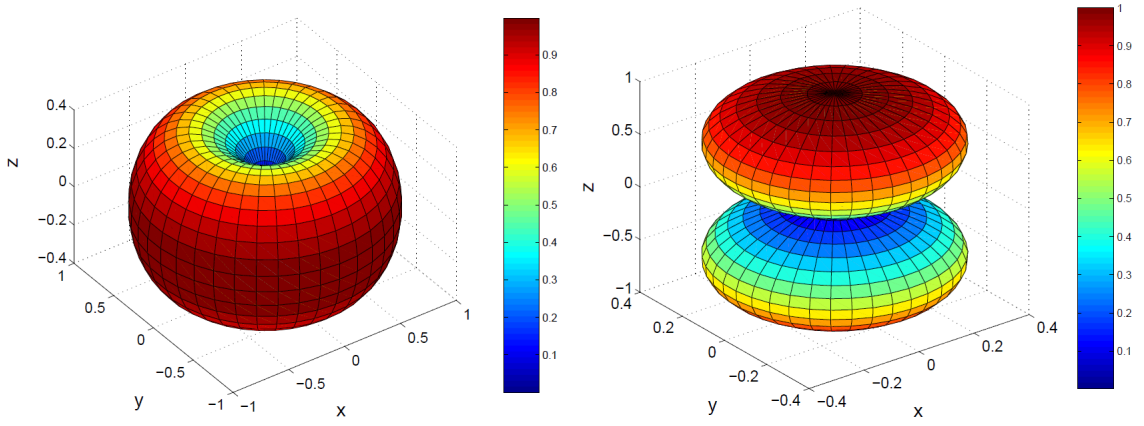

Figure 1.2: Uniaxial anisotropy energy distribution, from [12].

the energy minima lie along the $x - y$ plane. There exists more complex forms of anisotropy, but they will not be discussed here.

1.2.5 Magnetostatic Interactions

Magnetostatic interactions refer to long-range, dipolar interactions of the elementary magnetic moments with its own magnetization vector field (magnetostatic self-energy), as well as with an external field (Zeeman energy). Their contributions to the free energy functional can be described in terms of an appropriate magnetostatic field, $\mathbf{H}_{\text{demag}}$ or $\mathbf{H}_{\text{ext}}$.

Magnetostatic Self-Energy

The magnetostatic self-energy can be expressed in terms of the demagnetizing field $\mathbf{H}_{\text{demag}}$

$$E_{\text{demag}} = \int_{V_\infty} \frac{1}{2}\mu_o \mathbf{H}_{\text{demag}}^2 \, \mathrm{d}V, \tag{1.16}$$

where V_∞ indicates the entire space. (1.16) can be rewritten in terms of the magnetization vector field $\mathbf{M}$ as

$$E_{\text{demag}} = -\int_{V} \frac{1}{2}\mu_o \mathbf{H}_{\text{demag}} \cdot \mathbf{M} \, \mathrm{d}V. \tag{1.17}$$

by substituting $\mathbf{H}_{\text{demag}} = \mathbf{B}_{\text{demag}}/\mu_o - \mathbf{M}$ into (1.16), and taking note of the orthonormality between $\mathbf{H}_{\text{demag}}$ and $\mathbf{B}_{\text{demag}}$ over V_∞.

Zeeman Energy

Similar to magnetostatic self-energy, the energy contribution from an external field $\mathbf{H}_{\text{ext}}$ can be expressed as

$$E_{ext} = -\int_V \mu_o \mathbf{H}_{\text{ext}} \cdot \mathbf{M} \mathrm{d}V. \tag{1.18}$$

Note that the extra 1/2 in (1.17) arises from the *internal* nature of $\mathbf{H}_{\text{demag}}$.

1.2.6 Micromagnetic Equilibrium

By combining (1.10), (1.14), (1.17) and (1.18), we arrive at the complete expression for the free energy of a ferromagnetic body

$$\begin{aligned} G(\mathbf{m}, \mathbf{H}_{\text{ext}}) &= E_{\text{ex}} + E_{\text{an}} + E_{\text{demag}} + E_{\text{ext}} \\ &= \int_V \Big\{ A_{\text{ex}}[(\nabla m_x)^2 + (\nabla m_y)^2 + (\nabla m_z)^2] + K_o + K_1 \sin^2\theta + \\ &- \frac{1}{2}\mu_o \mathbf{H}_{\text{demag}} \cdot \mathbf{M} - \mu_o \mathbf{H}_{\text{ext}} \cdot \mathbf{M} \Big\} \, \mathrm{d}V \\ &= \int_V \Big[A_{\text{ex}} (\nabla \mathbf{m})^2 + \mathcal{E}_{\text{an}} - \frac{1}{2}\mu_o \mathbf{H}_{\text{demag}} \cdot \mathbf{M} - \mu_o \mathbf{H}_{\text{ext}} \cdot \mathbf{M} \Big] \, \mathrm{d}V. \end{aligned} \tag{1.19}$$

Equilibrium conditions can be derived by considering the vanishing first-order variation of this free energy

$$\delta G = G(\mathbf{m} + \delta\mathbf{m}) = 0, \tag{1.20}$$

subject to the constraint

$$|\mathbf{m} + \delta\mathbf{m}| = 1. \tag{1.21}$$

It can be shown [12, chap. 1] that

$$\begin{aligned} \delta G = &- \int_V \Big[2\nabla \cdot (A_{\text{ex}} \nabla \mathbf{m}) - \frac{\partial \mathcal{E}_{\text{an}}}{\partial \mathbf{m}} + \mu_o M_s (\mathbf{H}_{\text{demag}} + \mathbf{H}_{\text{ext}}) \Big] \cdot \delta\mathbf{m} \, \mathrm{d}V \\ &+ \int_{\partial V} \Big[2A_{\text{ex}} \frac{\partial \mathbf{m}}{\partial \mathbf{n}} \cdot \delta\mathbf{m} \Big] \, \mathrm{d}S = 0, \end{aligned} \tag{1.22}$$

where ∂V is the boundary of V and $\mathbf{n}$ is its surface normal. The constraint in (1.21) implies that the variation of the magnetic unit vector field is *rotational*, i.e.

$$\delta\mathbf{m} = \mathbf{m} \times \delta\boldsymbol{\theta}, \tag{1.23}$$

where $\delta\boldsymbol{\theta}$ represents an arbitrary elementary rotation. (1.22) thus becomes

$$\begin{aligned}\delta G = &\int_V \mathbf{m} \times \left[2\nabla \cdot (A_{\text{ex}}\nabla\mathbf{m}) - \frac{\partial \mathcal{E}_{an}}{\partial \mathbf{m}} + \mu_o M_s(\mathbf{H}_{demag} + \mathbf{H}_{ext})\right] \cdot \delta\boldsymbol{\theta}\, \mathrm{d}V \\ &+ \int_{\partial V} \left[2A_{\text{ex}}\frac{\partial \mathbf{m}}{\partial \mathbf{n}} \times \mathbf{m}\right] \cdot \delta\boldsymbol{\theta}\, \mathrm{d}S = 0,\end{aligned} \tag{1.24}$$

which is only *identically zero* for arbitrary $\delta\theta$ if *both* integrands are zero. We therefore arrive at the following equilibrium conditions:

$$\begin{cases} \mathbf{m} \times \left[2\nabla \cdot (A_{\text{ex}}\nabla\mathbf{m}) - \dfrac{\partial \mathcal{E}_{\text{an}}}{\partial \mathbf{m}} + \mu_o M_s(\mathbf{H}_{\text{demag}} + \mathbf{H}_{\text{ext}})\right] = 0 \\ \left[2A_{\text{ex}}\dfrac{\partial \mathbf{m}}{\partial \mathbf{n}} \times \mathbf{m}\right]_{\partial V} = 0, \end{cases} \tag{1.25}$$

which can be simplified into[4]

$$\begin{cases} \mu_o \mathbf{M} \times \mathbf{H}_{\text{eff}} = 0, \\ \left.\dfrac{\partial \mathbf{m}}{\partial \mathbf{n}}\right|_{\partial V} = 0. \end{cases} \tag{1.26}$$

we introduce the **effective field**, $\mathbf{H}_{\text{eff}}$ in (1.26), which summarily describes all interactions acting on magnetization $\mathbf{M}$

$$\mathbf{H}_{\text{eff}} = \frac{2}{\mu_o M_s}\nabla \cdot (A_{\text{ex}}\nabla\mathbf{m}) - \frac{1}{\mu_o M_s}\frac{\partial \mathcal{E}_{\text{an}}}{\partial \mathbf{m}} + \mathbf{H}_{\text{demag}} + \mathbf{H}_{\text{ext}}. \tag{1.27}$$

(1.26) is known as **Brown's Equations**, and define the conditions of equilibrium. The first equation states that the torque exerted on the magnetization by the effective field must be zero at equilibrium; the second equation states that the magnetization must not have any component perpendicular to the surface of the ferromagnetic body. Note that Brown's equations are *nonlinear*, since $\mathbf{H}_{\text{eff}}$ contains a functional dependence on $\mathbf{M}$. In general (1.26) is solved numerically (see section 1.4.3).

[4]Here we make use of the fact that $\partial\mathbf{m}/\partial\mathbf{n}$ is always orthogonal to $\mathbf{m}$.

1.2.7 Domain Configuration in Ferromagnetic Squares

As previously stated, magnetic domains are small regions with uniform magnetic alignment. In large ferromagnetic bodies, there exist multiple domains of different orientations separated by domain walls, in which the magnetic moments between the two domains are matched through rotation, as illustrated in Fig. 1.3.

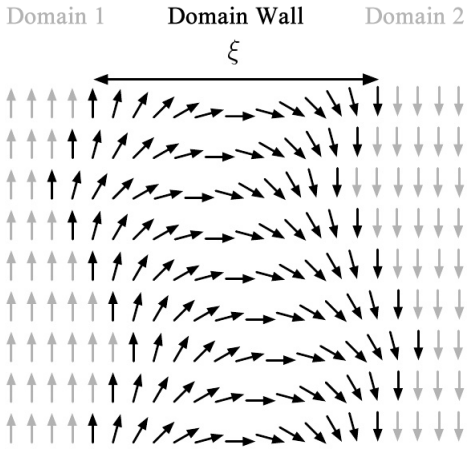

Figure 1.3: Illustration of magnetic domains separated by an in-plane Néel domain wall.

The equilibrium domain configuration of a particular ferromagnetic body arises out of the competition between its various energy constituents. The tendency of exchange interaction to align magnetic moments is counteracted by anisotropy and demagnetizing fields, which depend respectively on the crystal structure and shape geometries. In addition, interactions operate over different *length scales*:

The exchange length $l_{\mathbf{ex}}$ is the characteristic length scale over which exchange interaction prevails, and the magnetization is uniform,

$$l_{\mathrm{ex}} = \sqrt{\frac{2A_{\mathrm{ex}}}{\mu_o M_s^2}}. \tag{1.28}$$

For typical magnetic recording material, $l_{\mathrm{ex}} \simeq 5 - 10\,\mathrm{nm}$ [13]. Within the micromagnetic framework, it is important to ensure that the unit cell is smaller than, or at least comparable to l_{ex}, in order for the macrospin assumption to remain valid and the modelp realistic.

The domain wall width ξ is determined by the balance between exchange and magnetocrystalline anisotropy energies, and is typically in the 10-100 nm range [13],

$$\xi = \pi\sqrt{\frac{A_{\rm ex}}{K}}, \tag{1.29}$$

where K is the magnetocrystalline anisotropy constant.

Consider a laterally confined ferromagnetic thin film[5] with uniform magnetization, as illustrated in Fig. 1.4(a). The large magnetostatic self-energy of the surface poles results in a demagnetizing field that divides the film into two domains with anti-parallel orientations and roughly half the total energy (Fig. 1.4(b)). Subdivision will continue as long as the energy reduction in each case is greater than the energy required for the formation of the extra domain wall (Fig. 1.4(c)). Fig. 1.4(d)-(e) represent an energetically viable alternative division process, with no magnetic poles and zero magnetostatic energy. These are called *closure domain* configurations, in reference to the closure of the magnetic flux circuit within the body.

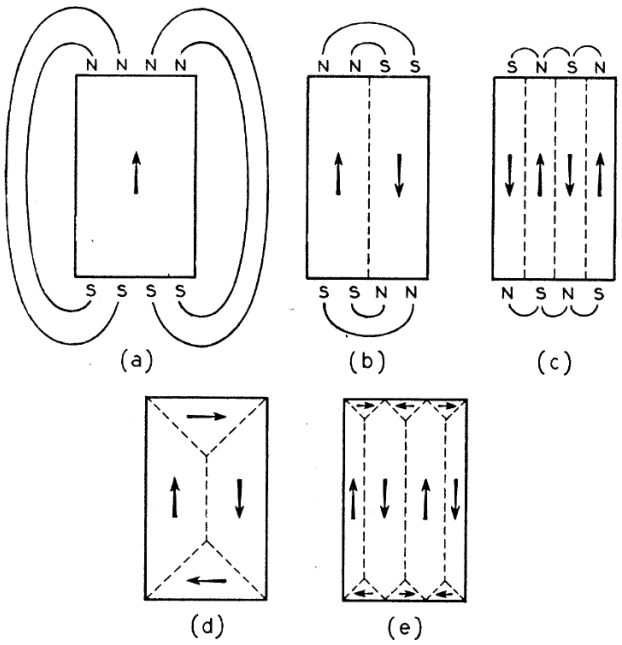

Figure 1.4: Domain configuration in laterally confined structures, from Kittel [8].

In square-shaped thin films of small lateral dimensions (100 nm to 10 μm) and negligible magnetocrystalline anisotropy, the competition between exchange interaction and magnetostatic energies under the influence of sample geometry can stabilize a vortex closure domain state with fourfold symmetry [14, 15], as illustrated in Fig. 1.5(a).

[5]We assume thickness of the order of $l_{\rm ex}$ and uniform magnetization depth profile.

The four equal triangular closure domains are separated by nominally 90° Néel domain walls with gradually changing magnetization which meet at the center. The shape anisotropy keeps all spins in-plane, except in a small region near the center, where the large angle variation of the domain wall magnetization is overcome by exchange interaction, and the magnetization is pushed out of plane [16] as illustrated in Fig. 1.5(b). The vortex core dimension is of the order of exchange length [17]. This state is commonly referred to as the **flux-closed Landau state**, in recognition to the original theoretical work on ferromagnetism carried out by Landau and Lifshitz [5].

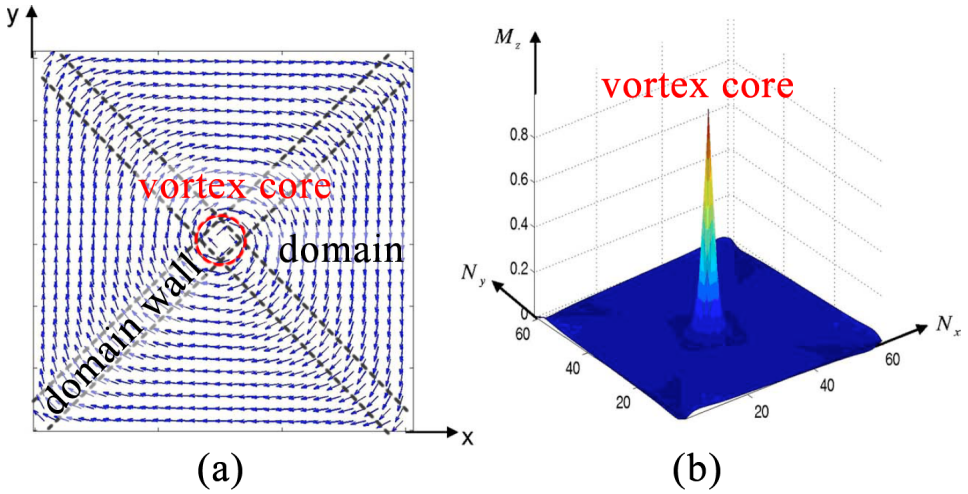

Figure 1.5: Closure domain vortex magnetization profile in ferromagnetic squares. (a) in-plane magnetization profile, (b) out-of-plane magnetization profile. From Yan et al. [15].

With an analytically simple vortex structure, low stray fields (hence minimum interaction between adjacent elements) and 4-fold degeneracy[6], the Landau state is an excellent candidate for both high-speed, high-density device integration and theoretical studies, and will constitute a substantial part of my work.

1.3 The Dynamic Equation

An outline derivation of the dynamic equation governing the temporal evolution of magnetization will be given in the section in order to complete the micromagnetic

[6]Up/down vortex core polarity as well as clockwise/counterclockwise chirality, see Bohlens et al. [18].

framework. The analysis herein follows the precession model proposed in 1935 by Landau and Lifshitz [5] and includes Gilbert's subsequent modification [19].

1.3.1 Gyromagnetic Precession

As previously stated in (1.1), the spin angular momentum $\mathbf{S}$ of an electron and its associated spin magnetic moment $\boldsymbol{\mu}_S$ are related through the gyromagnetic ratio[7]

$$\boldsymbol{\mu} = -\gamma \mathbf{S}. \tag{1.30}$$

An external field $\mathbf{H}$ exerts a torque $\boldsymbol{\Gamma}$ on the magnetic moment $\boldsymbol{\mu}$, causing a change in its spin angular momentum $\mathbf{S}$

$$\frac{\mathrm{d}\mathbf{S}}{\mathrm{d}t} = \boldsymbol{\mu} \times \mathbf{H}, \tag{1.31}$$

substituting (1.30) into (1.31), we obtain

$$\frac{\mathrm{d}\boldsymbol{\mu}}{\mathrm{d}t} = -\gamma \boldsymbol{\mu} \times \mathbf{H}. \tag{1.32}$$

(1.32) describes the precession of the electron spin magnetic moment around the external field. The frequency of precession is called the *Larmor frequency* and is given by

$$f_L = \frac{\gamma H}{2\pi}, \tag{1.33}$$

(1.32) can be re-written for the unit cell in the micromagnetic framework. Recalling (1.2), we have

$$\begin{aligned} \frac{1}{\mathrm{d}V_{\mathbf{r}}} \frac{\mathrm{d} \sum_{i=1}^{N} \boldsymbol{\mu}_i}{\mathrm{d}t} &= -\gamma \frac{\sum_{i=1}^{N} \boldsymbol{\mu}_i}{\mathrm{d}V_{\mathbf{r}}} \times \mathbf{H} \\ \Rightarrow \frac{\partial \mathbf{M}}{\partial t} &= -\gamma \mathbf{M} \times \mathbf{H}. \end{aligned} \tag{1.34}$$

1.3.2 The Landau-Lifshitz Equation

(1.34) is a continuum gyromagnetic precession equation for the magnetization vector field $\mathbf{M}$. By replacing $\mathbf{H}$ with the effective field $\mathbf{H}_{\text{eff}}$ from (1.27), we arrive at the

[7] The subscript S will be omitted henceforth for simplicity.

Landau-Lifshitz (LL) equation

$$\frac{\partial \mathbf{M}}{\partial t} = -\gamma \mathbf{M} \times \mathbf{H}_{\text{eff}}. \tag{1.35}$$

(1.35) is essentially the same as (1.34), except that it takes into account the various magnetic interactions in the system through $\mathbf{H}_{\text{eff}}$. It reduces to the first Brown's equation in (1.26) in the static limit.

According to (1.35), $\mathbf{M}$ precesses about the effective field indefinitely. In reality, intrinsic and extrinsic dissipative processes damp out the precession over time. These damping effects can be phenomenologically introduced into (1.35) in several different ways. Landau and Lifshitz originally suggested a damping torque which pushes the magnetization towards the effective field. This modifies the LL equation into

$$\frac{\partial \mathbf{M}}{\partial t} = -\gamma \mathbf{M} \times \mathbf{H}_{\text{eff}} - \frac{\lambda}{M_s} \mathbf{M} \times (\mathbf{M} \times \mathbf{H}_{\text{eff}}), \tag{1.36}$$

where $\lambda > 0$ is a phenomenological material constant.

1.3.3 The Landau-Lifshitz-Gilbert Equation

A principally different approach was proposed by William Gilbert, who, following a Lagrangian approach, noted that a general way of introducing dissipative effects into the dynamic equation is to add to the Lagrangian a suitable Rayleigh dissipation function proportional to the time derivatives of the generalized coordinates $\mathbf{M}(\mathbf{r}, t)$ [19]. Specifically, he introduced the following torque term (see Fig. 1.6)

$$\frac{\alpha}{M_s} \mathbf{M} \times \frac{\partial \mathbf{M}}{\partial t}, \tag{1.37}$$

where $\alpha > 0$ is the phenomenological Gilbert damping constant.

The modified LL equation became known as the *Landau-Lifshitz-Gilbert* (LLG) equation

$$\frac{\partial \mathbf{M}}{\partial t} = -\gamma \mathbf{M} \times \mathbf{H}_{\text{eff}} + \frac{\alpha}{M_s} \mathbf{M} \times \frac{\partial \mathbf{M}}{\partial t}, \tag{1.38}$$

which can be rearranged into a more convenient form

$$\frac{\partial \mathbf{M}}{\partial t} = -\frac{\gamma}{1+\alpha^2} \mathbf{M} \times \mathbf{H}_{\text{eff}} - \frac{\gamma \alpha}{(1+\alpha^2) M_s} \mathbf{M} \times (\mathbf{M} \times \mathbf{H}_{\text{eff}}). \tag{1.39}$$

(1.36) and (1.39) appear to be of identical mathematical form:

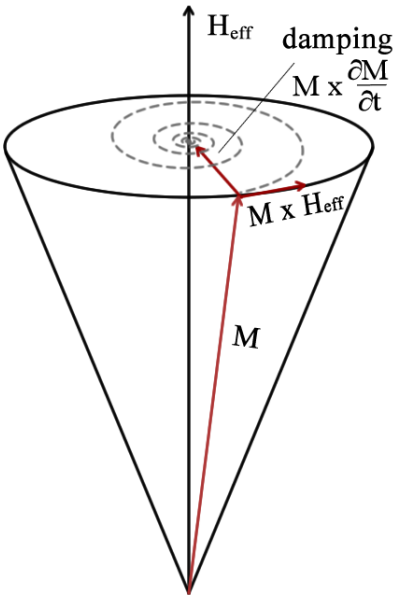

Figure 1.6: Schematic of LLG precession.

$$\begin{aligned} \gamma &\leftrightarrow \frac{\gamma}{1+\alpha^2} \\ \lambda &\leftrightarrow \frac{\gamma\alpha}{1+\alpha^2}, \end{aligned} \tag{1.40}$$

but the two equations actually express entirely different physics and are only identical in the limit of zero damping ($\alpha \to \frac{\lambda}{\gamma}$ as $\alpha \to 0$.). To see this, consider the limiting case with infinite damping ($\lambda \to \infty$ in (1.36) and $\alpha \to \infty$ in (1.39)). We have

$$\begin{aligned} \text{LL}: &\quad \frac{\partial \mathbf{M}}{\partial t} \to \infty \\ \text{LLG}: &\quad \frac{\partial \mathbf{M}}{\partial t} \to 0. \end{aligned} \tag{1.41}$$

Since the precessional motion is expected to drop to zero in the limit of infinite damping, one would concludes that the LLG equation (1.39) is indeed more appropriate for describing magnetization dynamics. With a suitable choice of the damping constant, the LLG equation has been shown to produce results in good agreement with experimental observations and has become a mainstay feature in micromagnetic numerical models [20, 21, 22].

1.4 Magnetization Dynamics

This section covers the theory behind two important dynamic magnetization processes at the two temporal extremes which are of particular relevance to my research: quasi-static Stoner-Wohlfarth coherent reversal, and ultrafast spin waves dynamics.

1.4.1 The Stoner-Wohlfarth Model

The Stoner-Wohlfarth model [23] is a solution to Brown's equations (1.26) in the special case of a single domain magnetic body with spheroidal geometry (shown in Fig. 1.7) and uniaxial anisotropy along its axis of rotational symmetry. In this particular case, there is no exchange contribution, and the demagnetizing field reduces to a simple tensorial relationship [24]

$$\mathbf{H}_{\text{demag}} = -\mathcal{N} \cdot \mathbf{M}, \tag{1.42}$$

where the demagnetizing tensor $\mathcal{N}$ can be expressed in terms of the demagnetizing factors N_x, N_y, N_z ($N_x + N_y + N_z = 1$) along the principal axes x, y, z of the ellipsoid

$$\mathcal{N} = \begin{pmatrix} N_x & 0 & 0 \\ 0 & N_y & 0 \\ 0 & 0 & N_z \end{pmatrix}, \tag{1.43}$$

The rotation symmetry also implies that

$$\begin{aligned} N_x &= N_y = N_\perp \\ N_z &= N_\parallel. \end{aligned} \tag{1.44}$$

Assuming the easy axis lies along the direction of the semi-major axis z, the anisotropy energy in (1.15) becomes

$$E_{an} = K_1(1 - m_z^2)V, \tag{1.45}$$

where V is the volume of the spheroid. The total free energy in (1.19) can therefore be written as

$$G(\mathbf{m}, \mathbf{H}_{\text{ext}}) = K_1(1 - m_z^2)V + \frac{1}{2}\mu_o M_s^2 \mathbf{m} \cdot \mathcal{N} \cdot \mathbf{m}V - \mu_o M_s \mathbf{m} \cdot \mathbf{H}_{\text{ext}}V. \tag{1.46}$$

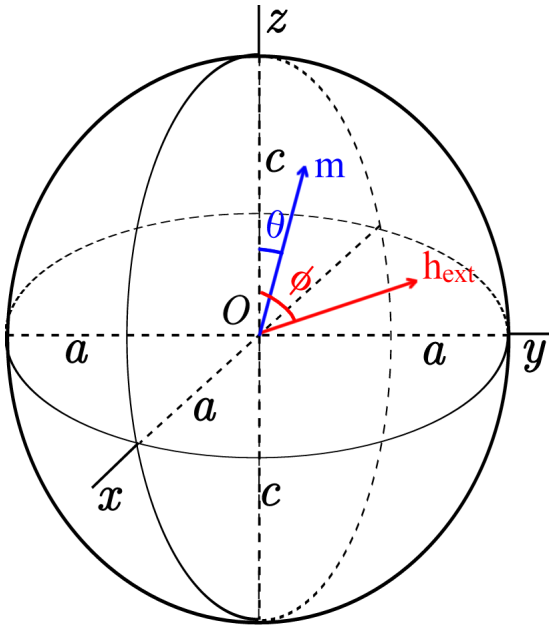

Figure 1.7: Stoner-Wohlfarth spheroid with two equal semi-minor axes along x, y and a semi-major axis in z.

which can be reduced to a more convenient dimensionless form if it is divided through by $\mu_o M_s^2 V$ and the constant terms dropped

$$g(\mathbf{m}, \mathbf{h}_{\text{ext}}) = -\frac{1}{2} k_{\text{eff}} m_z^2 - \mathbf{m} \cdot \mathbf{h}_{\text{ext}}, \tag{1.47}$$

where

$$\begin{aligned} g &= \frac{G}{\mu_o M_s^2 V} \\ \mathbf{h}_{\text{ext}} &= \frac{\mathbf{H}_{\text{ext}}}{\mu_o M_s^2 V} \\ k_{\text{eff}} &= N_\perp + \frac{2K_1}{\mu_o M_s^2} - N_\parallel. \end{aligned} \tag{1.48}$$

The rotational symmetry ensures that the magnetization lies in a plane defined by the easy axis z. It is therefore more convenient to express (1.48) in terms of the spherical polar angles θ, ϕ between $\mathbf{m}$, z and $\mathbf{h}_{\text{ext}}$. Referring to Fig. 1.7,

$$g(\theta,\phi) = -\frac{1}{2}k_{\text{eff}}\cos^2\theta - h_{\text{ext}}\cos(\phi-\theta)$$
$$= -\frac{1}{2}k_{\text{eff}}\cos^2\theta - h_{\parallel}\cos\theta - h_{\perp}\sin\theta. \quad (1.49)$$

where $h_{\parallel}, h_{\perp}$ are the components of $\mathbf{h}_{\text{ext}}$ parallel and perpendicular to the z axis.

Assuming $\mathbf{h}_{\text{ext}}$ lies along $-z$, the free energy g can be plotted against θ, the angle between $\mathbf{m}$ and the easy axis direction z, for different external field values. As shown in Fig. 1.8, for (a) zero or (b) small $\mathbf{h}_{\text{ext}}$, g possesses two minima; at the critical value of $\mathbf{h}_{\text{ext}}$ (c), one of the minimum turns to a saddle point. For fields greater than this critical value, only one energy minimum remains.

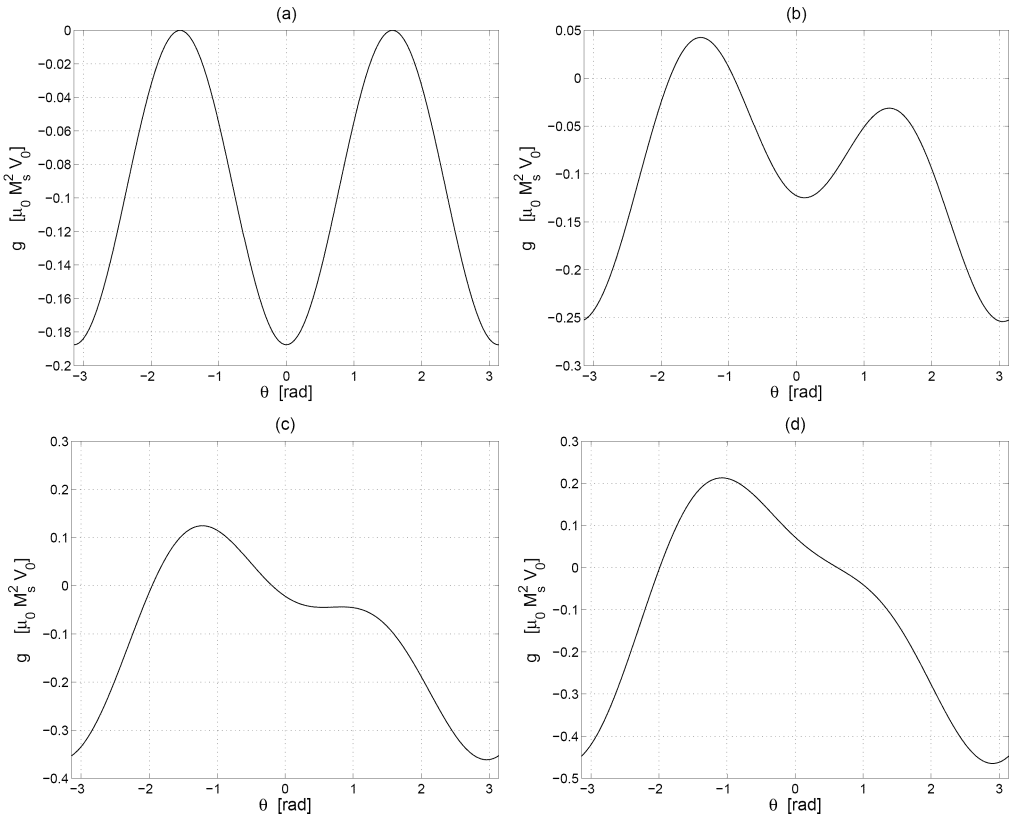

Figure 1.8: Free energy vs. θ at different $\mathbf{h}_{\text{ext}}$ along $-z$, from D'Aquino [12].

The critical $\mathbf{h}_{\text{eff}}$ can be found through the derivatives of g. The saddle point satisfies

$$\frac{\partial g}{\partial \theta} = \frac{\partial^2 g}{\partial^2 \theta} = 0, \tag{1.50}$$

which leads to the parametric solution in terms of polar angle θ

$$\begin{cases} h_{\parallel} = -k_{\text{eff}} \cos^3 \theta \\ h_{\perp} = k_{\text{eff}} \sin^3 \theta. \end{cases} \tag{1.51}$$

(1.51) can be plotted in the Cartesian plane defined by $h_{\parallel}$, $h_{\perp}$ in units of k_{eff}, as shown in Fig. 1.9. The line represents cross-over from single (outside) to double (inside) energy minima and is known as the **Stoner-Wohlfarth asteroid**. It provides a model for the observed hysteretic behavior in ferromagnets.

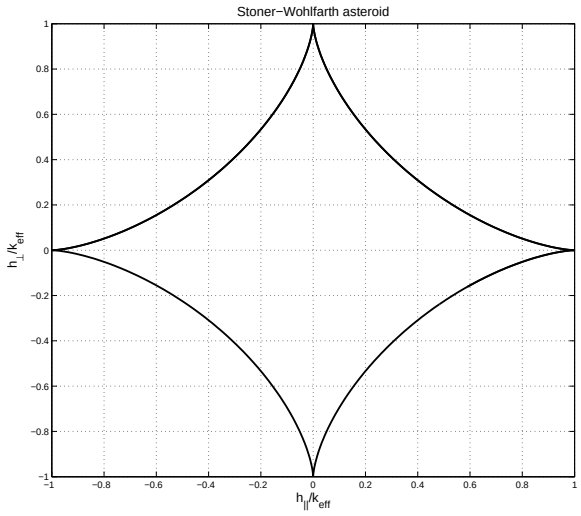

Figure 1.9: Stoner-Wohlfarth asteroid

1.4.2 Spin-Waves

Spin-waves refer to the small-angle precessional perturbations of magnetization **M** that propagate through a ferromagnetic body. They can be regarded as the magnetic equivalent of lattice vibration waves. Unlike phonons however, *magnons*, the quasi-particle carriers of spin-waves are not described by amplitude, but rather the phase variation θ of the precessing spins as a function of position, as illustrated in Fig. 1.10.

Similar to lattice vibrations, spin-wave propagation is characterized by a disper-

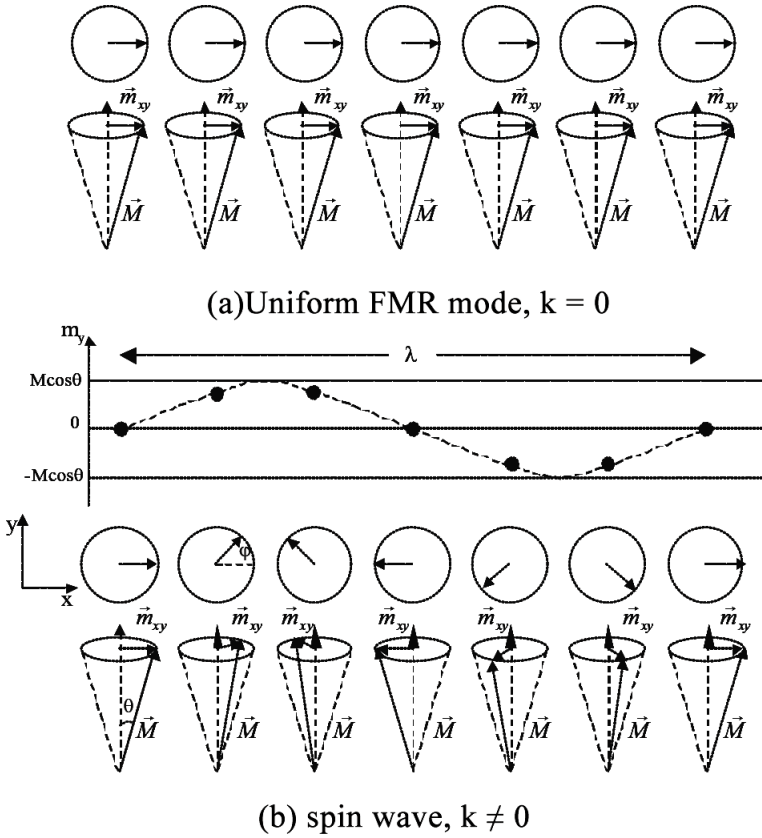

Figure 1.10: Spin-wave modes, from Elena [25].

sion relation between frequency and wave vectors. This can be analytically derived for certain simple geometries through the linearized LLG equation (1.39)[8] in the limit of zero damping, though the calculation is rather involved[9].

The simplest case is the uniform mode illustrated in Fig. 1.10(a), where the magnetic body precesses as a single macrospin, corresponding to $\mathbf{k} = 0$. The frequency of this mode is called the ferromagnetic resonance frequency f_{FMR}. For an isotropic, infinite magnetic media magnetized along the direction of an in-plane external field H_{ext}, it can be shown that f_{FMR} is given by Kittel's formula [27]

$$f_{\mathrm{FMR}} = \frac{\mu_o \gamma}{2\pi} \sqrt{H_{\mathrm{ext}}(H_{\mathrm{ext}} + M_s)}. \tag{1.52}$$

The uniform mode is governed by the dipolar interaction alone with no exchange

[8]Linearization is performed under the assumption of small angle dynamics, i.e. $M(t) = \mathbf{M}_s + \mathbf{m}(t)$ and $|\mathbf{m}| \ll |\mathbf{M}_o|$

[9]See, for example, [26, chap. 8] for a quantum mechanical treatment

contribution.

In the $\mathbf{k} \neq 0$ case illustrated in Fig. 1.10(b) displacement of neighboring spins result in an exchange contribution to the spin-wave energy. This effect can be incorporated into (1.52), in what is known as the Herring-Kittel formula [28]

$$f = \frac{\mu_o \gamma}{2\pi} \sqrt{(H_{\text{ex}} + H_{\text{ext}})(H_{\text{ex}} + H_{\text{ext}} + M_s \sin^2 \phi)}, \tag{1.53}$$

for a spin-wave vector at angle ϕ to the equilibrium magnetization position. (1.53) shows that exchange interaction increases the spin-wave frequency by contributing to the total effective field.

In ferromagnetic thin films, the situation is significantly more complex. Surface demagnetizing fields modify the dispersion relation through its contribution to the effective field. Comprehensive calculations performed by Damon and Eshbach [29] show that the dispersion relation of magnetostatic spin-wave modes in in-plane magnetized thin films are highly anisotropic and can be classified into either surface[10] or volume mode based on the propagation angle ϕ.

As illustrated in Fig. 1.11 and 1.12, the surface mode is characterized by a positive dispersion above the critical angle ϕ_c, and constant dispersion equal to f_{FMR} below ϕ_c. The volume mode is described by a negative dispersion for wave vector perpendicular to equilibrium magnetization, commonly referred to as the backward volume wave (BVW); and a constant dispersion equal to f_{FMR} for wave vector parallel to equilibrium magnetization.

1.4.3 Numerical Modeling

For a general system, the LLG equation (1.39) is typically solved numerically through energy minimization (for computing quasi-static equilibrium) and time integration (for computing dynamics) techniques implemented in a number of standard micromagnetic finite-element modeling packages [30]. The target magnetic system must be appropriately discretized both spatially (rectilinear unit cells comparable in dimension to l_{ex}) and temporally (integration time step $\geq$ highest characteristic frequency). The LLG equation is solved iteratively for each unit cell over successive time step increments. More details will be given in chapter 5.

[10] so-called because the amplitude of dynamic magnetization decays exponentially from a surface maximum through the film thickness.

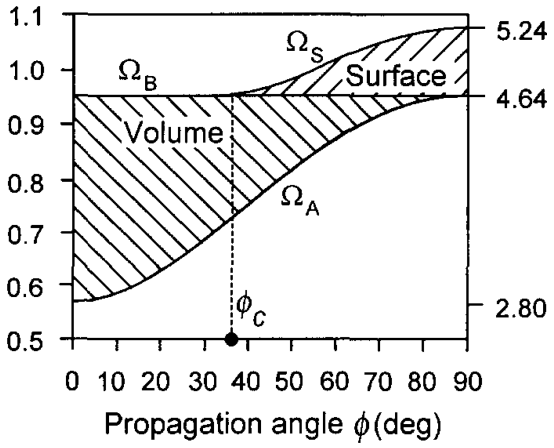

Figure 1.11: Volume and surface spin wave modes as a function of propagation angle ϕ. The bounding curves Ω_S, Ω_B and Ω_A show the upper and lower limits of the two mode bands. From Hurben and Patton [29].

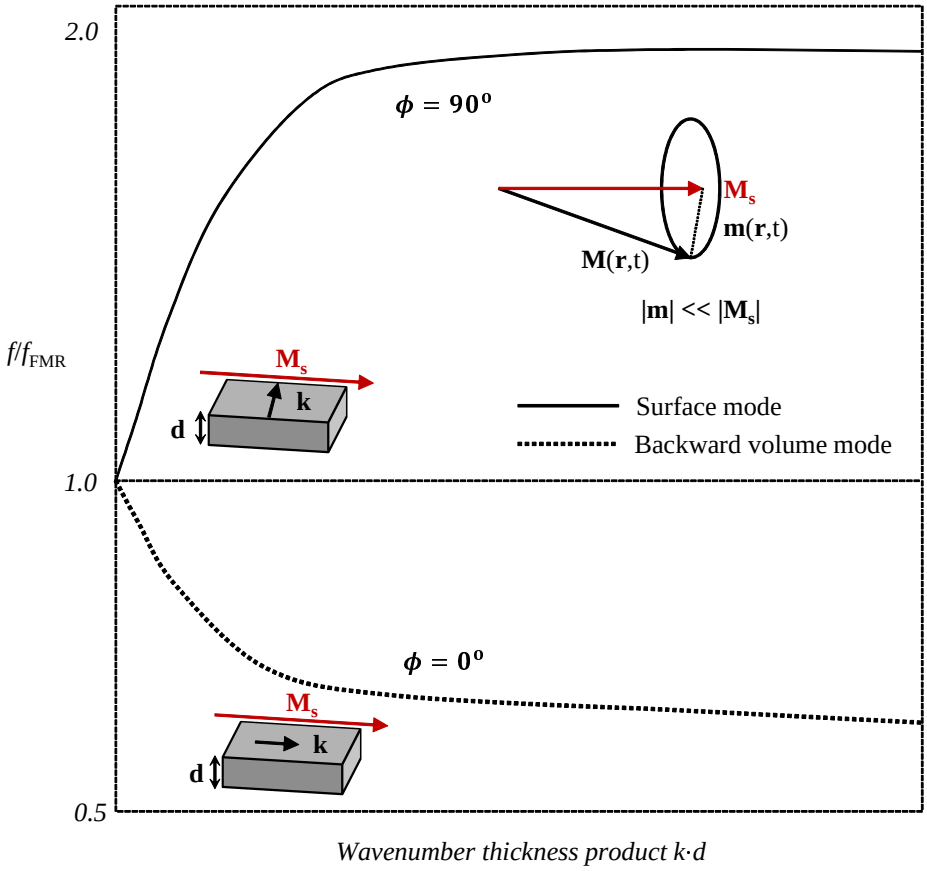

Figure 1.12: Damon Eshbach magnetostatic spin wave dispersion relation for permalloy thin film

Chapter 2

Exchange Bias

2.1 Introduction

When a ferromagnetic (FM) / antiferromagnetic (AF) bilayer is heated above a certain temperature, the exchange torque exerted by the FM spins on the neighboring AF spins at the FM/AF interface becomes strong enough to overcome the energy barrier holding the AF spins in place. As a result, the AF spins near the interface will align with the FM ordering. If the system is cooled to room temperature in this condition, the AF spins will be 'frozen' in place, and the FM ordering adopted by the AF spins is retained. This *spin imprinting* process, as it is commonly called, is illustrated in Fig. 2.1.

In the simplest case where the original FM ordering is uniform (Fig. 2.1(a)), the imprinting results in a uniform interfacial bias field acting on the FM layer by the AF spins, which can be readily included in our micromagnetic framework as an additional anisotropy term that is *unidirectional* in nature. Observationally, this bias field gives rise to a shift in the hysteresis *opposite* to itself, since the bias field has to be first overcome in order to switch the FM magnetization in this direction (Fig. 2.2). This phenomenon is known as **Exchange Bias**, and the anisotropy associated with it is called **Exchange Anisotropy**. The characteristic temperature at which exchange bias is established for a FM/AF system is called the **Blocking Temperature, $\mathbf{T_B}$**[1].

[1] T_B represents the critical temperature above which the order parameter of a FM/AF bilayer, exchange bias, drops to zero. It is the property of the bilayer system and in general much lower than the Néel temperature, T_N of the AF for a polycrystalline FM/AF system. The definition of T_B is fraught with certain ambiguity in literature, being frequently used interchangeably with T_N [31].

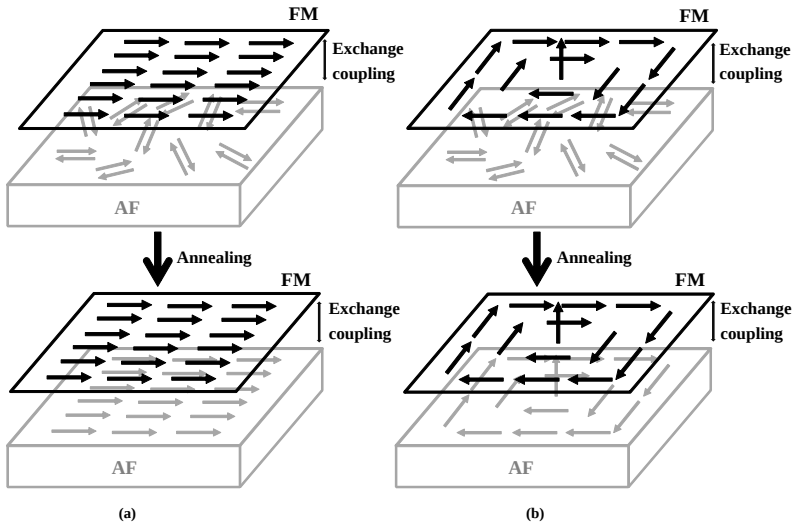

Figure 2.1: Imprinting (a) uniform FM spin ordering and (b) Non-uniform vortex FM ordering into AF.

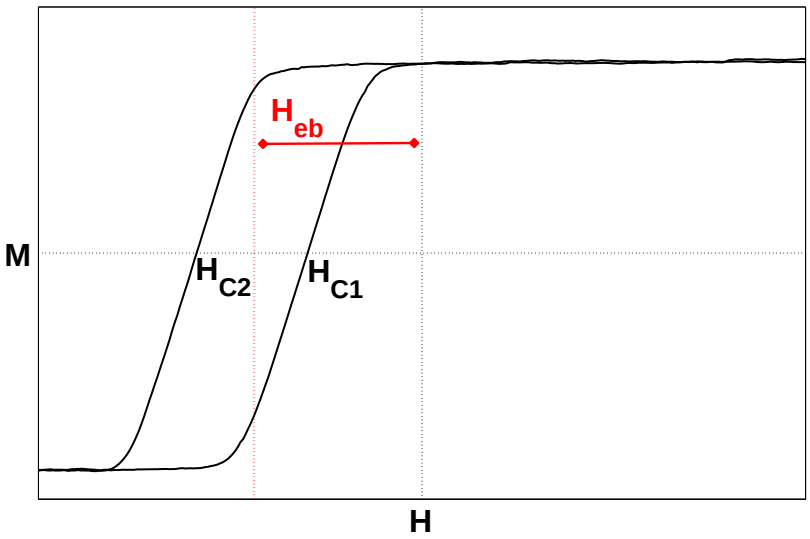

Figure 2.2: Exchange-bias.

The exchange-bias phenomenon was first discovered in 1956 by Meiklejohn and Bean [32] when studying ferromagnetic cobalt particles embedded in their native AF oxide CoO. It has since been observed in numerous systems containing FM/AF

interfaces, such as small particle core-shell systems and layered thin films[2].

The critical roles played by exchange bias in conventional and tunneling magnetoresistance spin valve[3] devices [34, 35] as well as MRAMs [1, 36] have triggered unprecedented increase of research in FM/AF thin film systems, and in particular, lithographically patterned nanostructures [13]. Recent studies have shown that the FM ordering imprinted into the AF does not have to be uniform. For example, a remanent FM vortex magnetization can be faithfully copied into the AF layer when the system is cooled through T_B, creating an inhomogeneous interfacial exchange-bias field that follows the FM vortex magnetization [37, 38], i.e., Fig. 2.1(b). The interplay between this non-uniform exchange-bias field and magnetostatic energies of the vortex magnetization significantly modifies the magnetic behavior of the system, giving rise to a wide variety of complex behaviors which can be observed experimentally [39, 40].

2.2 Phenomenology

As previously mentioned, in the case where the FM ordering is uniform, say, induced by a saturating, uniform cooling field when the bilayer is heated past T_B, exchange bias would manifest most prominently as a shift in the hysteresis loop in the opposite direction to the cooling field. The exchange-bias field, $H_{\rm eb}$, can be trivially calculated from this loop shift. Referring to Fig. 2.2:

$$H_{\rm eb} = \frac{H_{C1} + H_{C2}}{2}, \tag{2.1}$$

where H_{C1} and H_{C2} are the coercive fields for increasing and decreasing sweeping fields respectively. The coercivity is given by

$$H_C = \frac{H_{C1} - H_{C2}}{2}. \tag{2.2}$$

A quantity related to $H_{\rm eb}$ is the interfacial exchange energy $J_{\rm eb}$, which is a measure of the strength of exchange bias. It assumes the phenomenological form

[2]Refer to the comprehensive review papers by Nogués et al. [13], Nogués and Schuller [33] for extensive lists of references.

[3]Spin valve sensors consist of a reference layer with fixed magnetization, a free layer whose magnetization direction aligns with an external field, and a nonmagnetic spacer layer separating the two. The magnetization of the reference layer can be fixed through exchange coupling with an adjacent antiferromagnetic layer.

$$J_{\rm eb} = H_{\rm eb} M_s t_{\rm F}, \tag{2.3}$$

where $t_{\rm F}$ and M_s are the thickness and saturation magnetization of the FM layer.

Other commonly observed effects of exchange bias include coercivity enhancement (Fig. 2.3(b)) as a result of greater hysteretic energy losses due to exchange coupling[4] and asymmetric reversal. These will be further discussed in the later chapters.

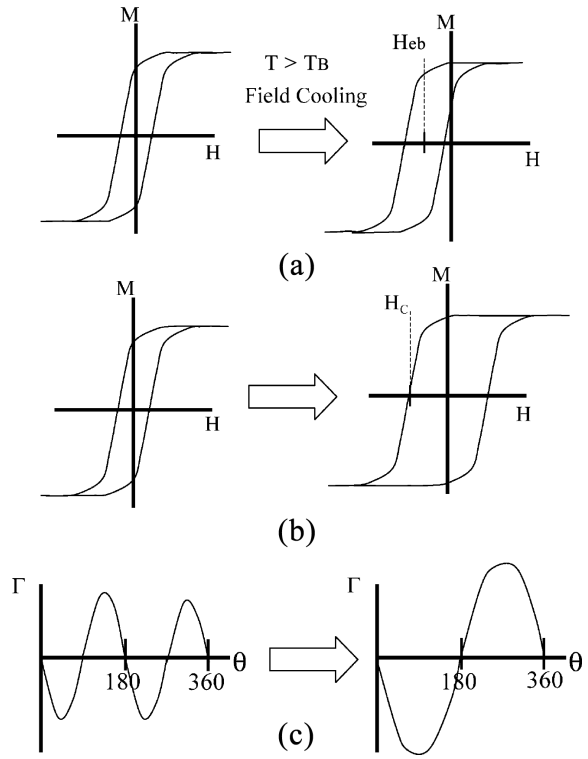

Figure 2.3: Observable effects of exchange bias. (a) Hysteresis loop shift (b) Coercivity enhancement and (c) Torque magnetometry, from Nogués et al. [13].

The unidirectional nature of exchange bias is demonstrated via torque magnetometry [32] (Fig. 2.3(c)), with a $K\cos\theta$ dependence of the magnetic torque (as opposed to the $K\sin^2\theta$ dependence observed for uniaxial anisotropy) corresponding to a single minimum energy state. The interfacial nature of exchange bias is convincingly demonstrated by the inverse dependence of $H_{\rm eb}$ on $t_{\rm F}$ observed in numerous experi-

[4]This effect is typically observed in the case of weak exchange bias, where instead fully aligning with FM, the AF spins retain partial anti-ferromagnetic ordering, which, when coupled to the FM layer, increases its effective inhomogeneity. Such systems are marked by small a hysteresis loop shift and a large increase in coercivity.

ments [33].

The original model proposed by Meiklejohn and Bean [32] can provide an intuitive understanding of the origin of the hysteresis loop shift. The model considers the simplest possible case, in which the AF is fully aligned with a uniformly positive FM ordering, and the magnetization in each layer rotates coherently (i.e., as a macrospin).

Fig. 2.4 shows schematics of the spin configuration for this system during different stages of hysteresis. If the AF anisotropy is strong enough, the interfacial spins in the AF will remain fixed during FM reversal, and exert microscopic torques via exchange coupling on the FM spins as they start to rotate, in an attempt to keep them in alignment. The external field must overcome this additional torque when switching the FM magnetization towards the negative direction (Fig. 2.4(b)), the coercive field H_{C2} in the decreasing field branch is thus increased. Conversely, when a positive external field switches the FM magnetization back, the torque exerted by the AF layer now works with the external field (Fig. 2.4(d)), reducing the coercive field H_{C1} in the increasing field branch . The overall effect is the net shift of the hysteresis loop along the negative field direction.

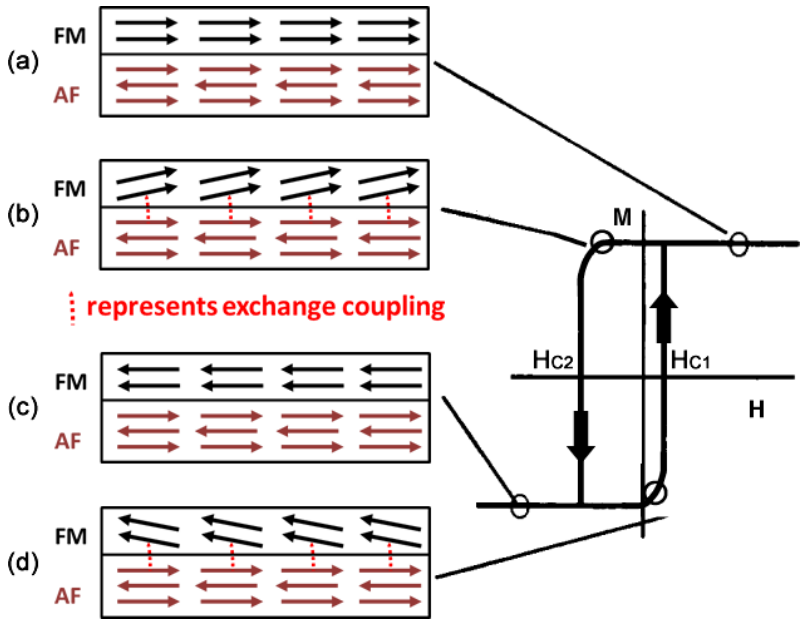

Figure 2.4: Intuitive picture of exchange bias, from Nogués et al. [13].

From the intuitive picture, we see that the AF spins at the interface should be *uncompensated* and remain *pinned* while the FM spins rotate with the external field in order to observe the loop shift.

2.2.1 Compensated vs. uncompensated

In a compensated AF interface, the net spin averaged over a macroscopic length scale is zero, with no net magnetization. In contrast, the interface is said to be uncompensated if the spin arrangement is such that the net magnetization is non-zero. This difference is illustrated in Fig. 2.5.

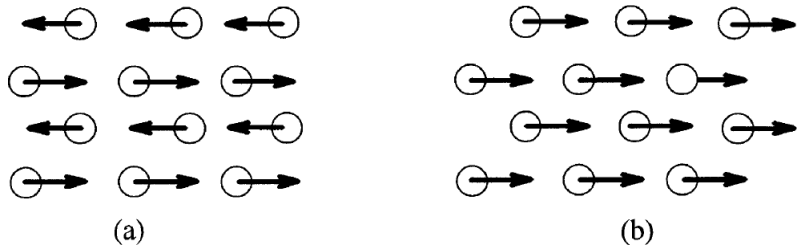

Figure 2.5: Compensated (a) vs. uncompensated (b) AF interface, from Nogués and Schuller [33].

2.2.2 Critical AF Thickness

From an energy point of view, pinning of the AF layer during FM reversal requires the (bulk) AF anisotropy energy density to be greater than the interfacial coupling energy J_{eb},

$$K_{\mathrm{AF}} t_{\mathrm{AF}} \geq J_{\mathrm{eb}}, \tag{2.4}$$

where K_{AF} is anisotropy constant. This sets a lower bound on the AF thickness t_{AF}, below which the exchange coupling causes the AF spins to rotate with FM, and no exchange bias is observed.

Many theories of exchange bias rely on the existence of pinned, uncompensated AF spins near the interface [41, 42]. The actual depth profile of the uncompensated spins near the FM/AF interface can be experimentally investigated using magnetization-sensitive techniques such as X-ray magnetic circular dichroism (XMCD), in which the left and right circularly polarized X-rays exhibit differential absorption spectra depending on sample magnetization. Studies [43] have shown that the AF spins near the FM/AF interface are indeed uncompensated. However, within the immediate vicinity of the interface ($\leq 3\,\mathrm{nm}$, which can be considered the critical AF thickness), the uncompensated AF spins are overcome by exchange and rotate with the FM spins

in response to an external field, while the uncompensated AF spins at thicknesses beyond this region remain pinned, providing the actual exchange bias.

2.3 Aspects of Exchange-Bias Theory

Despite general acceptance that exchange bias originates from the interfacial FM/AF exchange coupling, the microscopic details of this coupling are poorly understood, and how it translates into the various observed effects of exchange bias remains an area of active research, with numerous proposed models[41, 42, 44, 45] attempting to explain the complex nature of the FM/AF interface.

As previously mentioned, the strength of exchange bias in a FM/AF system can be measured using the phenomenological interfacial exchange energy, J_{eb}. From (2.3)

$$J_{\mathrm{eb}} = H_{\mathrm{eb}} M_s t_{\mathrm{F}} = K_{\mathrm{eb}} t_{\mathrm{F}}, \tag{2.5}$$

where $K_{eb} = H_{\mathrm{eb}} M_s$ is the exchange anisotropy constant.

Merely constructing a theoretical model that is capable of predicting experimental J_{eb} values within order-of-magnitude accuracy has proven a considerable challenge. Consider a FM domain wall in a FM/AF bilayer driven by an applied in-plane field H along the exchange-bias axis, Fig. 2.6. The exchange-bias field can be determined by the balance between the applied field pressure (energy per unit area), $2HM_s t_{\mathrm{F}}$, and the pressure $\Delta\sigma = \sigma_2 - \sigma_1$ from the interfacial energy difference between the two domain orientations, when the domain wall is held stationary by these two pressures.

$$H_{\mathrm{eb}} = \frac{\Delta\sigma}{2M_s t_{\mathrm{F}}}. \tag{2.6}$$

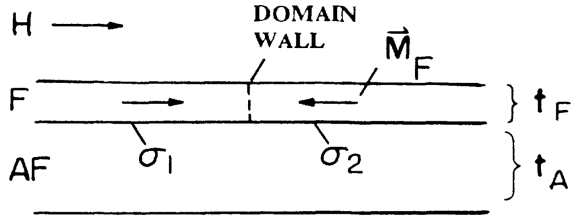

Figure 2.6: Balance between external field and exchange-bias field, from Malozemoff [44].

Some basic assumptions must be made at this point. In order to establish exchange

bias, the bulk AF spins need to be *fixed* and *in-plane*, otherwise the two FM domain orientations would correspond to identical energy configurations, and no exchange bias would be observed[5].

Recall the Heisenberg Hamiltonian, (1.3), the energy between a pair of atomic spins $\mathbf{S}_i$ and $\mathbf{S}_j$[6] across the interface with ferromagnetic nearest neighbor exchange integral J_{F} is given by:

$$E_{ij} = -J_{\mathrm{F}}\mathbf{S}_i \cdot \mathbf{S}_j. \tag{2.7}$$

With a fully compensated interface, shown in Fig. 2.7(a), the total energy as well as exchange-bias field are zero. For fully uncompensated interfaces in Fig. 2.7(b) and Fig. 2.7(c) corresponding to the simple intuitive model of the previous section, $\Delta\sigma$ between the two ferromagnetic orientations can be shown to be $\sim 2J_{\mathrm{F}}S^2/a^2 \simeq 2J_{\mathrm{F}}/a^2$ for a cubic lattice with lattice parameter a. According to (2.6) therefore,

$$H_{\mathrm{eb}} = \frac{J_{\mathrm{F}}}{a^2 M_s t_{\mathrm{F}}} \tag{2.8}$$

Note that this is identical to (2.3) with $J_{\mathrm{F}}/a^2 = J_{\mathrm{eb}}$, as J_{F} is defined as energy *per pair* of atomic spins (i.e. over an area of a^2), while J_{eb} is defined as energy *per unit area*.

Reasonable values for J_{F}, M_s and t_{F} give estimates of H_{eb} based on (2.8) that are two orders of magnitude too large. One might construe that some innominate interfacial disorder is frustrating 99% of the exchange coupling, however, the consistency of experimental measurements beckons a more intrinsic mechanism and improvements to the simple model to quantitatively match experimental results.

A common way to improve upon an existing model is to add dimensional variability. Consider, for example, the formation of a planar domain wall in the AF layer near the interface (1D variability), for the unfavorable FM orientation, as illustrated in Fig. 2.7(d). This relaxes the configuration in Fig. 2.7(c) by spreading the interfacial exchange energy over the domain wall. Assuming in-plane uniaxial anisotropy energy density K_{AF}, nearest neighbor exchange integral J_{AF} and exchange stiffness $A_{\mathrm{AF}} \sim J_{\mathrm{AF}}/a$ for the AF layer, one can show that the AF domain wall has an energy

[5] If the bulk AF spins are free to rotate with the FM spins, they would align with the FM, and $\Delta\sigma = 0$. Similarly, if the AF spins point perpendicularly out-of-plane, the two opposite in-plane FM domains have identical energy in relation to the AF orientation, and we again have $\Delta\sigma = 0$.

[6] A typical magnetic transition metal possess two unpaired electrons in its valence 3d shell, therefore as an simple approximation, the total atomic spin at each lattice site $S_i = 1$.

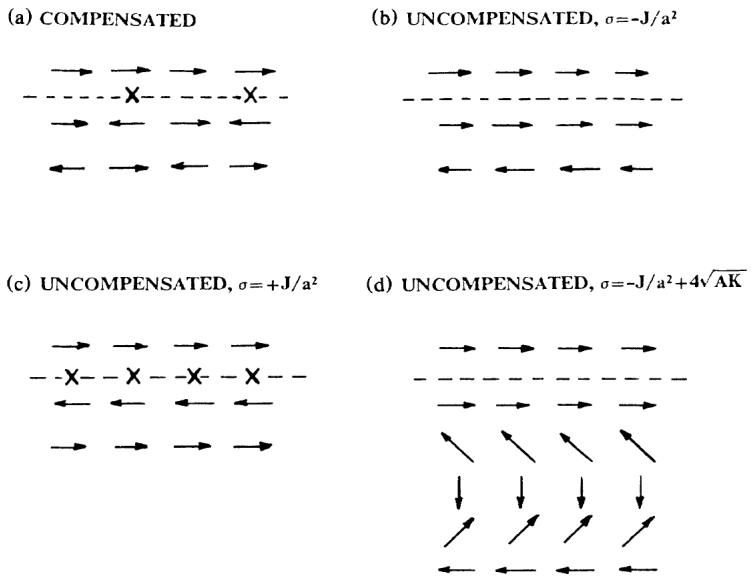

Figure 2.7: Schematics of possible spin arrangements in FM/AFM sandwich. Dashed lines indicate boundary, crosses indicate frustration of FM coupling.

density of $4\sqrt{A_{\rm AF}K_{\rm AF}}$ per unit area [46], which also represents the difference in energy density between the two FM orientations, $\Delta\sigma$. (2.6) thus becomes

$$H_{\rm eb} = \frac{2\sqrt{A_{\rm AF}K_{\rm AF}}}{M_s t_{\rm F}}. \tag{2.9}$$

Assuming identical nearest neighbor exchange parameters, $J_{\rm F} = J_A = J$, and take $A_{\rm AF} \simeq J/a$, we see that the energy expression in (2.9) is reduced from (2.8) by a factor of $\sqrt{A_{\rm AF}/K_{\rm AF}}/2a$, or the ratio between domain-wall width parameter (see (1.29), typically 10s of nm) divided by twice the lattice parameter (a few Å), which is indeed in the 10^2 range. However, this model fails to address the persistence of exchange bias down to the critical AF thickness, typically several nm, which is order of magnitude below the characteristic domain wall width in most AF materials.

We therefore add additional variability to our model, by assuming that random interface disorder exists as a random interface field. The AF spins reorient themselves in order to minimize local random field energy, forming random AF domains along the interface which are separated by domain walls perpendicular to the interface, as shown in Fig. 2.8.

This interfacial randomness can be represented by a factor f_i, such that the effective nearest neighbor exchange integral is $J_i = f_i J$. According to random statistics,

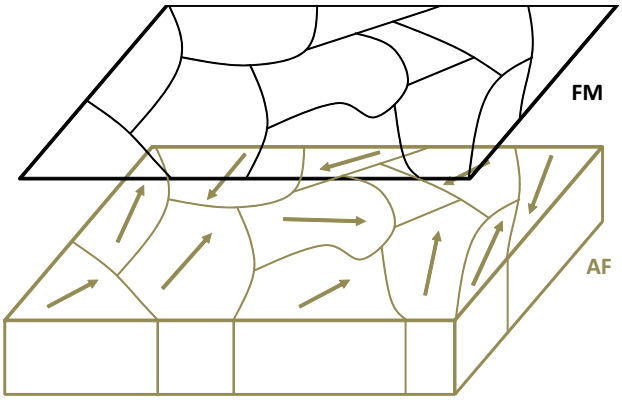

Figure 2.8: Random field model with perpendicular AF domain walls.

for an interface domain area of L^2 with $N = L^2/a^2$ atoms, the random-field energy density is given by:

$$\Delta\sigma \simeq -f_i \frac{J}{a^2\sqrt{N}} \simeq -f_i \frac{J}{aL}, \tag{2.10}$$

which means the larger the characteristic domain size L, the smaller the averaged interfacial energy. The exchange-bias field is calculated as

$$H_{\mathrm{eb}} \simeq \frac{f_i J}{2M_s t_{\mathrm{F}} aL}. \tag{2.11}$$

As we shall see, the size of the interfacial AF domain L and degree of randomness f_i depend on a variety of correlated factors such as growth conditions and crystal structure, all of which impact the experimentally observed exchange bias [47].

Chapter 3

Experimental Methodology

3.1 Sample Preparation

The ability to fabricate magnetic nanostructures with precise control over geometry, texture and composition is crucial for my research. In this section I will describe the techniques used for sample preparation, which includes patterning, deposition and post-deposition annealing.

3.1.1 Electron Beam Lithography

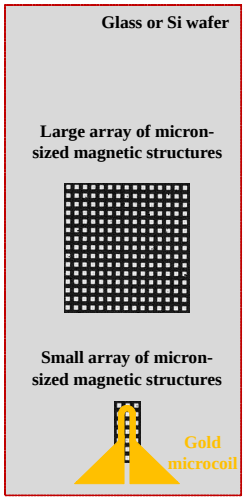

Figure 3.1: Sample schematic.

A schematic of the experimental sample is shown in Fig. 3.1. The micron-sized

magnetic structures and gold microcoil were patterned on silicon and glass substrates using the RAITH50 electron beam lithography (EBL) system in the UVic Nanofabrication facility. The system doubles as a scanning electron microscope (SEM) for high-resolution sample imaging.

Lithography refers to the collective process whereby a geometric pattern is transferred onto a substrate [48]. As the first part of the fabrication process, lithography generally consists of resist coating, pattern exposure, development, deposition and lift-off, as shown in Fig. 3.2(a)-(b).

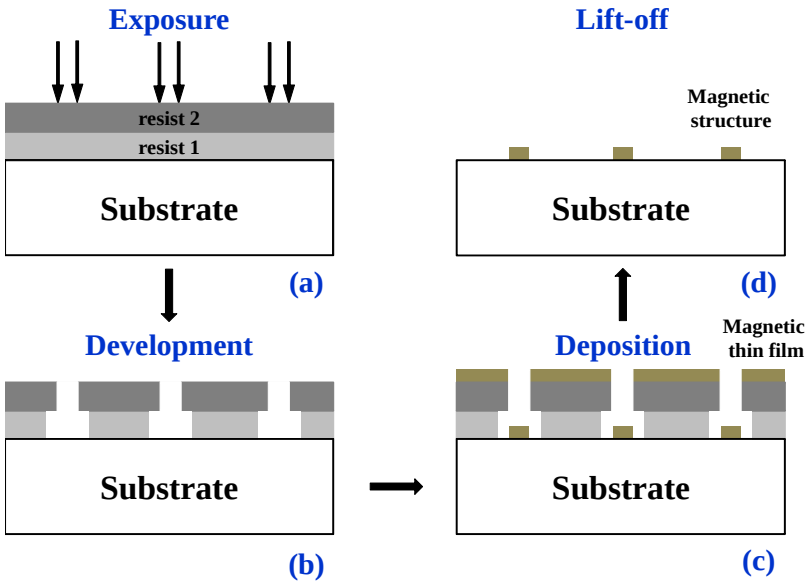

Figure 3.2: General fabrication process.

Substrates were spin-coated with two uniform layers of poly-methyl-methacrylate (PMMA) resist with different molecular weights. The resist thicknesses depend on the thickness of the structures to be fabricated and was set by the speed of the spin-coater. Selected areas of the coated substrates were then exposed to a high-energy electron beam, whereupon de-crosslinking of the exposed polymer chains allow for the selective removal of the exposed resist by a chemical developer. The desired magnetic materials were subsequently deposited on the patterned substrates (Fig. 3.2(c)), and the substrates were lifted off in acetone which dissolves the remaining resist, leaving behind the patterned magnetic structure. The heavier molecular weight of resist 2 gives an undercut depth profile for easier break-off of the residual resist during lift-off (Fig. 3.2(d)). Patterning parameters are listed in Tab. B.1, Appendix B.

3.1.2 Physical Vapour Deposition

Physical vapour deposition (PVD) refers to the controlled physical transference of a material from a source to a substrate. The two PVD techniques employed in my research were thermal evaporation and sputtering.

Electron Beam Evaporation

The gold microcoils were deposited using an Ångstrom Åmod electron beam evaporation system, courtesy of Professor David Steuerman's research group in the Department of Chemistry.

In an electron beam evaporator, the source (target) material contained in a crucible is heated into a liquid melt by a magnetically-focused thermionic electron beam. The melt evaporates under vacuum, and upon precipitation creates a thin layer of the source atoms on all line-of-sight surfaces. The deposition rate was monitored by a quartz crystal microbalance (QCM) sensor, whose resonant frequency is sensitive to the deposition thickness [49]. Evaporation parameters are provided in Tab. B.2, Appendix B.

Magnetron Sputtering

The magnetic layers were deposited using DC-triode magnetron sputtering, curtesy of our collaborator, Professor Thanasis Speliotis at the Institute of Materials Science (IMS) in Athens, Greece.

In a sputter deposition system, magnetron-enhanced bombardment of the target surface by a inert gas 'sputters' atoms from the target slab with $\sim 5\,\mathrm{eV}$ kinetic energy. A fraction of the sputtered atoms subsequently condenses on the substrate surface. Compared to thermal evaporation, sputtering takes place at room temperature with much higher adatom energies, leading to higher degree of compositional and textural consistency, better adhesion and more defined magnetic properties [50], and is therefore the preferred PVD technique for the magnetic structures. Sputter deposition parameters are provided in Tab. B.3, Appendix B.

3.1.3 Post-Deposition Annealing

To induce exchange bias, samples were individually annealed in an induction furnace under vacuum ($5 \times 10^{-5}\,\mathrm{Torr}$) in the presence of a uniform magnetic field parallel

to an edge of the sample. The temperature of the furnace was monitored using a thermocouple and the heating/cooling rates were kept at a constant 5 °C/min using proportional-integral-derivative control.

3.2 Sample Characterization

3.2.1 The Magneto-Optical Probe

Quasi-static and dynamic measurements of magnetization were realized using the magneto-optical Kerr effect (MOKE). Discovered in 1877 [51], MOKE refers to the rotation of a linearly polarized electric field $\vec{E}$ upon reflection from a magnetic surface. For many materials, the Kerr rotation is linear, $\theta_k \propto M$, and defined by both the rotation θ_k and the ellipticity ϕ_k of the reflected field, as illustrated in Fig. 3.3.

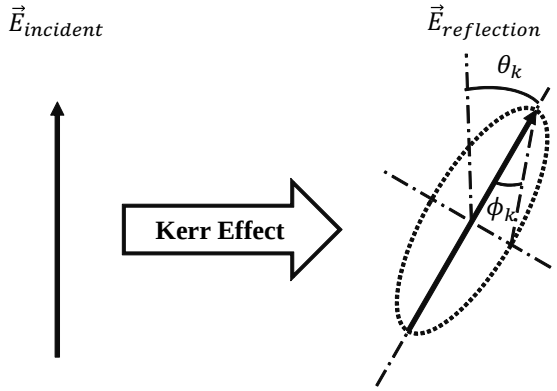

Figure 3.3: Schematic of Kerr rotation.

$$\tilde{\theta_k} = \theta_k + i\phi_k. \tag{3.1}$$

The Kerr effect lends itself naturally to the study of surface magnetization profiles in metallic ferromagnets with an information depth of $\sim 10\,\text{nm}$ [52].

An *ab initio* derivation of the magneto-optical Kerr effect is mathematically involved and can be found in a number of texts [53]. Here I only offer a simple rationale. Consider the dielectric law

$$\vec{D} = \tilde{\varepsilon}\vec{E}, \tag{3.2}$$

the complex dielectric tensor $\tilde{\varepsilon}$, containing components of the magnetization vector $\mathbf{M}$, relates $\vec{E}$ of the incident plane-polarized light to the induced displacement vector $\vec{D}$. (3.2) can be written in the form of a Lorentz force equation

$$\vec{D} = \varepsilon(\vec{E} + i\tilde{Q}\mathbf{M} \times \vec{E}), \tag{3.3}$$

where ε is the ordinary dielectric constant and $\tilde{Q}$ is the complex Voigt constant, a material parameter that depends on saturation magnetization and spin-orbit coupling. $\vec{D}$ can be construed as a secondary wave resulting from the magneto-optical interaction between $\vec{E}$ and magnetization $\mathbf{M}$.

The cross product in (3.3) reveals the gyro-electric nature of the Kerr effect. The term represents a Lorentz force acting on surface valence electrons undergoing harmonic motion as a result of the incident light. The cross product means that the corresponding Lorentz motion is perpendicular to the direction of propagation of the reflected light, and the interference results in a small rotation of the reflected polarization.

First used successfully to observe magnetic domains over 60 years ago [54], MOKE remains to this day one of the most versatile and important techniques for the imaging of magnetic microstructures.

3.2.2 Quasi-Static MOKE Setup

There exists three MOKE geometries: *polar*, *longitudinal* and *transversal*, determined by the relative orientations of the plane of incidence and the sample magnetization, as illustrated in Fig. 3.4.

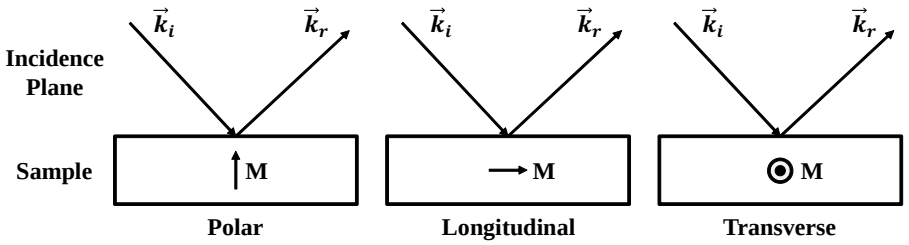

Figure 3.4: MOKE geometries.

For quasi-static hysteresis measurements, the longitudinal setup was used, with in-plane magnetization and applied field parallel to the plane of incidence. A simplified

schematic of the experimental setup is shown in Fig. 3.5

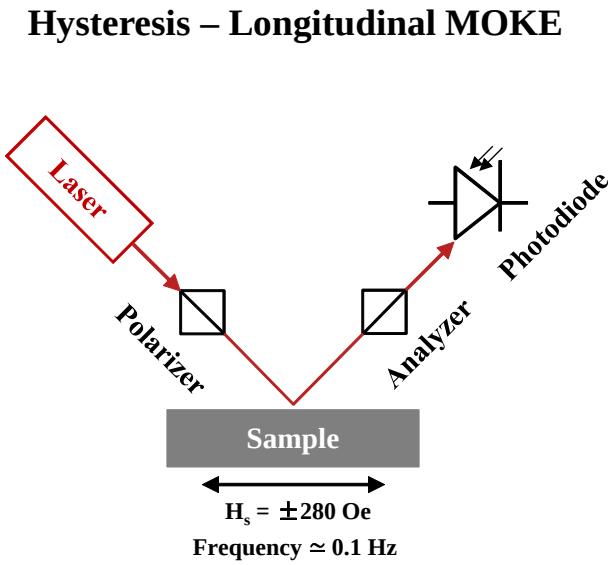

Figure 3.5: Quasi-static MOKE setup (simplified).

The laser reflects off the sample surface through a polarizer-analyzer pair and impinges on a photodiode. The polarizing axes of the polarizer-analyzer pair are orthogonally oriented, leading (ideally) to total extinction in the absence of sample magnetization (Fig. 3.6 top). If the sample is magnetized, the small Kerr rotation results in a signal proportional to the local magnetization in the sample (Fig. 3.6 bottom) at the photodiode.

The detailed MOKE implementation is shown in Fig. 3.7, equipment details are provided in Tab. B.4, Appendix B.

The linearly polarized laser is focused on the sample surface through the 10× objective at close to 45° incidence. The diverging reflected beam is re-focused through lens B, then through the analyzer before entering the silicon photodiode, which converts the light intensity to a voltage signal with a linear dependence on the magnetization. The optical chopper placed in the beam path provides a modulation reference for the incident light, enabling the phase sensitive detection of the lock-in amplifier to extract the Kerr signal from the modulation carrier through time-integration and low-pass filtering. This process significantly improves the signal to noise ratio. The pre-amplifiers provides preliminary amplification and filtering centered around the modulation frequency.

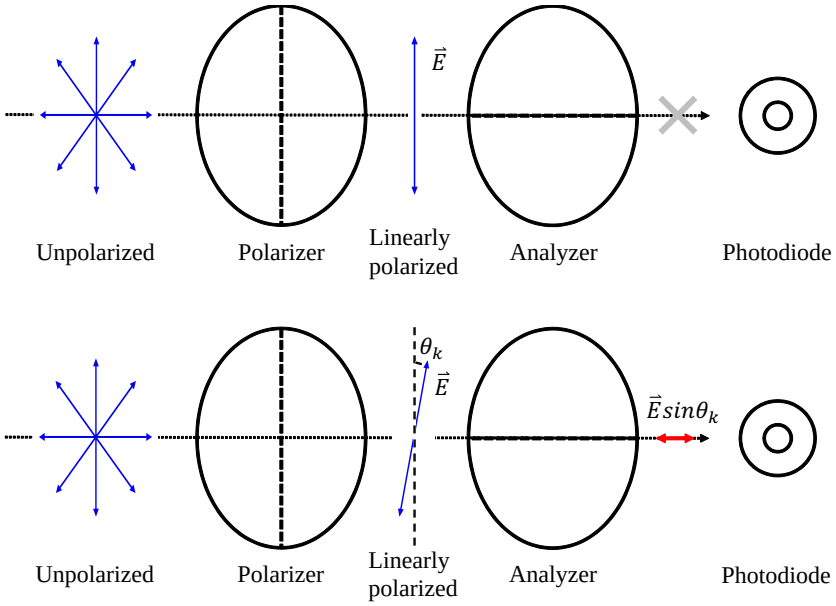

Figure 3.6: Polarizer-analyzer setup.

The sample is mounted on a micrometer positioning stage, allowing for precise alignment of the microstructures with the incident laser spot. Due to working distance constraints, the laser spot size is around $30 - 50\,\mu$m and cover several sample structures[1].

The sweeping magnetic field is provided by a ferrite-core electromagnet, with the sample located between its poles such that the field is parallel to its surface, as illustrated in Fig. 3.8. A Hall effect sensor mounted between the pole faces above the sample monitors the external magnetic field.

The photodiode and Hall probe outputs are averaged over 20 field cycles and combined to produce $M-H$ hysteresis plots. PC interfacing is achieved through National Instrument's PCI/BNC data acquisition module and LabView virtual instrumentation.

[1]Hysteresis signals are therefore averaged over several sample squares.

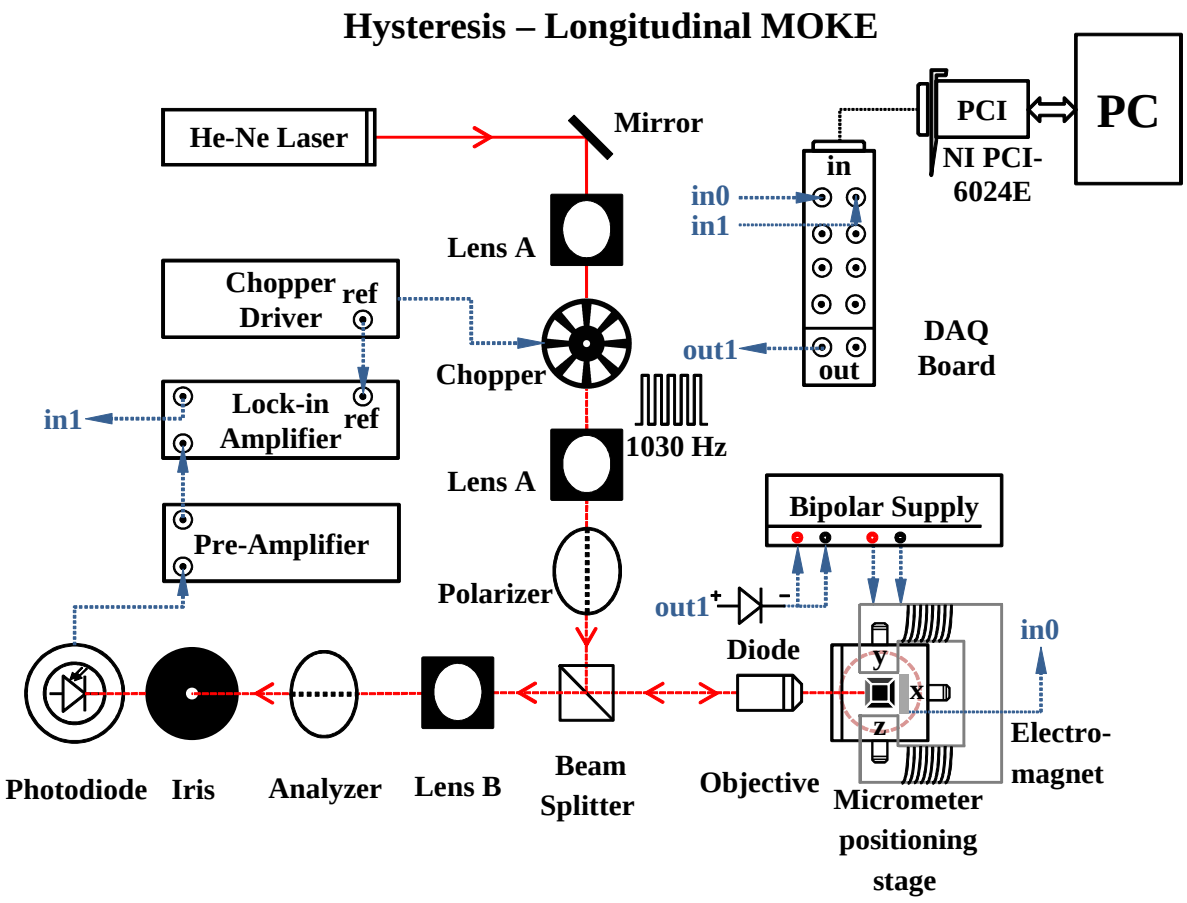

Figure 3.7: Quasi-static MOKE setup (detailed).

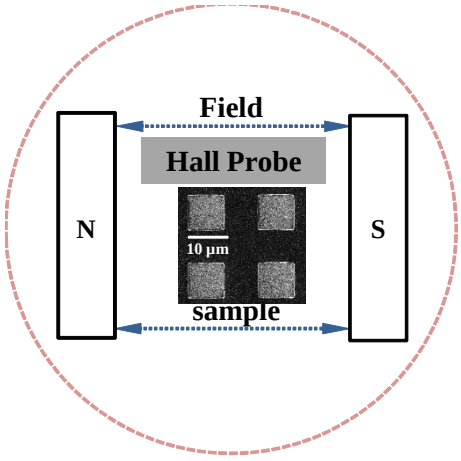

Figure 3.8: Sample arrangement between magnet pole faces.

3.2.3 The Stroboscopic Pump-Probe Technique

Probing transient magnetic behavior induced by rapidly-changing external parameters requires time-resolved techniques with resolution in the GHz precessional regime. Fortunately, the quasi-static MOKE technique can be extended to the time-resolved regime using a femtosecond ultrafast laser and employing the stroboscopic pump-probe technique [55]. The technique is identical in concept to strobe lighting in high-speed photography in that it reconstructs a fast-moving process through 'snapshots' frozen in time.

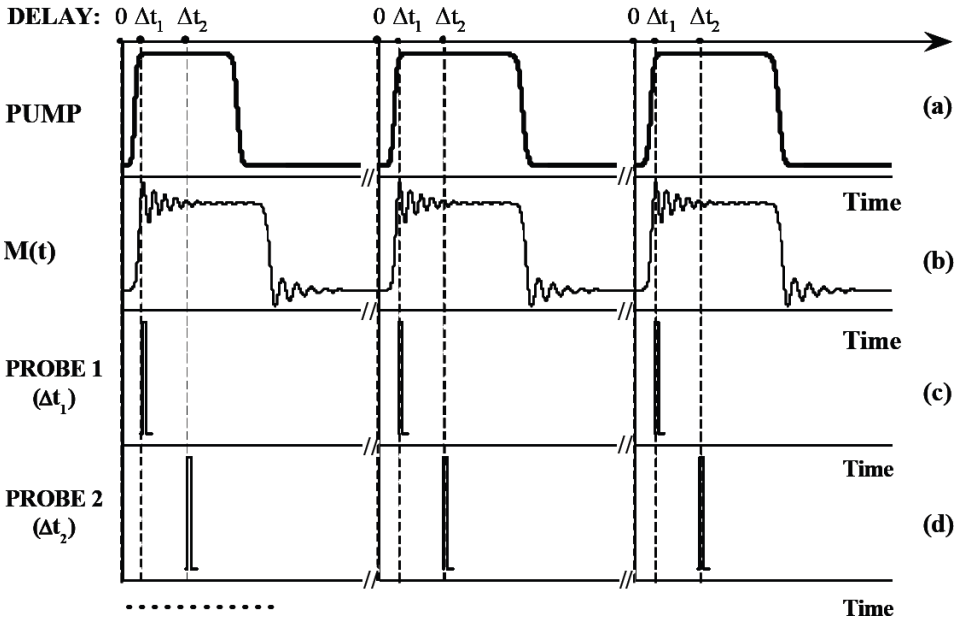

Figure 3.9: Stroboscopic pump-probe technique, from Elena [25].

First implemented in the study of sub-nanosecond magnetization dynamics by—Freeman et al. [56], the stroboscopic pump-probe technique is schematically illustrated in Fig. 3.9. The pump signal, in the form of a periodic magnetic field pulse (Fig. 3.9(a)) excites a dynamic magnetization response $\mathbf{M}(t)$ (Fig. 3.9(b)). An ultra-short laser probe pulse with the same repetition rate (Fig. 3.9(c)-(d)) but delayed with respect to the pump signal at Δt_1, $\Delta t_2 \ldots$ measures $\mathbf{M}(\Delta t_1)$, $\mathbf{M}(\Delta t_2) \ldots$ in the dynamic response with temporal resolution determined by the laser pulse signal duration, the interval between successive Δt_i and the pump-probe synchronization[2].

[2]This refers to the accuracy with which the time delay can be controlled, and can be defined as the temporal uncertainty in triggering the probe signal at the delay time t_1, $t_1 \pm \delta t$

3.2.4 Time-Resolved Kerr Effect Microscopy

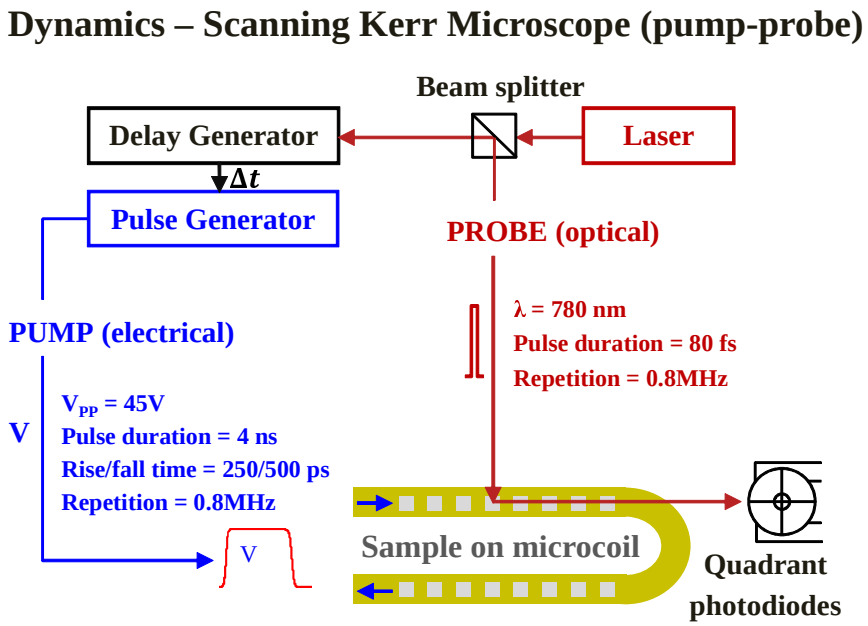

Figure 3.10: Dynamic MOKE Setup (simplified).

Fig. 3.10 shows a simplified schematic of the dynamic MOKE setup. A pulse laser beam is split into pump and probe branches through a 50/50 beam-splitting prism. The pump beam triggers electrical pulses that are electronically delayed via computer control. The delayed pulses subsequently trigger a voltage generator which excites the sample with a magnetic field pulse created by the current-carrying microcoil. The probe beam reflects off the sample through the same polarizer-analyzer setup in Fig. 3.5, and the magnetic signal is detected as a Kerr rotation using the quadrant photodiodes. Sample electrical connection is discussed in more detail below.

Sample Stage and Microcoil

Fig. 3.11 shows a rendering of the dynamic MOKE sample stage. The magnetic structures are located on gold microcoils, with a closeup shown in Fig. 3.12.

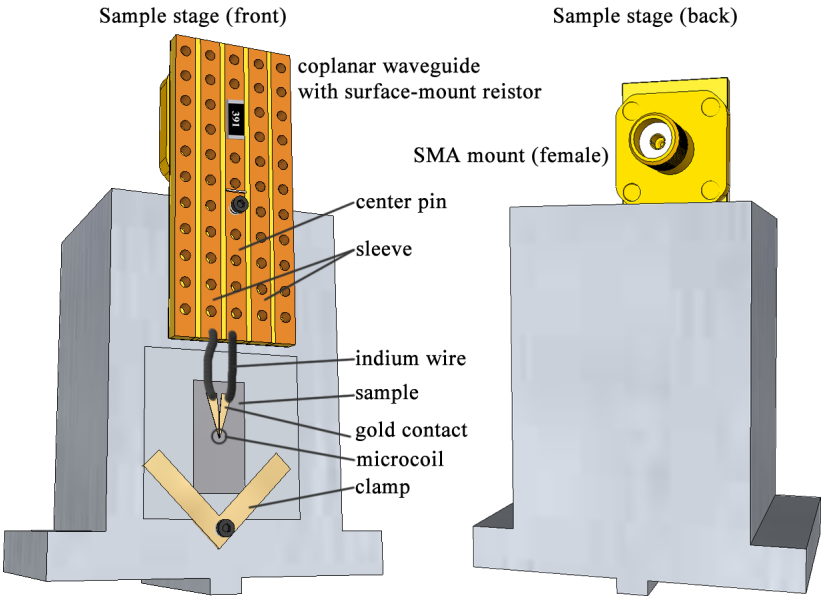

Figure 3.11: Sample stage schematic.

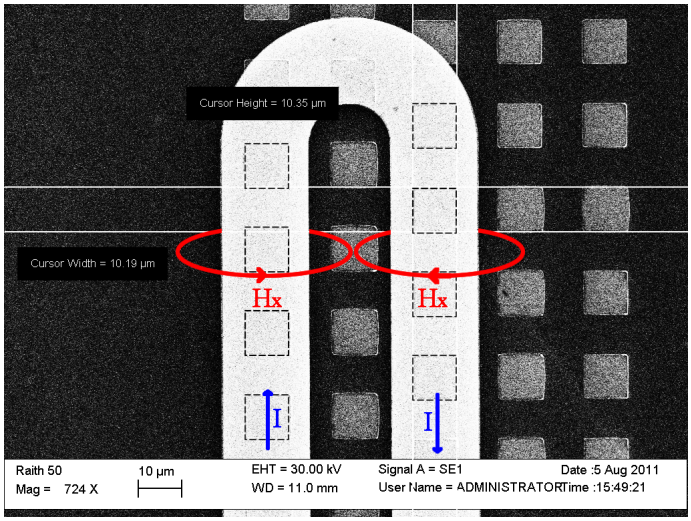

Figure 3.12: Closeup of microcoil.

The stage connects directly to a voltage pulse generator which provides the pump excitation through the coaxial SMA mount. The surface-mount resistor nominally provides $50\,\Omega$ impedance matching to maximize transmission. Given the microcoil resistance, dimension and the profile of the voltage pulse, we can calculate an approximate value of the in-plane magnetic field pulse H_x generated by the current-carrying

microcoils (as illustrated in Fig. 3.12) using the *Biot-Savart law*. This calculation is presented in Appendix C.

Fig. 3.13 shows a section of the applied voltage profile recorded with a digital oscilloscope. The rise time is roughly 250 ps. My research focuses on small-angle spin wave dynamics, which occurs in the 'region of interest' *after* the initial rising of the voltage pulse.

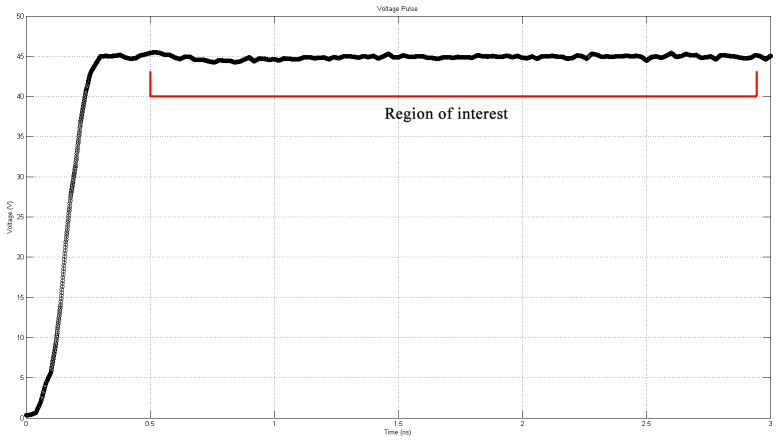

Figure 3.13: Applied voltage pulse.

Dynamic MOKE Setup

The complete dynamic MOKE setup is shown in Fig. 3.14. Equipment details are provided in Tab. B.4, Appendix B. A mode-locked Ti:Sapphire infrared pulse laser with 80 fs pulse duration and 80 MHz repetition rate was used as the synchronous source for both pump and probe branches. The pulse selector divides the repetition rate down to 0.8 MHz. *In addition* to previously mentioned features:

The pump beam is focused on a fast photodiode which generates a modulated ~ 2 ns, 0.8 MHz voltage signal, triggering the delay generator. The delay generator subsequently triggers the pulse generator which provides a $V_{pp} = 45$ V, 4 ns pump signal. The delay of the pump signal Δt is computer-controlled through the LabView/PCI interface.

The probe beam is focused on the sample through an $80\times$, numerical aperture (N.A.) $= 0.75$ lens to a spot of $\sim 1\,\mu$m at normal incidence. Two quadrant photodiodes (QPD) are setup in a differential scheme through a polarizing beam splitter (Wollaston prism) to enable vector magnetometry, with out-of-plane magnetization M_z provided by $s_1 - s_2$, and in-plane components M_x, M_y provided by $h_1 - h_2$ and

$v_1 - v_2$. Signal averaging is realized through an appropriate choice of the lock-in amplifier time constant[3].

The sample is mounted on a computer-controlled piezo flexure stage, allowing raster scanning of the sample surface for spatiotemporal magnetization imaging. Spatial resolution is determined by the N.A. of the objective and the wavelength λ of the laser from Rayleigh diffraction criterion

$$d = 1.22\frac{\lambda}{N.A.} = 1.22\frac{0.78\,\mu\text{m}}{0.75} \simeq 1.3\,\mu\text{m}. \tag{3.4}$$

3.2.5 X-Ray Diffraction Analysis

Magnetic properties are strongly influenced by crystal structure. The (111) texture (in the reciprocal lattice Miller notation) for example, is commonly associated with the antiferromagnetic phase [57].

X-rays 'see' a crystal lattice by having wavelengths comparable to lattice parameter a in a crystalline solid. The arrangement of a crystalline lattice can therefore be determined by analysing the angles and intensities of the diffracted X-ray peaks, which correspond to constructive interferences of scattered X-rays off successive crystallographic planes [58], as described by Bragg's Law

$$2d\sin\theta = n\lambda, \tag{3.5}$$

where d is the distance between successive (hkl) planes and θ is the scattering angle.

X-ray diffraction crystallography (XRD) was performed with a Siemens D500 diffractometer at IMS in Athens, Greece. Cu-K_α radiation with $\lambda = 1.5418\,$Åwas used in the $\theta - 2\theta$ geometry, from 20 to 90 degrees at 1 degree glancing incidence with respect to the sample surface. The X-ray penetration depth for this configuration can be calculated to be around $2\,\mu$m [59], sufficient to resolve crystal structure throughout the sample depth.

[3]The time constant is typically $\sim 100\,$ms, and at 0.8 MHz repetition rate, this means each output data point is the average of thousands of signals.

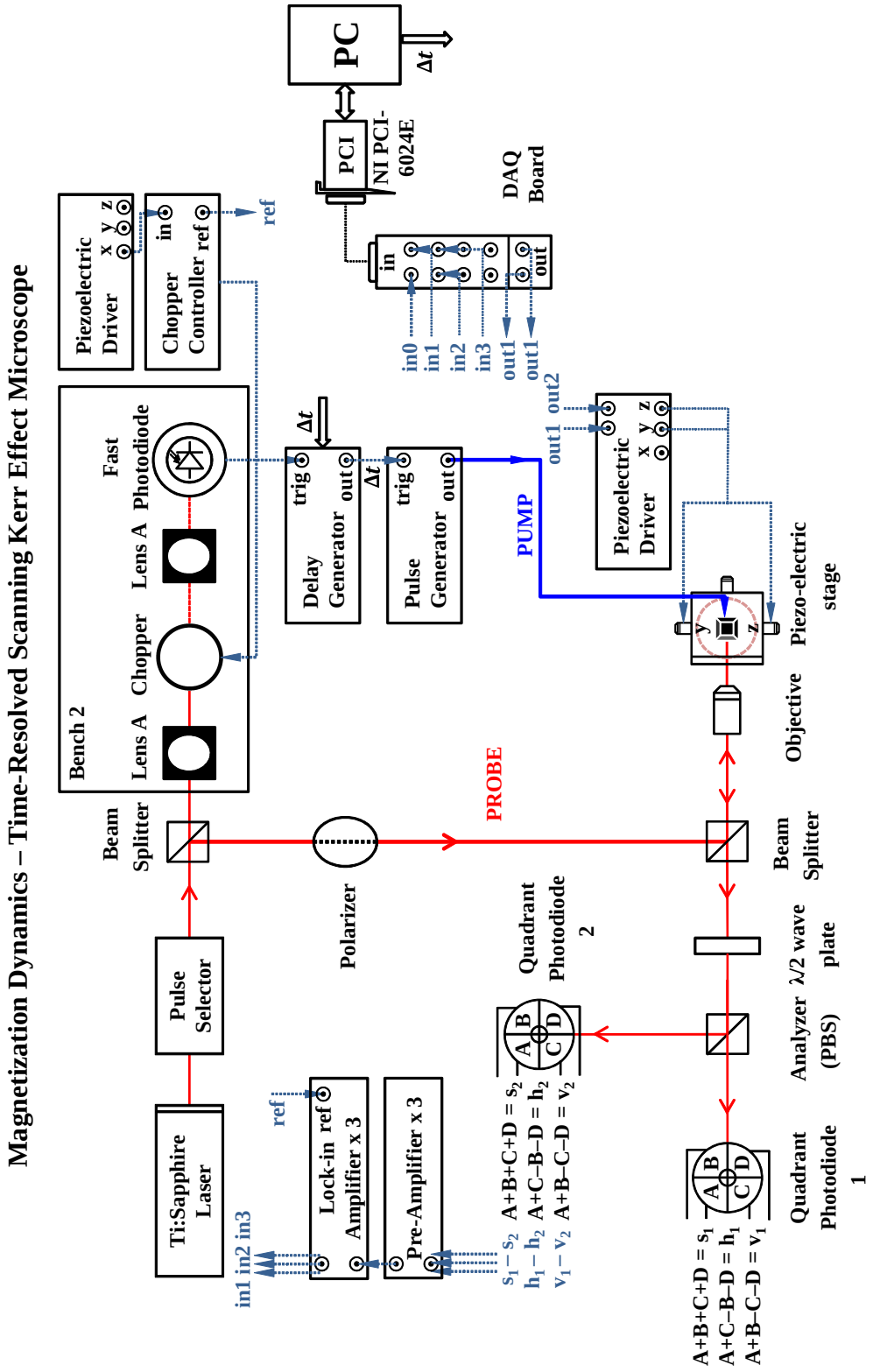

Figure 3.14: Dynamic MOKE Setup (detailed).

Chapter 4

Experimental Results

4.1 Overview

Arrays of 10 μm$\times$10 μm multi-layer squares with the general configuration of substrate/adhesion layer/FM-AF bilayer/capping layer[1] were fabricated on either Si/SiO_2 or 500 μm-thick borosilicate glass substrates via electron-beam lithography and DC-triode sputter deposition. For dynamic measurements, 20 μm-wide, 100 nm-thick gold microcoils were evaporated either directly on top of or below the magnetic squares. General sample arrangements are shown in Fig. 4.1.

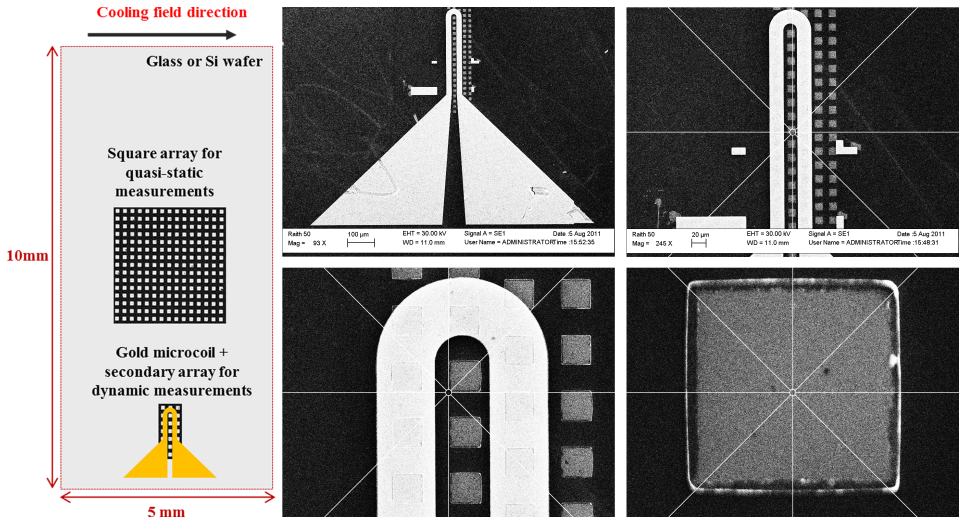

Figure 4.1: Sample wafer schematic and SEM images.

[1]The adhesion layer improves bonding between substrate and magnetic layers without compromising magnetic behavior while the capping layer prevents oxidation.

Several different layer configurations were used in order to explore different aspects of exchange bias. These are illustrated in Fig. 4.2.

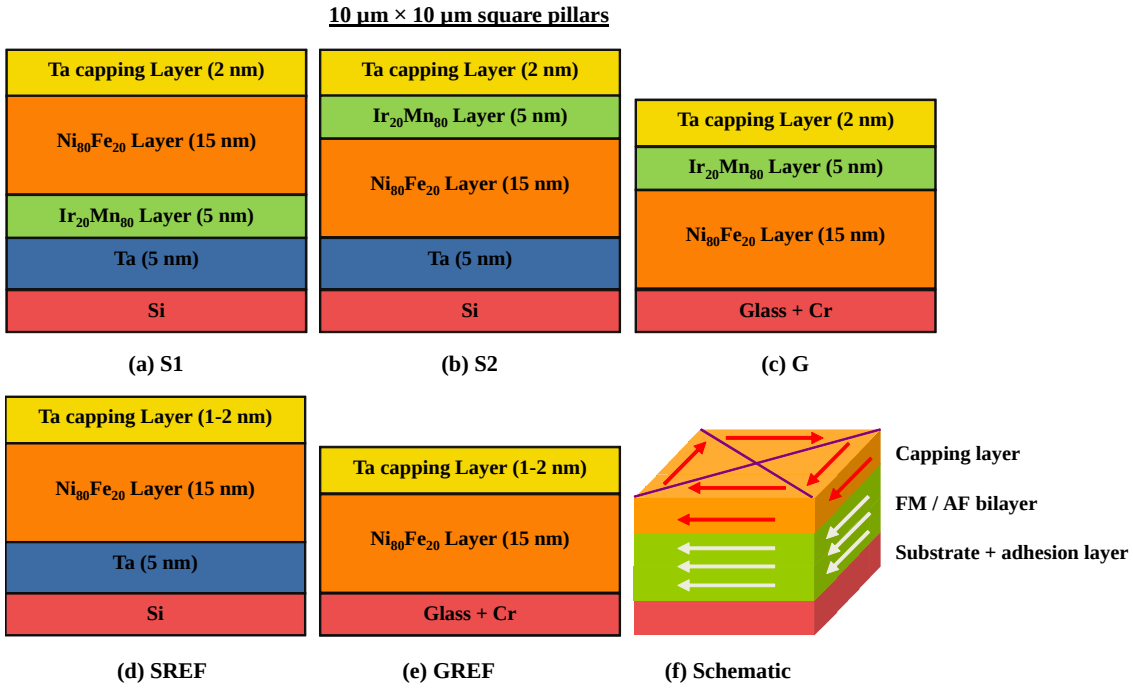

Figure 4.2: Schematics of fabricated structures.

(a) Si/Ta(5 nm)/$Ir_{20}Mn_{80}$(5 nm)/$Ni_{80}Fe_{20}$(15 nm)/Ta(2 nm), with silicon substrate and the ferromagnetic $Ni_{80}Fe_{20}$ (permalloy) deposited *after* the antiferromagnetic $Ir_{20}Mn_{80}$ (5 nm). Henceforward referred to as **sample S1**.

(b) Si/Ta(5 nm)/$Ni_{80}Fe_{20}$(15 nm)/$Ir_{20}Mn_{80}$(5 nm)/Ta(2 nm), with silicon substrate and the FM layer deposited *before* the AF layer. Henceforward referred to as **sample S2**[2].

(c) Glass/Cr(∼5 nm)/$Ni_{80}Fe_{20}$(15 nm)/$Ir_{20}Mn_{80}$(5 nm)/Ta(2 nm), same as S2 except with glass substrate, henceforward referred to as **sample G**.

(d) Si/Ta(5 nm)/$Ni_{80}Fe_{20}$(15 nm)/Ta(2 nm), single FM layer deposited on top of silicon, a reference sample for result comparison. Henceforward referred to as **sample SREF**.

[2]Only unpatterned films of this sample type were made, near the end of the research.

(e) Glass/Cr(∼5 nm)/$Ni_{80}Fe_{20}$(15 nm)/Ta(2 nm), single FM layer deposited on top of glass, a reference sample for result comparison. Henceforward referred to as **sample GREF**.

For sample S1, gold microcoils were *first* fabricated *underneath* the magnetic structures, and the MOKE laser reflects off the top FM surface of the sample; for sample G, gold microcoils were fabricated later, on top of existing magnetic structures, with the sample mounted *in reverse* for the MOKE laser to reflect off the bottom FM layer *through the glass substrate*. The rationale behind the chosen structural ordering in sample G will be made apparent in Chapter 5.

Our choice of ferromagnetic material, permalloy is widely used in industry and research for its high relative permeability and anisotropic magnetoresistance as well as low coercivity and magnetostriction. Likewise, $Ir_{20}Mn_{80}$ was chosen as the AF material for its high Néel Temperature ($T_N = 693\,\mathrm{K}$), exchange energy density ($J_{ex} \simeq 0.15\,\mathrm{erg/cm^2}$ for 50 Åof IrMn) and blocking temperature[3] (420–560 K for IrMn thicknesses between 2-10 Å), with the thickness of 5 nm experimentally observed to give maximum exchange bias [47, 60, 61, 62].

The fabricated samples were post-annealed at 450 K in a number of in-plane cooling fields along an edge of the square (Fig. 4.1), **which is taken as the $+x$ direction in subsequent experiments**. The cooling fields modify remanent FM magnetization, while the annealing temperature was set to above the experimentally determined blocking temperature of 420 K [37] in order to 'loosen up' the AF spins such that they align with the modified FM magnetization in accordance with exchange-bias theory.

The cooling fields used are listed in Tab. 4.1.

Sample Designation	Cooling fields (Oe)
S1	0, 50, 100, 150, 250, 300, 500
S2	n/a
G	0, 15, 40, 50, 100, 150, 200, 250, 300
SREF	0
GREF	0

Table 4.1: Sample cooling fields.

From now on I will adopt the naming convention of **sample code (S1/S2/G)-cooling field** when referencing a specific sample, e.g., *S1-150* refers to a sample with

[3]Strictly speaking, the blocking temperature it is not a property of the AF alone, but rather depends on the bilayer system

S1 configuration annealed in 150 Oe cooling field.

Film samples of identical configurations to S1, S2 and G were prepared for X-ray diffraction analysis, which are included in the next chapter along with simulation results for convenience.

4.2 Sample S1

4.2.1 Quasi-Static Results

Fig. 4.3 show the measured *easy-axis* (along the cooling field direction) as well as selected *hard-axis* (perpendicular to the cooling field direction) hysteresis loops of sample S1 under various annealing conditions.

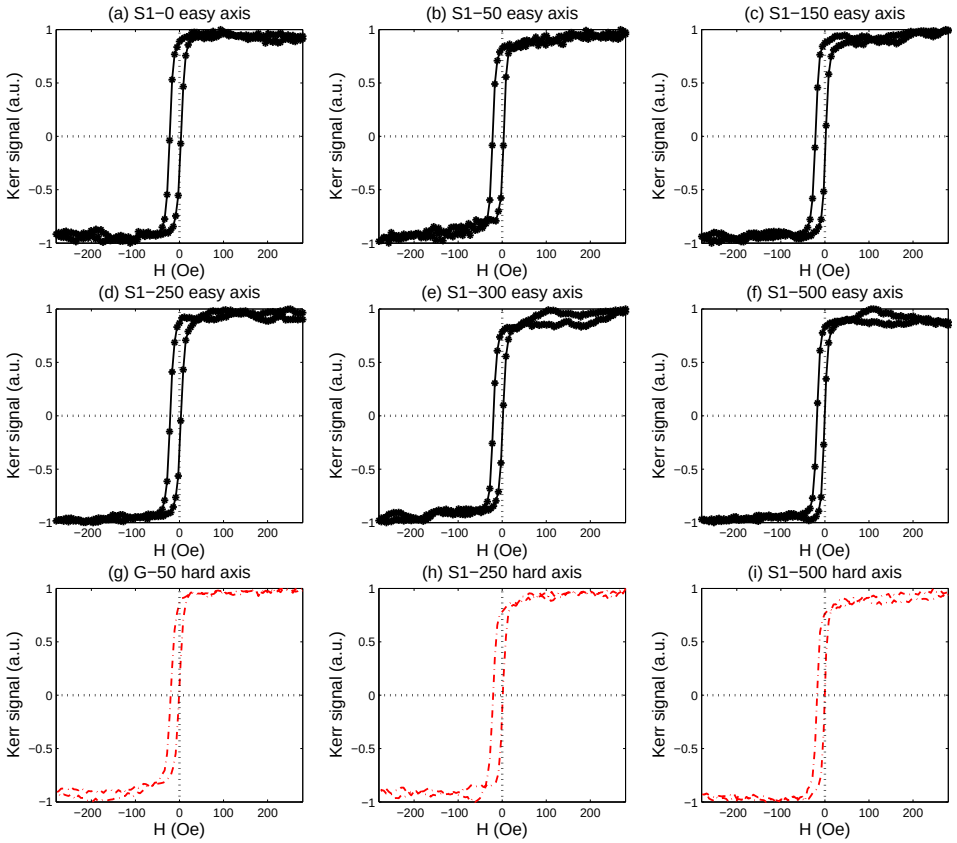

Figure 4.3: Easy-axis hysteresis for sample S1. (a),(b),(c),(d),(e),(f): 0, 50, 150, 250, 300, 500 Oe cooling fields (g),(h),(i): selected hard-axis hysteresis loops for 50, 250 and 500 Oe cooling fields.

In Fig. 4.4, the easy-axis hysteresis of the zero-field cooled (ZFC) S1-0 is plotted against (a) single-layer reference sample SREF and (b) S1-0 hard-axis hysteresis. The change in hysteresis behavior is negligible both between the exchange-biased and reference sample (a) and between the two axes of the exchange-biased sample (b).

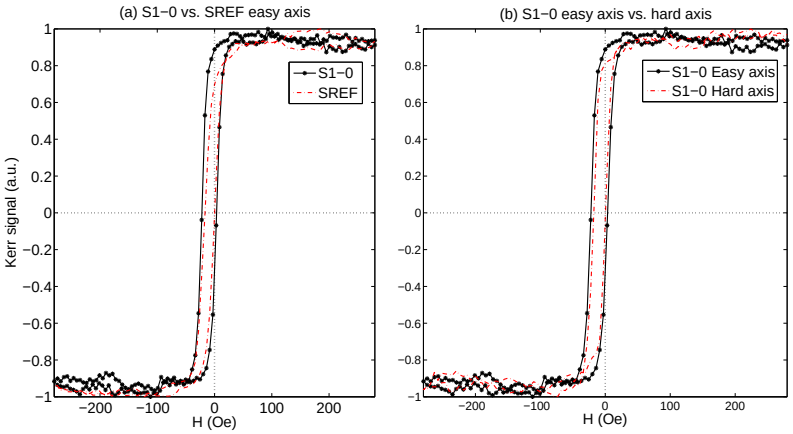

Figure 4.4: S1-0 vs. SREF. (a) easy axis hysteresis of S1-0 and SREF (b) easy vs. hard axis hysteresis for S1-0.

4.2.2 Dynamic Results

The way samples are arranged on gold microcoil is schematically shown in Fig. 4.5. As mentioned previously, the cooling field is in the $+x$ direction and excitation pulse fields are applied along the x-axis. From now on, a square will be referred to by its label in Fig. 4.5.

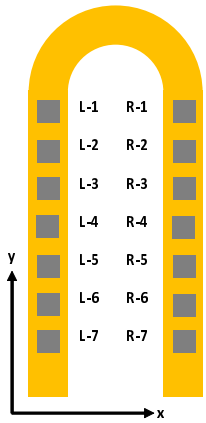

Figure 4.5: Samples on microcoil.

Fig. 4.6 shows a scanning Kerr image of sample S1-100-L-2 showing remnant magnetization in M_z. The dashed lines mark the boundary of the square. No apparent vortex or domain features are observed besides structural defects.

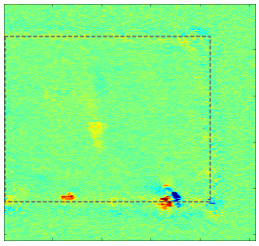

Figure 4.6: M_z profile of square S1-100-L-2.

All three components of magnetization (M_x, M_y and M_z) can be measured using the polarizing beam splitter and quadrant photodiode setup (Fig. 3.14). A typical 3-component temporal signal is shown in Fig. 4.7

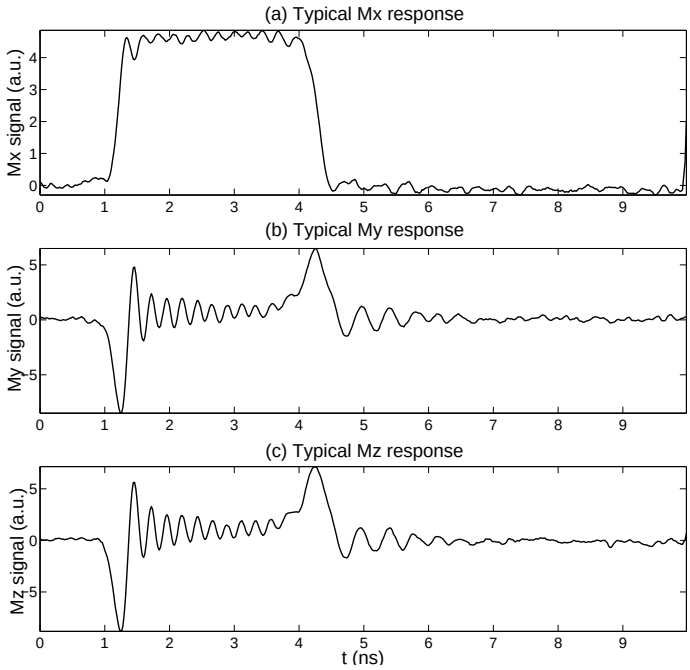

Figure 4.7: 3-component temporal signal.

In practice, MOKE signals are very sensitive to photodiode balance and obtaining all three components of magnetization simultaneously can be difficult. Nevertheless, since M_i is the projection of the magnetization $\mathbf{M}$ along the ith axis, its frequency

characteristics should be identical to that of **M**. In actual experiments, only a single component of magnetization was recorded and analyzed.

The temporal dynamics of three S1 samples, namely S1-100, S1-150 and S1-200 were investigated over a number of squares (L-2, R-3 etc. in Fig. 4.5). Fig. 4.8 show temporal profiles and corresponding fast Fourier transform (FFT) plots for M_z, with a field pulse H_{pulse} in the $-x$ direction, measured at the center of the squares.

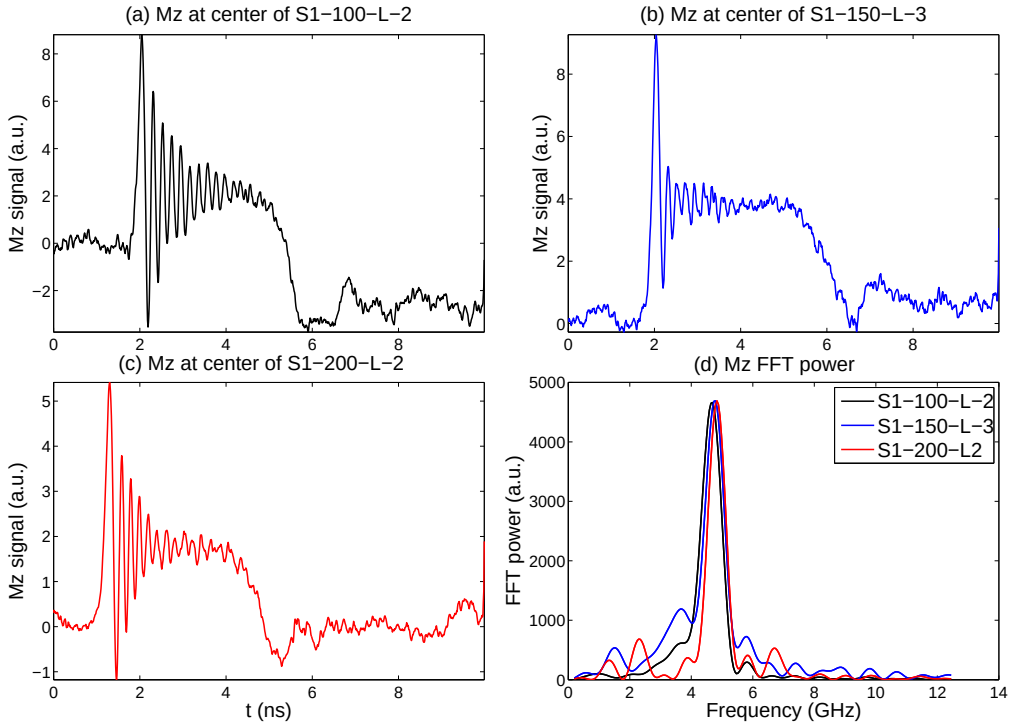

Figure 4.8: Temporal dynamics for (a) S1-100-L-2 (b) S1-150-L-3 and (c) S1-200-L-2. FFT plots are shown in (d).

The temporal data was captured at 10 ps resolution (100 GHz sampling frequency), and the 1024-point FFT has spectral resolution $\simeq \pm 0.1$ GHz. The GHz FFT peaks, corresponding to magnetization precession, appear identical in all three samples.

I then investigated the variation of FFT peak frequency under an external field along the x-direction. Since all S1 samples show very similar quasi-static and dynamic behavior regardless of cooling field, Only a single sample square (S1-200-R-6) was used. First, M_z profiles for S1-200-R-6 in response to H_{pulse} in both the $+x$ (red) and $-x$ (blue) directions in the absence of any external field H_{ext} were recorded and shown in Fig. 4.9.

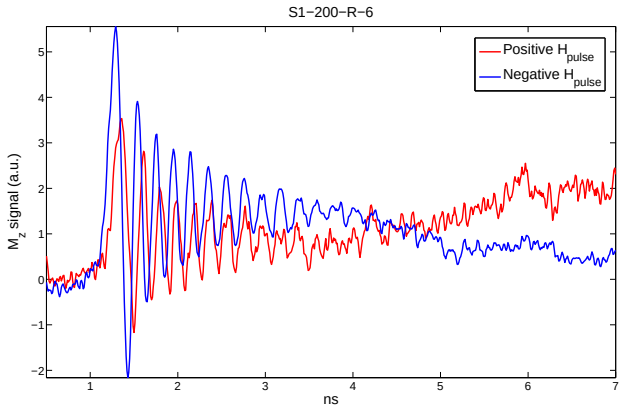

Figure 4.9: M_z in response to H_{pulse} in $\pm x$ for S1-200-R-6, $H_{\text{ext}} = 0\,\text{Oe}$.

Notice the preferential excitation direction with greater signal strength for H_{pulse} in the $-x$ direction. This can be explained by noting that we expect the $+x$ cooling field during annealing to create net magnetic ordering (i.e. exchange-bias field H_{eb}) pointing in the $+x$ direction in the samples. The stronger signal occurs when H_{pulse} points in the *opposite direction* to this ordering, which is expected: sample magnetization are excited only if pushed in a direction different from their equilibrium orientation.

M_z profiles were then recorded for a $-x$ H_{ext} between 0 Oe and 200 Oe. The results are shown in Fig. 4.10. The strengths and directions of the various fields in Fig. 4.10 are shown in the corresponding schematic, Fig. 4.11 to help interpret the results.

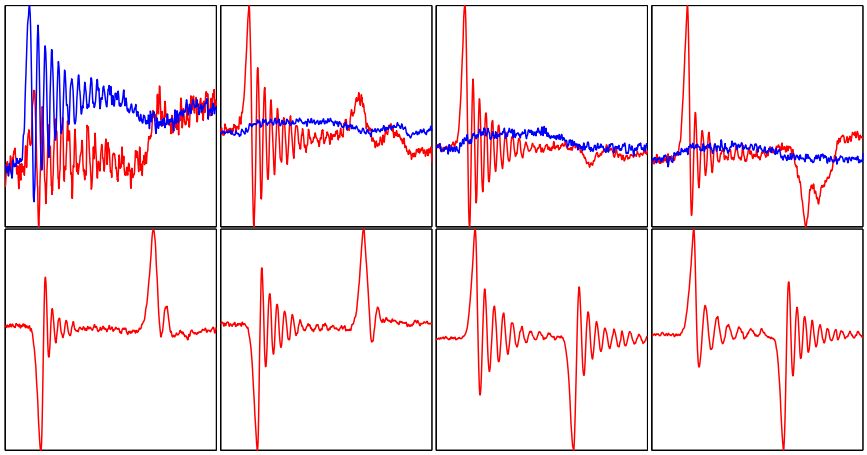

Figure 4.10: M_z in response to H_{pulse} in $+x$ (red) and $-x$ (blue) for S1-200-R-6.

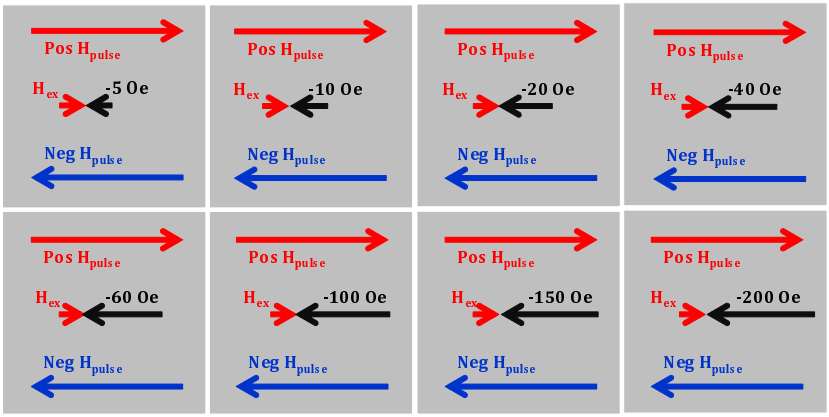

Figure 4.11: Schematic for the relative magnitudes and directions of magnetic fields present in Fig. 4.10.

Note that the spikes and subsequent oscillation near the tail-end of the signals in Fig. 4.10 are a result of the abrupt termination of the excitation pulse. The preferential excitation of M_z in response to a $-x$ H_{pulse} observed in zero H_{ext} (Fig. 4.9) disappears under an external field of 10 Oe pointing in the opposite direction. This implies that the $+x$ H_{eb}/net magnetic ordering created through thermomagnetic annealing is very weak and can be overcome by a small, 10 Oe external bias field pointing in $-x$. The overall bias field and sample magnetization ordering thus point in the $-x$ direction for $|H_{\text{ext}}| \geq 10$ Oe, and a meaningful M_z signal only exists for H_{pulse} in the $+x$ direction (red).

4.3 Sample G

4.3.1 Prior Work

Samples GREF, G-0, G-15 and G-40 were previously fabricated and measured by two other members of the research group, Jonathan Rudge and Emad Girgis [40] under slightly different experimental parameters[4]. Static results are shown in Fig. 4.12, with remanent vortex states measured using the scanning mode of the Kerr effect microscope shown as insets. Local domain magnetization are represented through

[4]Their FM layer was 12 nm thick, and the annealing temperature was 600 K, later deemed unnecessarily high. The static and dynamic setup was also slightly different, but inconsequential to the obtained results.

the color contrast in the Kerr images. The dashed lines and arrows serve as aids to the visualization of the domain magnetization.

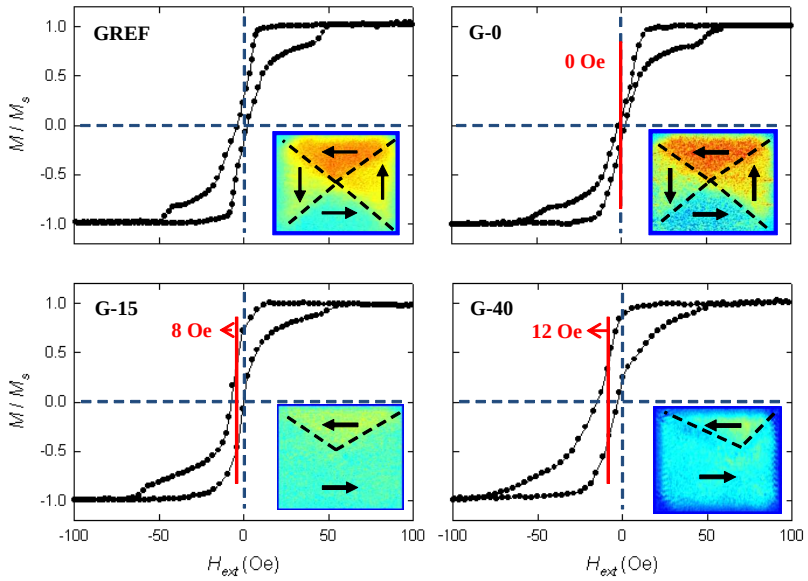

Figure 4.12: Previously obtained hysteresis results and remnant vortex configuration.

In the case of the zero-field cooled G-0, the fourfold symmetry of the Landau vortex state is unbroken, therefore no hysteresis shift is observed. When the cooling field is increased above zero, the vortex core is displaced from the center, and the hysteresis loops show a distinguished increase in shift (marked in red). It is evident that these G samples were annealed in *non-saturating cooling fields* such that the remanent vortex magnetization is retained.

The temporal profiles of M_x in response to H_{pulse} in $-x$ for the same samples are shown in Fig. 4.13, with the corresponding FFT profiles shown in Fig. 4.14. The signals are measured over a laser spot positioned in the lower quadrant of the squares, as indicated by the red dot in Fig. 4.13. In each case, the magnetization undergoes rapid initial large-angle switching towards the direction of H_{pulse}, followed by small-angle damped precession towards equilibrium. The details of the precession dynamics are determined by the cooling-field modified remanent magnetization profile, as evidenced by the shift in FFT peak frequencies. This will be discussed in more detail in Chapter 6.

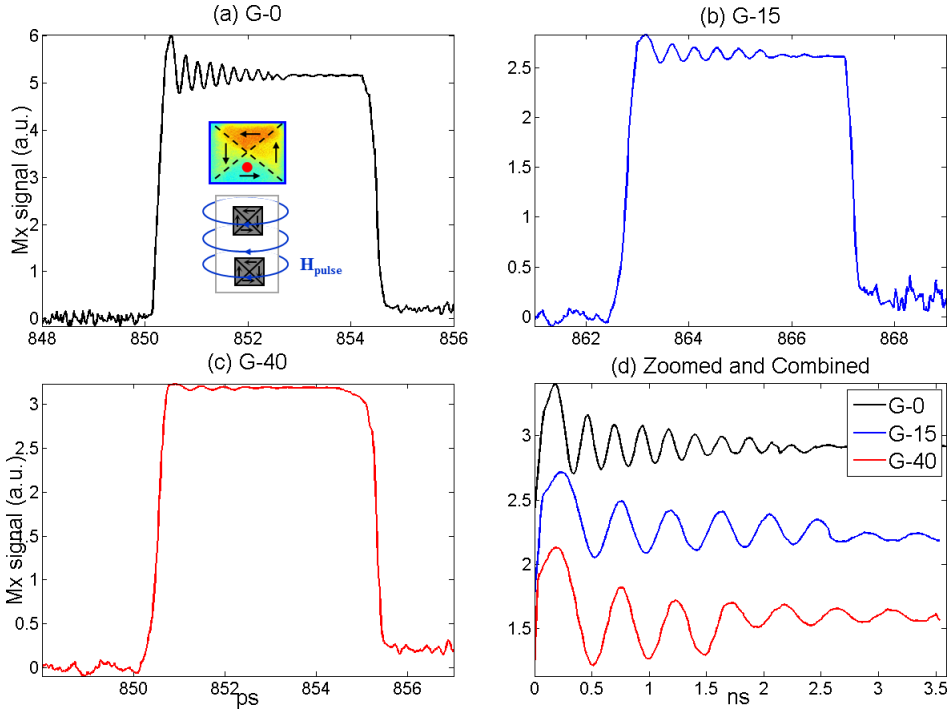

Figure 4.13: Previously obtained dynamic M_x data.

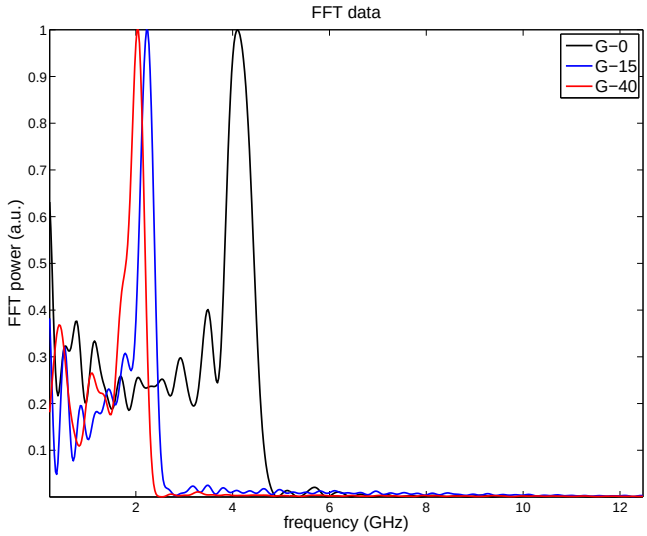

Figure 4.14: FFT plots.

4.3.2 Quasi-Static Results

Fig. 4.15 show the easy- and hard-axis hysteresis plots for sample G with cooling fields ≥ 50 Oe.

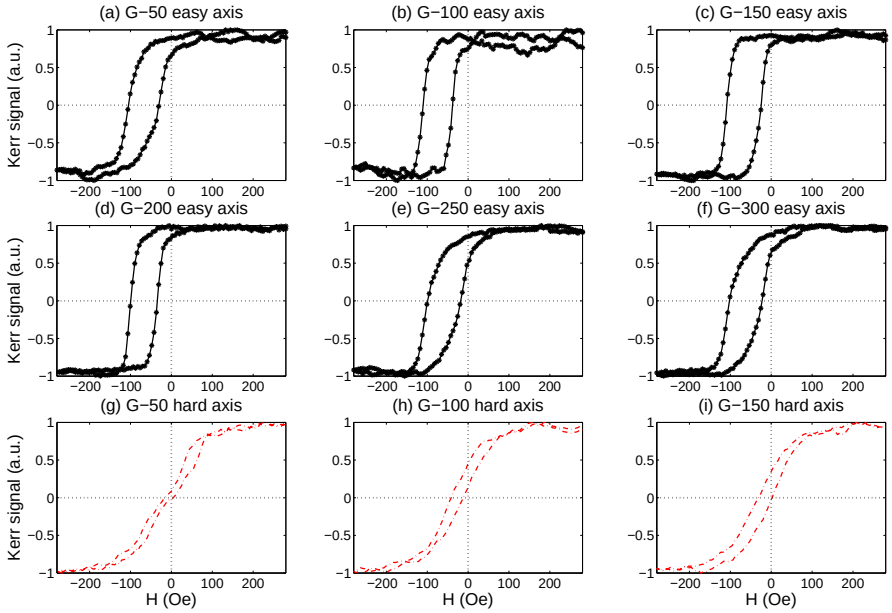

Figure 4.15: Hysteresis results for sample G. (a),(b),(c),(d),(e),(f): easy-axis hysteresis with cooling fields of 50, 100, 150, 200, 250 and 300 Oe respectively (g),(h),(i): selected hard-axis hysteresis for 50, 100 and 150 Oe cooling fields.

The hysteresis curve for sample GREF in Fig. 4.12 shows a saturation point at $\simeq 50$ Oe, therefore the G samples shown in Fig. 4.15 can be regarded as annealed in *saturating cooling fields* such that they possess a more or less saturated domain profile at remanence, as confirmed by the scanning Kerr image, Fig. 4.16.

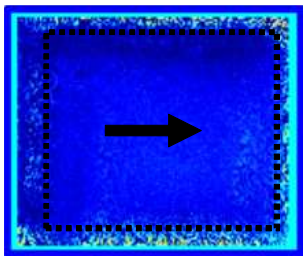

Figure 4.16: Typical scanning Kerr image for sample G with saturating cooling field.

4.3.3 Dynamic Results

Repeated attempts were made to measure the temporal response M_z for G samples under varying H_{ext}. Unfortunately, since the FM is the *bottom* layer, underneath both AF and the gold microcoils, the probing laser must shine through the glass in order to reflect off its surface, and the process introduces too much noise to the signal for the extraction of meaningful dynamic information, as shown in a typical measurement in Fig. 4.17. The dynamic details of G samples annealed in saturating cooling fields will instead be investigated with the aid of numerical modeling in Chapter 5.

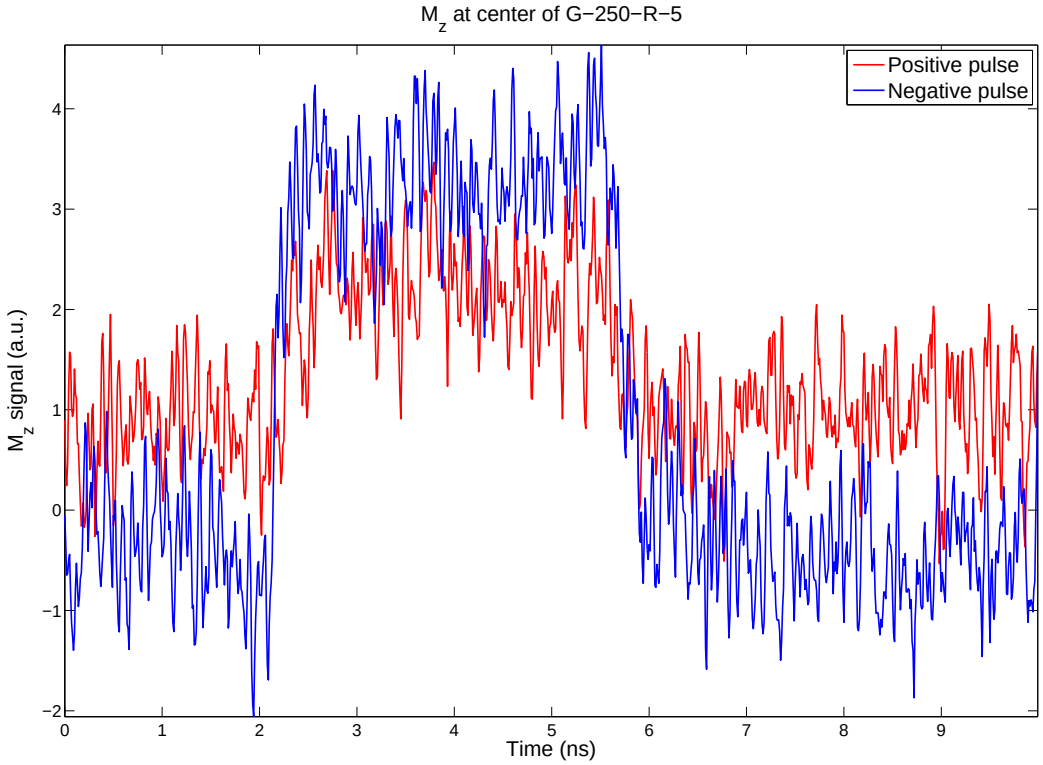

Figure 4.17: M_z in response to H_{pulse} in $+x$ (red) and $-x$ (blue) for G-250-R-5, $H_{\text{ext}} = 0$.

Chapter 5

Analysis

5.1 Sample S1

The hysteretic behavior of sample S1 as a function of cooling field is summarized in Fig. 5.1.

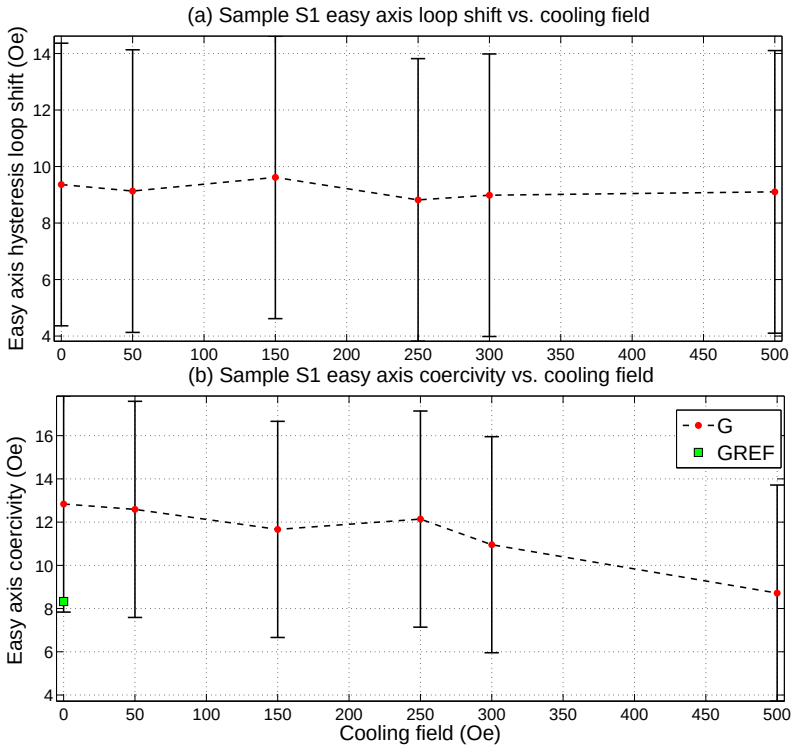

Figure 5.1: Easy axis hysteresis behavior as a function of cooling field. (a) Loop shift (b) Coercivity. Reference sample SREF is shown in (b) as green square.

Considering the uncertainty in field measurements ($\simeq \pm 5\,\mathrm{Oe}$), the cooling fields do not appear to produce an appreciable hysteresis loop shift in sample S1 (Fig. 5.1(a)). There does however seem to be a very slight decrease in coercivity with increasing cooling field (Fig. 5.1(b)), indicating a more coherent switching process possibly owing to a more homogeneous overall magnetic ordering obtained during annealing in larger cooling fields.

In the dynamic regime, the various samples again show little changes in precessional frequency in their M_z response, as evident from the FFT plots in Fig. 4.8(d). To confirm this, further measurements were performed for a number of other squares in samples S1-100, S1-150 and S1-200, and the FFT peak frequencies vs. cooling field relation is summarized in Fig. 5.2, with artificial scatter added to the cooling field axis to enhance visualization. Once again, considering the $\pm 0.1\,\mathrm{GHz}$ uncertainty in FFT frequency, there seems to be little change in the precessional frequency with increasing cooling fields.

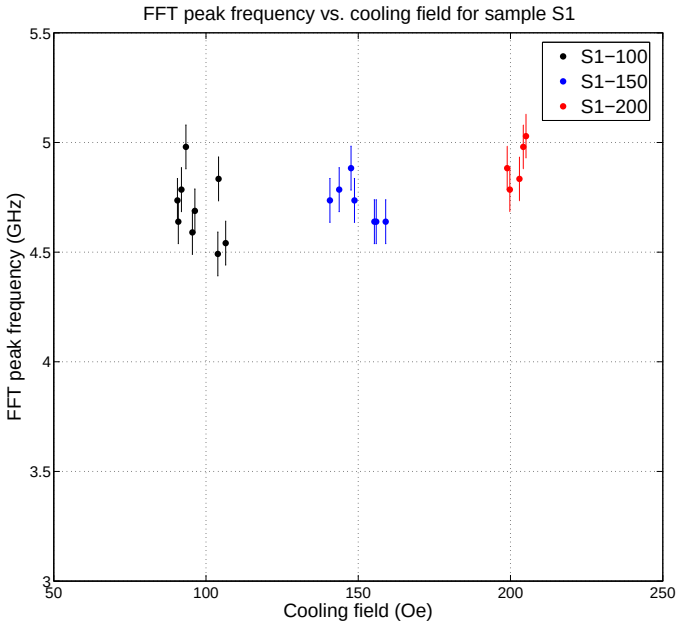

Figure 5.2: M_z FFT peak frequency vs. cooling field for sample S1.

The cooling field however does seem to play a small role in the dynamic regime. As mentioned in Chapter 4, sample S1-200-R-6 exhibits preferential switching in $-x$, corresponding to $H_{\mathrm{eb}} \leq 10\,\mathrm{Oe}$ in $+x$, in the direction of the cooling field (Fig. 4.10 and 4.11). A more reliable estimate of H_{eb} can be obtained using the value of H_{pulse}

calculated in Appendix C and fitting the M_z FFT peak frequency vs. H_{ext} relation from Fig. 4.10 to the Herring-Kittel formula (1.53)

$$f = \frac{\mu_o \gamma}{2\pi} \sqrt{(H + H_{\text{ext}})(H + H_{\text{ext}} + M_s)}, \tag{5.1}$$

where

$$\mu_o \gamma = 0.23\,\text{GHz}(\text{kA/m})^{-1}$$
$$M_s \simeq 800\,\text{kA/m}$$
$$1\,\text{kA/m} = 4\pi\,\text{Oe}, \tag{5.2}$$
$$\tag{5.3}$$

and

$$H = \begin{cases} H_{\text{pulse}} + H_{\text{eb}} & \text{if the field pulse is in} + x; \\ H_{\text{pulse}} - H_{\text{eb}} & \text{if the field pulse is in} - x. \end{cases} \tag{5.4}$$

Non-linear least-squares fitting was performed using the Levenberg-Marquardt algorithm with H_{eff} and M_s in (5.1) as optimization variables. The results are summarized in Tab. 5.1 and Fig. 5.3. Note field values are rounded to the nearest integer.

H_{pulse} polarity	+
H_{ext} polarity	–
H_{eb} polarity	+
H_{pulse}	258 Oe (see Appendix C)
H	279±15 Oe
H_{eb}	(21±15) Oe
M_s	(856±55) kA/m
Coefficient of determination R^2	0.9949

Table 5.1: Leas-squares curve fitting results.

The results are consistent with the previously estimated $H_{\text{eb}} \leq 10\,\text{Oe}$, within the limits of experimental uncertainty.

In summary, whether it is in the quasi-static or dynamic measurements we see very little exchange-bias effect in sample S1. Neither thermomagnetic annealing nor the additional AF layer seem to change the overall magnetic behavior of the bilayer samples when compared to the single-layer SREF. These rather unexpected observa-

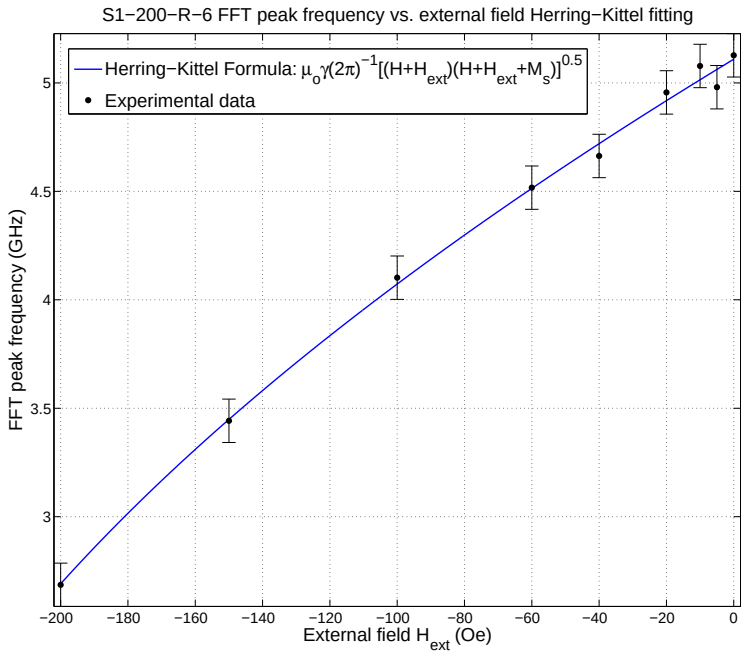

Figure 5.3: Least-squares fitting for S1-200-R6 with positive H_{pulse} and negative H_{ext} combination.

tions can be understood by considering the different sputter deposition procedures used for sample S1, S2 and G, and how these procedures influence the texture and spin alignment in the AF layer.

5.1.1 Deposition Order vs. AF texture and Spin Alignment

The magnetic lattice configuration (texture) of antiferromagnetic materials can be investigated using powder neutron diffraction techniques. The principle is similar to X-ray diffraction, except the interaction between neutrons and specimen nuclei is magnetic in nature. Studies show that antiferromagnetism in A-type antiferromagnets are associated with the (111) texture, in which magnetic moments are arranged in ferromagnetic sheets (submotifs) parallel to the (111) planes, and the magnetization between neighboring sheets are antiparallel [57]. A schematic is shown in Fig. 5.4.

The development of exchange bias in $Ni_{80}Fe_{20}/Ir_{20}Mn_{80}$ bilayers is strongly dependent on the formation of the (111) texture in IrMn [61][1], which in turn depends on the crystallinity of the *underlying seed layer* during its growth. Our FM layer

[1] As the % compositions are the same for all samples, I will omit the subscripts for convenience.

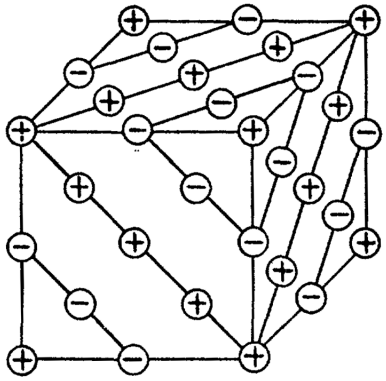

Figure 5.4: Arrangement of AF submotifs in the (111) texture, from Roth [57].

material NiFe is excellent for this purpose, as just $\sim 5\,\mathrm{nm}$ of NiFe greatly enhances (111) growth in a large number of AF materials [47, 63]. Furthermore, the ion energy-enhanced mobility at the FM surface during sputter deposition can cause mobile FM adatom pairs to orient along local energy minima, giving rise to significant spin ordering in the FM layer even under small magnetron stray fields [64, 65]. If an AF layer is deposited on top of the ordered FM, it will not adopt the usual compensated spin structure (Fig. 2.5(a)), instead, its spins will tend to align with the FM, creating the uncompensated net spin ordering in the first few AF atomic layers (Fig. 2.5(b)) which is necessary for exchange bias.

However, for optical access to the FM layer in sample S1, the FM layer was deposited *on top of* the AF , in a reversed substrate/AF/FM configuration (Fig. 4.2(a)). In this case, the AF layer is deposited directly on the Ta adhesion layer, which does not adequately promote the growth of (111) texture. Furthermore, the rigid, compensated AF spin structure formed during deposition can not be easily realigned to the FM layer spin ordering. In fact, in a role reversal, the spins in the first several atomic layers of *FM* are now aligned to the AF order, becoming partially compensated. The AF spins near the interface thus have little net ordering and contribute negligibly to the overall exchange bias. The effect of layer deposition order on spin alignment is illustrated in Fig. 5.5.

We therefore expect samples with substrate/FM/AF structure (e.g. S2 and G) to exhibit good AF texture and large exchange-bias loop shift; while samples with substrate/AF/FM structure (e.g. S1) should show little AF texture and negligible exchange-bias loop shift.

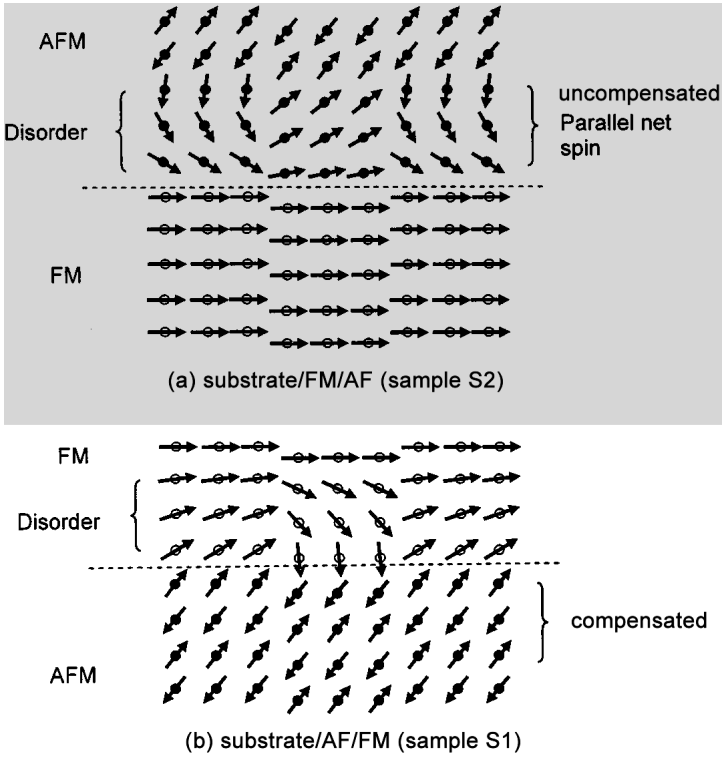

Figure 5.5: FM/AF interfacial spin alignment vs. layer deposition order (a) substrate/FM/AF (b) substrate/AF/FM. From Sankaranarayanan et al. [47].

5.1.2 XRD Results

AF textures in *as-deposited* (i.e. no annealing) films with S1, S2 and G configurations were measured using X-ray diffraction, and the results are shown in Fig. 5.6. The peaks are identified by element as well as texture in terms of Miller indices. Several trends are observed:

1. Sharpness of NiFe (111) peak: S2>S1>G.
2. Bragg angle θ of NiFe (111) peak: S2>S1>G.
3. IrMn (111) peak only exists for S2.

The average size of diffracting crystallites can be calculated from the position and broadening of the XRD peaks according to Scherrer's formula [66]

$$\tau = \frac{K\lambda}{\beta \cos\theta}, \tag{5.5}$$

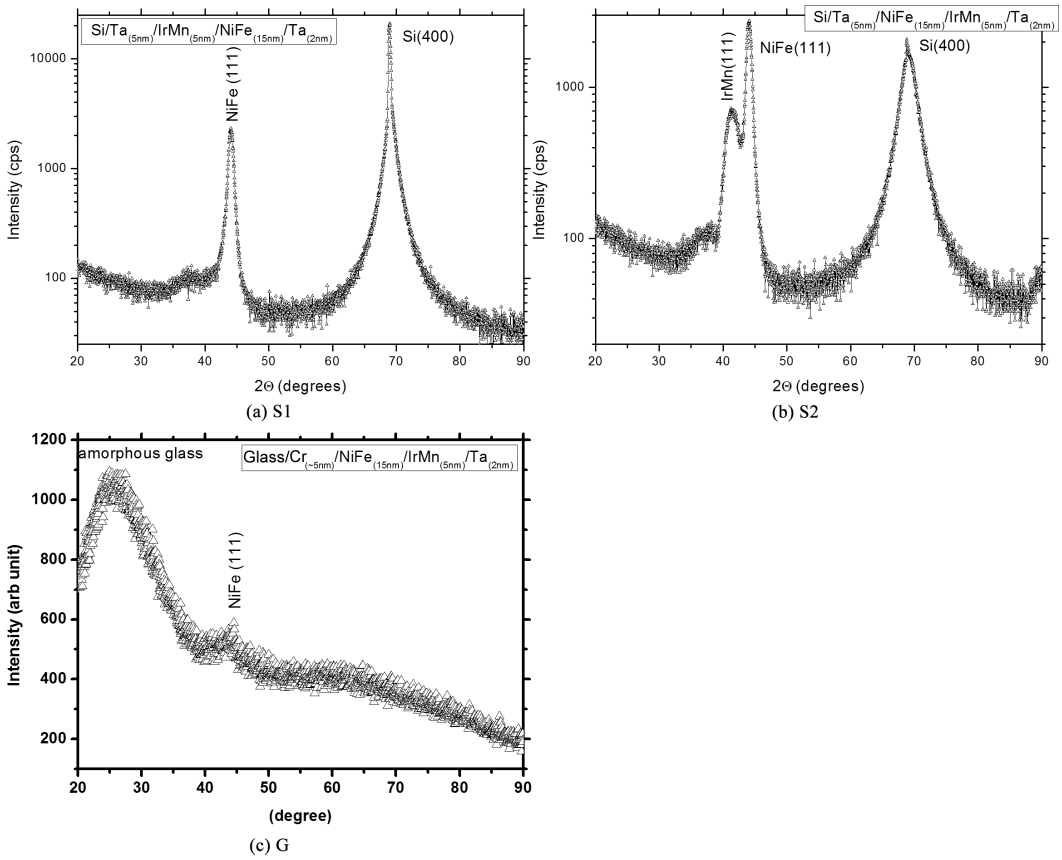

Figure 5.6: $\theta - 2\theta$ XRD results for (a) S1, (b) S2 and (c) G

where $K \simeq 0.9$ is the crystallite shape factor, λ is the X-ray wavelength, θ is the Bragg angle and β is the full width at half maximum of a diffraction peak. Better texture is associated with smaller β and larger θ.

As expected, the best texture (sharpest peak with the largest Bragg angle) is observed in sample S2 (Si/FM/AF, Fig. 4.2(b)). The (400) texture of the silicon substrate and Ta seed layer promotes the development of (111) texture in the NiFe layer [61, 67], which in turn seeds the growth of (111) texture and net spin ordering in the IrMn layer. In the case of sample S1 (substrate/AF/FM, Fig. 4.2(a)), there is indeed no IrMn (111) peak, thus justifying our previous MOKE measurements. The texture in the NiFe layer is also consequently worse, as demonstrated by the broadening of the NiFe peak. In the case of sample G (glass/FM/AF, Fig. 4.2(c)), despite having the exchange-bias inducing FM→AF deposition order, the underlying amorphous glass substrate (large, broad XRD peak) inhibits the growth of (111) texture in both NiFe and IrMn layers, leading to poor structural consistency and

small coherence lengths. Despite lacking texture, the correct deposition order means that the FM layer can still induce net spin ordering in the AF layer at the interface.

SEM images also verify the XRD results (Fig. 5.7 and 5.8), with minimum roughness in sample S2 and maximum in sample G.

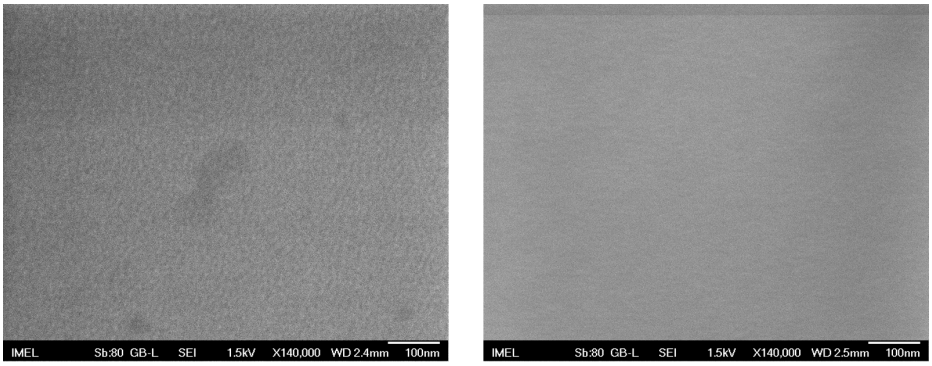

(a) S1 140k FE-SEM Micrograph (b) S2 140k FE-SEM Micrograph

Figure 5.7: SEM micrographs of film samples of S1 and S2 at 140k magnification.

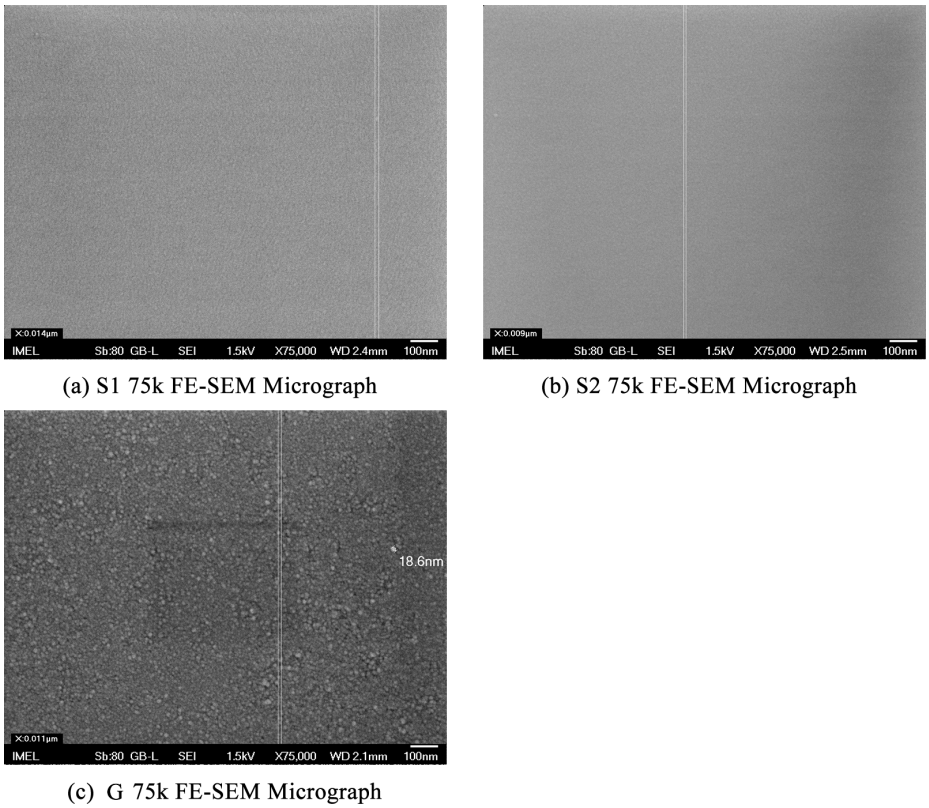

(a) S1 75k FE-SEM Micrograph (b) S2 75k FE-SEM Micrograph

(c) G 75k FE-SEM Micrograph

Figure 5.8: SEM micrographs of film samples of S1, S2 and G at 75k magnification.

The magnetic consequences of texture and spin alignment variations are neatly summarized in the hysteresis measurements of Fig. 5.9 for as-deposited film samples.

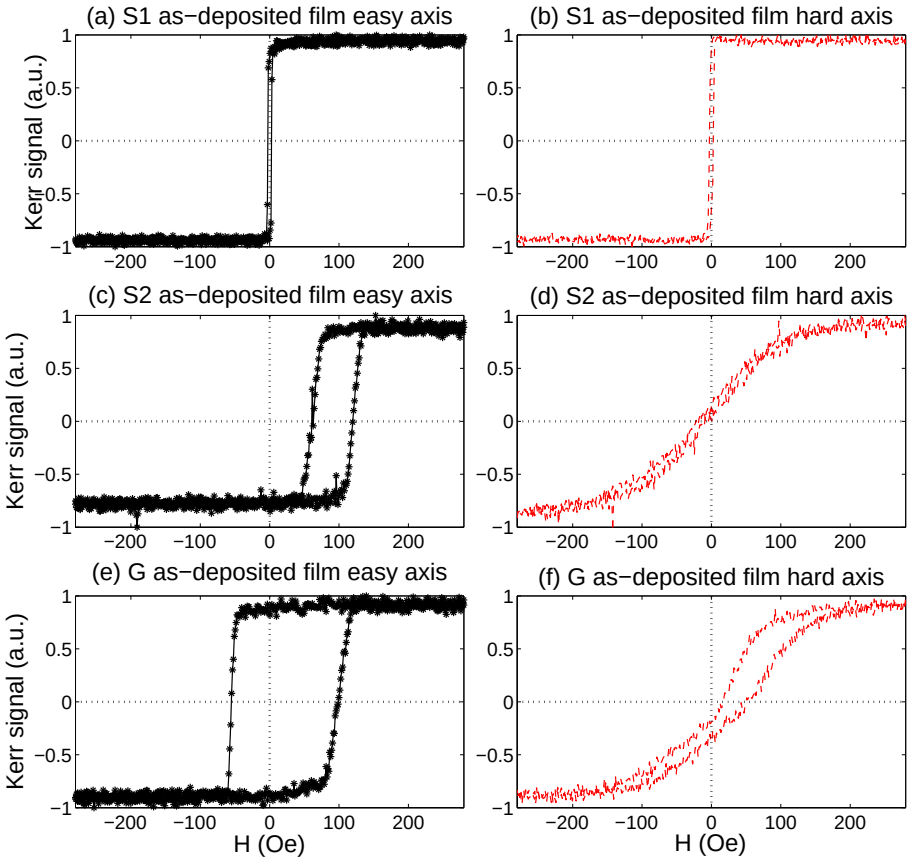

Figure 5.9: As-deposited film sample hysteresis.

Sample S2, having both AF (111) texture and interfacial spin alignment, exhibits large hysteresis loop shift in the easy-axis direction. Sample S1, having neither, shows typical behavior of single-layer polycrystalline NiFe film, with no distinct easy- or hard-axis (i.e. random anisotropy). The effect of the AF layer on FM in S1 is negligibly small. Sample G, lacking in AF (111) texture but making up for it in interfacial spin alignment, shows weak exchange-bias in the form of a small hysteresis loop shift and large coercivity as the result of its structural inhomogeneity[2].

[2]The large coercivity of the as-deposited G sample (Fig. 5.9(e)) can be reduced through annealing (see Fig. 4.15), which improves texture and relaxes the metastable AF configuration [60, 64]. The process also improves exchange bias, and the effect is particularly pronounced in systems with poor as-deposited texture, such as films grown on amorphous substrates similar to sample G [63].

The results so far show that the choice of substrate, adhesion layer and FM/AF deposition order are of great importance in determining the crystal texture and spin orientation, and hence exchange bias. In optimizing fabrication conditions, we are often constrained by instrumentation considerations - in our case, the need for optical access to the FM layer necessitates a sub-optimal fabrication compromise: the use of amorphous glass substrates.

5.2 Micromagnetic Modeling

Briefly introduced in Chapter 1, micromagnetic modeling refers to the general numerical approach towards solving LLG equations and is a versatile platform for the implementation of experiments in an idealized setting. The validity of a theoretical model can be tested against experimental results; in turn, experimental data can be justified through simulations based on a proven model. By bypassing numerous practical limitations, modeling can expand upon existing experiments, providing additional insight, or just additional resolution.

Numerical modeling was performed using the Windows-based proprietary LLG Micromagnetic Simulator [30]. A $Ni_{80}Fe_{20}$ square element with $2\,\mu$m sides and 20 nm thickness was subdivided into cubic unit cells of length 10 nm, compatible with $l_{ex} \simeq 5 - 10$ nm [13]. Due to limited computing resources, a compromise had to be made between the element and unit cell sizes. The reduced size of the simulation element from the actual sample means that the experimental and simulation data can only be compared *qualitatively*. Standard bulk material parameters for $Ni_{80}Fe_{20}$ were used in accordance with existing literature [37, 38]. These are listed in Tab. 5.2.

Simulated hysteresis was performed under a ± 450 Oe in-plane sweeping field. In dynamic simulations, small-angle spin-wave dynamics was investigated using a 20 Oe, 2 ns magnetic pulse along the $-x$-direction, constructed from the measured pulse generator voltage profile in Fig. 3.13. The magnetic pulse perturbs, but does not completely switch the sample magnetization[3]. This was done in partial consideration to minimize edge effects such as reflection, which becomes quite prominent in the simulated sample due to its reduced size. Measurements were averaged over a small circular area below the center, similar to the experiments (See Fig. 4.13(a)).

[3]This is equivalent to exciting the sample with a large switching pulse, then observing the post-switching small-angle dynamics once the initial rising voltage pulse has stabilized. Refer to 'region of interest' marked in Fig. 3.13.

Magnetic Quantity (Unit)	**Value**
Saturation magnetization M_s (emu/cm^3)	800
Exchange stiffness A (μerg/cm)	1.05
Anisotropy (erg/cm^3)	negligible
Gilbert damping constant α	0.008

Table 5.2: Material parameters for $Ni_{80}Fe_{20}$ used in simulation.

The AF layer was not modeled directly, as no current recipe describing the exact spin structure in the AF layer exists. Instead, the *influence of the AF layer* was represented through the interfacial exchange-bias field, which enters the model as a position-dependent pinning field adjacent to the FM layer. Since the exchange-bias field is essentially a copy of the FM remanent magnetization, the pinning field was constructed from the remanent domain profile of a single layer FM, relaxed in the appropriate in-plane cooling field in $+x$ [37]. The pinning field profiles used in the simulations are collectively shown in Fig. 5.10. The strength of the pinning field was fixed at 90 Oe, matched to the experimentally observed hysteresis loop shift under a large saturating field, as discussed in Hoffmann et al. [38], Sort et al. [37]. Irregularities introduced during the fabrication process were modeled as a random thermal noise at 300 K, as illustrated in Fig. 5.11.

From Fig. 5.10, we see as the $+x$ cooling field expands the bottom domain with $+x$ magnetization, leading to modified remanent domain and exchange-bias field profiles with the vortex core displaced upwards. The core is eventually driven out of the sample by a cooling field $\geq$ 150 Oe[4], and the sample ends up with a saturated remanent domain/exchange-bias field profile. Field directions and other conventions used in the simulation are chosen to be in agreement with experiments (cf. insets from Fig. 4.12).

[4]Compared to $\simeq$ 50 Oe in experiments. All field values are scaled from their experimental counterparts due to reduced sample size in simulation.

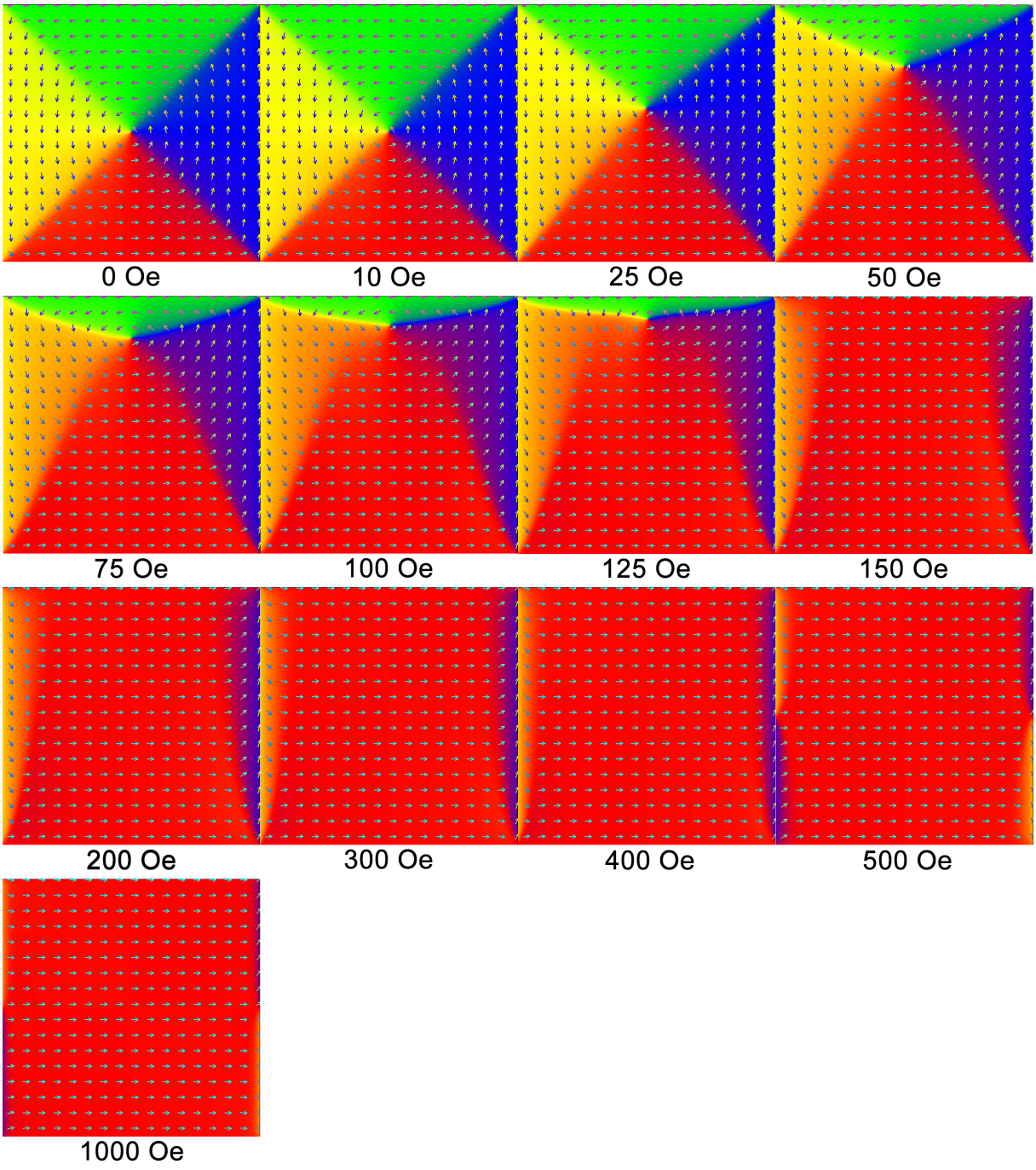

Figure 5.10: Simulated remanent domain and pinning field profiles at 0-1000 Oe cooling fields. Local magnetization direction represented through arrows and colors.

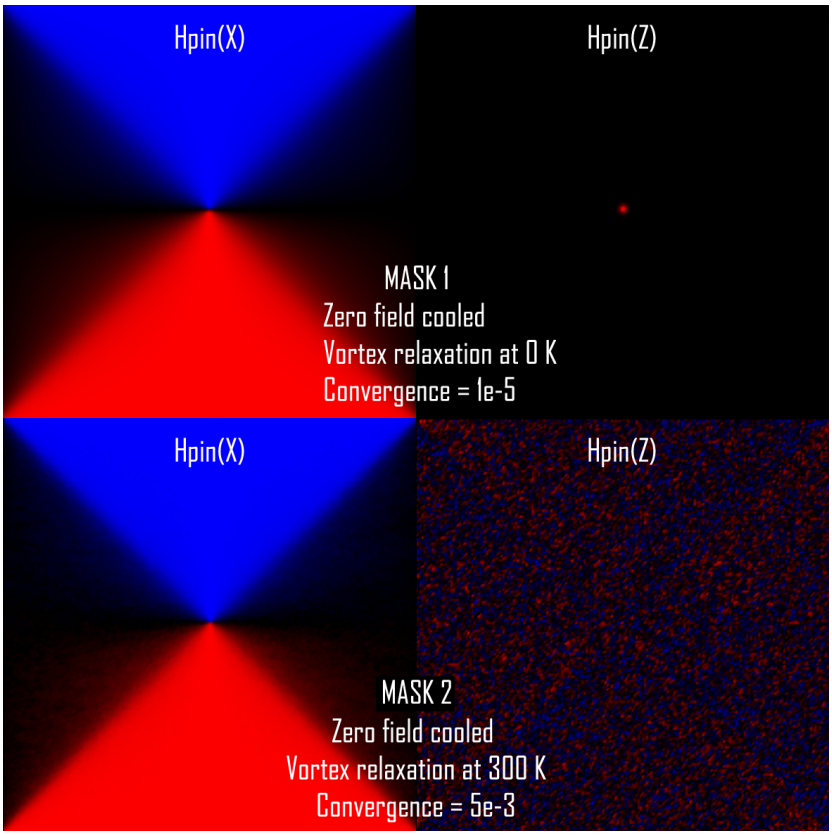

Figure 5.11: Simulated pinning field profiles of G-0 in x and z, demonstrating the addition of random thermal noise. Top: ideal pinning fields in x and z at 0 K. Bottom: random thermal noise corresponding to microstructure imperfection added to the pinning field at 300 K.

5.3 Sample G

5.3.1 Quasi-Static – Unsaturated Cooling Field

The experimental hysteretic behavior of sample G annealed in unsaturated cooling fields (≤ 50 Oe) were shown in Fig. 4.12, Chapter 4. Fig. 5.12 shows the superimposed hysteresis curves for samples G-0 and GREF, both annealed in zero field and support symmetric remanent Landau vortex states.

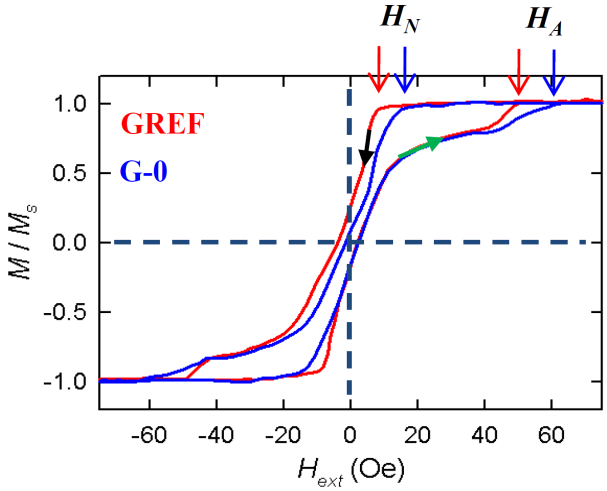

Figure 5.12: G-0 (blue) and GREF (red) hysteresis superimposed.

These exhibit typical features of vortex-mediated hysteresis reversal [37, 38, 39, 40], including:

- A central constriction with low coercivity, corresponding to the low stray fields of the symmetric Landau state at remanence;
- an abrupt change in the hysteresis curve in the descending field branch (black arrow), corresponding to vortex core emergence in the sample at the nucleation field H_N when the sweeping field is decreased from saturation, whereupon the sample magnetization is sharply decreased by the formation of closure domains;
- an abrupt change in the hysteresis curve in the ascending field branch (green arrow), corresponding to vortex core removal in the sample at the annihilation field H_A, whereupon the sample magnetization is sharply increased by the removal of closure domains.

In the ideal case, the fourfold symmetry of the vortex state implies zero coercivity – i.e., a closed and fully reversible central portion. In reality, the imperfection of the square shape and non-negligible FM anisotropy induced during sputter deposition result in a finite remanent magnetization. The effect of exchange bias is evident in Fig. 5.12: H_N and H_A are increased from 8 Oe and 50 Oe in GREF to 15 Oe and 62 Oe in G-0, which indicate enhanced vortex stability. There is also a marked reduction in coercivity in G-0. Both observations agree with previous results obtained for disk

elements [37], and can be explained by noting that the interfacial exchange-bias field in G-0 creates a central 'restoring force' acting on the displaced vortex core during hysteresis, improving vortex stability and quenching the effects of inhomogeneities.

Like in the modeling ($< 150\,\mathrm{Oe}$ in Fig. 5.10), increasing the cooling field above zero expands the bottom domain, leading to an upward displacement of the vortex core and asymmetry in the remanent state (insets of Fig. 4.12). The Rayleigh criterion ((3.4)) limits the resolution to $\geq 1.3\,\mu\mathrm{m}$, and the nanometer-sized vortex cores cannot be resolved, although their details are revealed in the simulation.

Owing to their displaced-vortex remanent states, the hysteresis curves of experimental samples G-15 and G-40 show *asymmetric* loop shifts, modified H_N and H_A values as well as increased coercivities (Fig. 4.12), again in agreement with previous results for disk elements [37, 38, 39]. The exchange-bias field H_{eb} estimated from the loop shift are at 8 Oe and 12 Oe for samples G-15 and G-40 respectively.

The simulation results corresponding to Fig. 4.12 and Fig. 5.12 are shown in Fig. 5.14 and Fig. 5.13. The same label convention is used, e.g., G-75 denotes sample G cooled in 75 Oe cooling field. As previously mentioned, simulated cooling fields are scaled due to sample size reduction in the modelling.

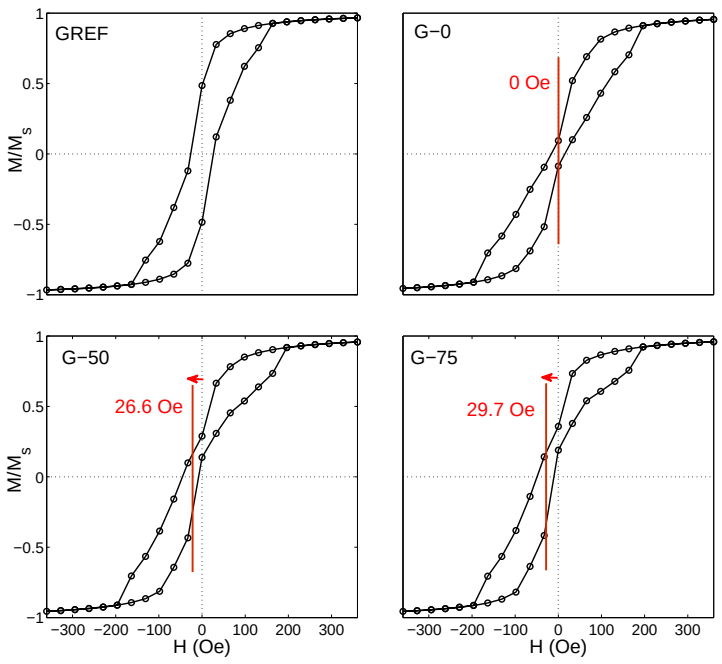

Figure 5.13: Simulated G easy-axis hysteresis with unsaturated cooling fields.

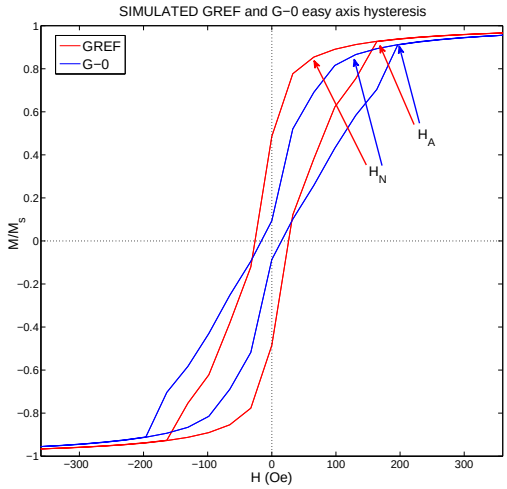

Figure 5.14: Simulated G-0 and GREF hysteresis superimposed.

The experimental features are well-reproduced in the simulations. The effect of the 300 K random thermal noise is illustrated in Fig. 5.15.

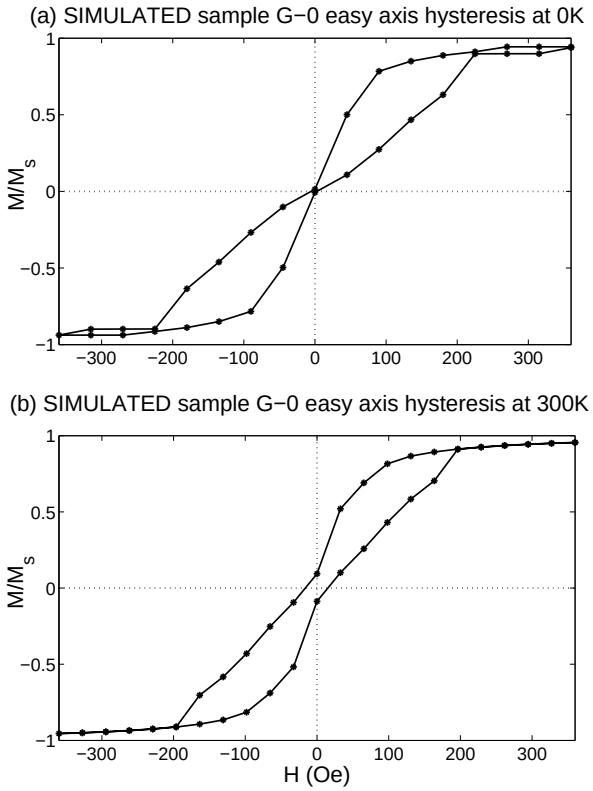

Figure 5.15: Simulated G-0 hysteresis at (a) 0 K (b) 300 K

We see that the coercivity indeed reduces to zero upon removal of the thermal noise (i.e. top pinning field profile in Fig. 5.11) in a system supporting a fourfold-symmetric Landau vortex.

5.3.2 Quasi-Static – Saturated Cooling Field

The hysteretic behavior of sample G annealed in saturated cooling fields ($\geq 50\,\mathrm{Oe}$) were shown in Fig. 4.15, Chapter 4. Like in the modeling ($\geq 150\,\mathrm{Oe}$ in Fig. 5.10), the vortex core is annihilated, and a saturated remanent FM state remains (see Kerr image Fig. 4.16). Consequently, vortex-mediated hysteresis features are no longer observed. Instead, we have a more typical, square-ish hysteresis reversal with prominent easy-axis loop shift along the $-x$ direction. While impossible to see in the experimental scanning Kerr images (Fig. 4.16) due to resolution limits, upon closer inspection of the simulated domain profiles, we see there are regions of inhomogeneous magnetization near the edges perpendicular to the cooling field (dashed lines in Fig. 5.16). These regions are remnants of the original bottom domain walls which are now extended over the length of the sample. Notice the shape of these regions change at very high cooling fields.

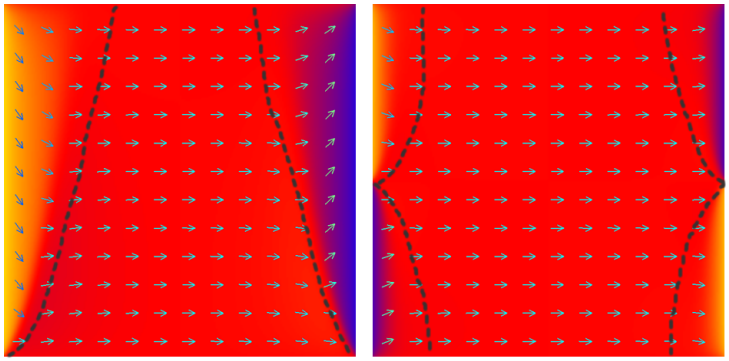

Figure 5.16: Regions of inhomogeneous magnetization in samples annealed in saturated cooling field.

Regions of inhomogeneous fields give rise to slight asymmetry in the otherwise saturated hysteresis loops, observed both experimentally and in simulations. The dynamic significance of these regions of inhomogeneous magnetization will be revealed

later in this chapter. Fig. 5.17 compares typical experimental and simulated results.

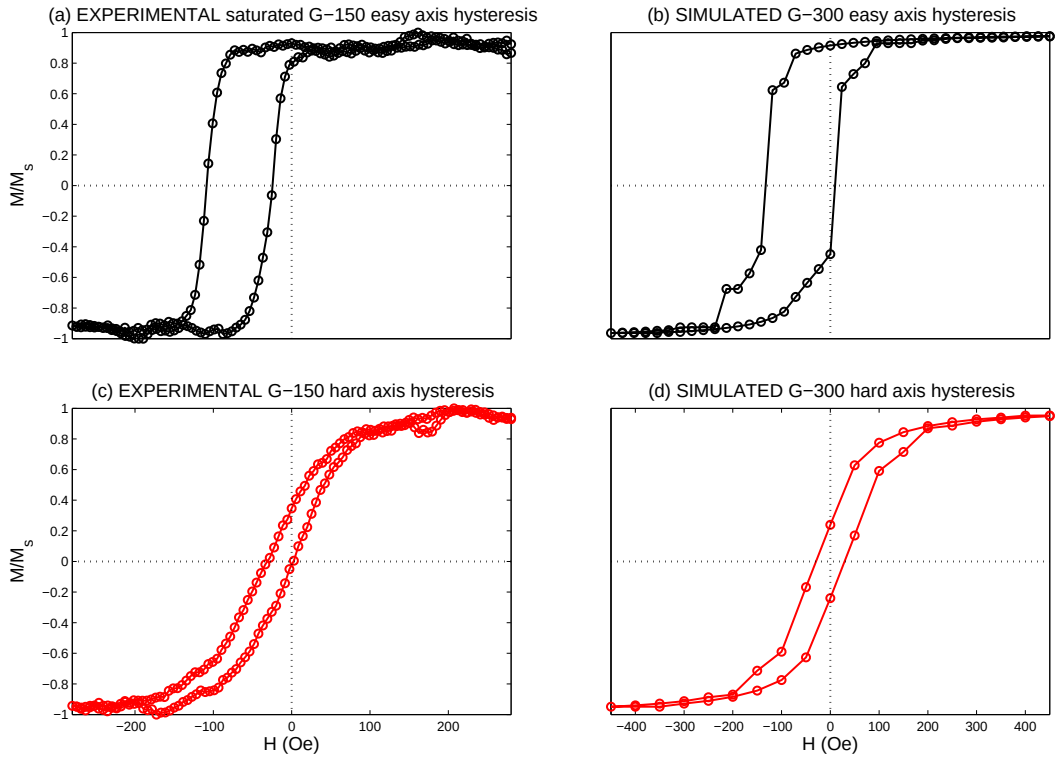

Figure 5.17: Experimental (left) vs. simulated (right) hysteresis for sample G annealed in saturated cooling field.

There is good agreement in both the easy- and hard-axis hysteresis behaviors between experiment and simulation. The slight shift in the experimental hard-axis hysteresis could be due to slightly tilted H_{eb} as a result of imperfect alignment between the sample axis and cooling field.

Summary plots of both experimental and simulated easy-axis hysteresis behavior as functions of cooling fields are presented in Fig. 5.18 and Fig. 5.19 respectively, for all samples annealed in both unsaturated and saturated cooling fields. We see similar trends in coercivity and loop shift variation: gradual increase with increasing cooling field up to saturation, a discontinuous jump at around the vortex annihilation field H_A, and little subsequent changes.

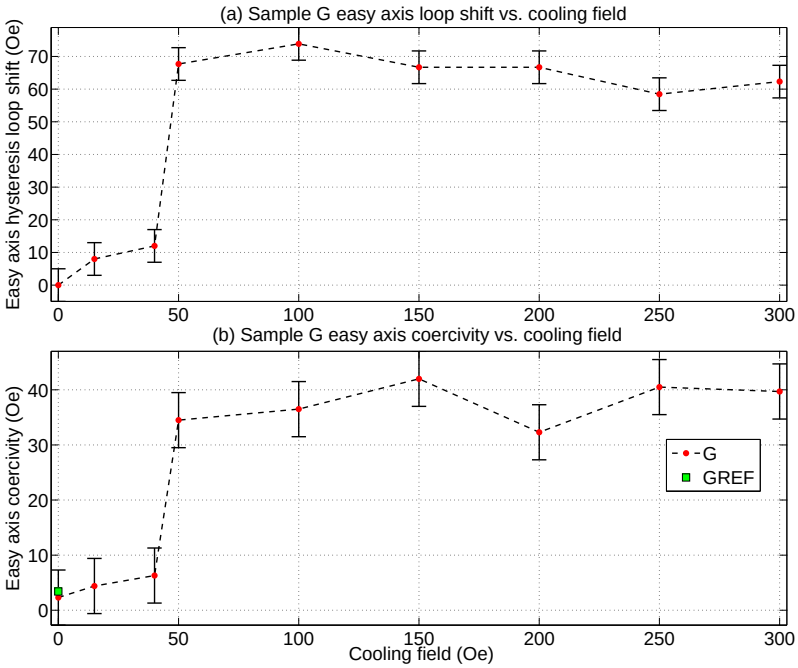

Figure 5.18: Experimental G easy-axis hysteresis behavior as a function of cooling field.

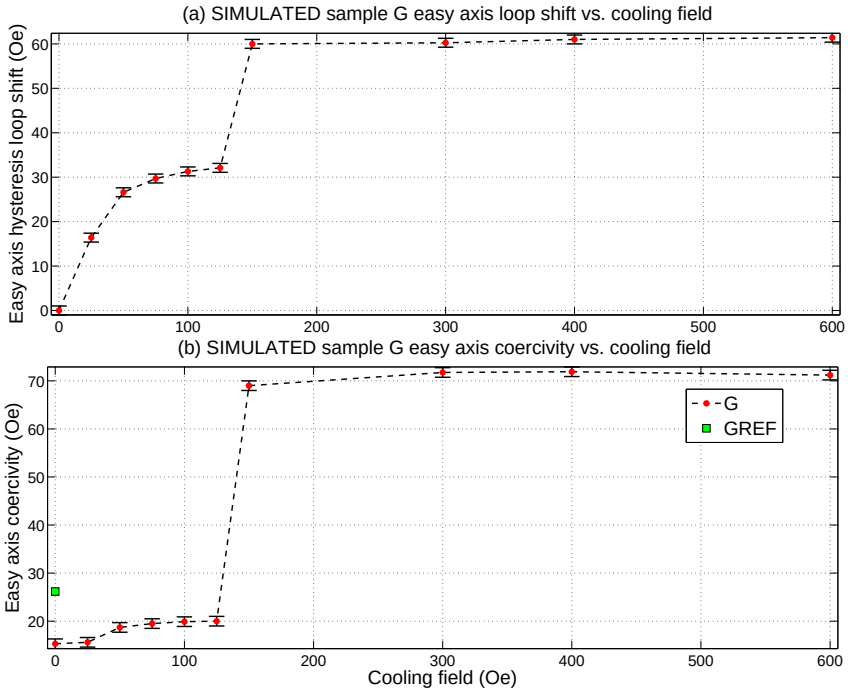

Figure 5.19: Simulated G easy axis hysteresis behavior as a function of cooling field.

So far, we have seen how the exchange-bias field and remanent magnetization can be adjusted through an appropriate cooling field, and how this adjustment modifies quasi-static behavior. In the next section, The dynamic implications of such adjustments will be explored, with a focus on spin-wave eigenmodes.

5.3.3 Spin-Wave Dynamics

Due to its lateral confinement, dynamic excitation of a square element releases stored magnetic energy in the form of quantized spin-wave eigenmodes at various frequencies [14, 69, 70], which have complex dependence on the energies, shape, and remanent state symmetry of the specimen. A rigorous theory of quantized spin-wave modes in Landau domain structures does not exist, but certain features of observed modes can be qualitatively understood based on the Damon-Eshbach theory discussed in Chapter 1 [14]. Numerical modeling is particularly useful in order to bypass resolution limits [68].

First, precessional frequency dependence on cooling field was examined. The experimental (refer to Fig. 4.14) and the corresponding simulated (major) FFT peak frequencies in $M_x(t)$ for samples annealed in unsaturated cooling fields are plotted side by side in Fig. 5.20 as functions of H_{eb}.

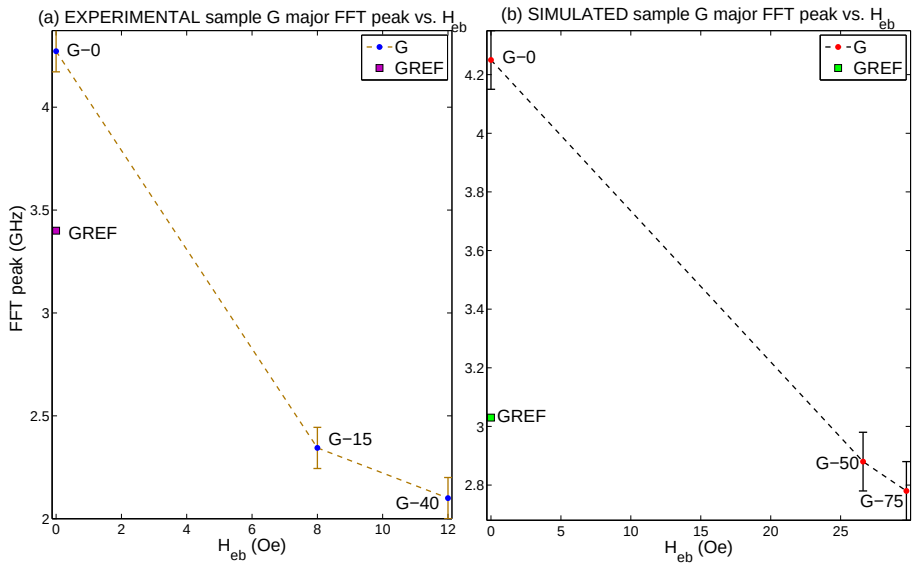

Figure 5.20: Experimental (a) vs. Simulated (b) sample G FFT peak vs. H_{eb}.

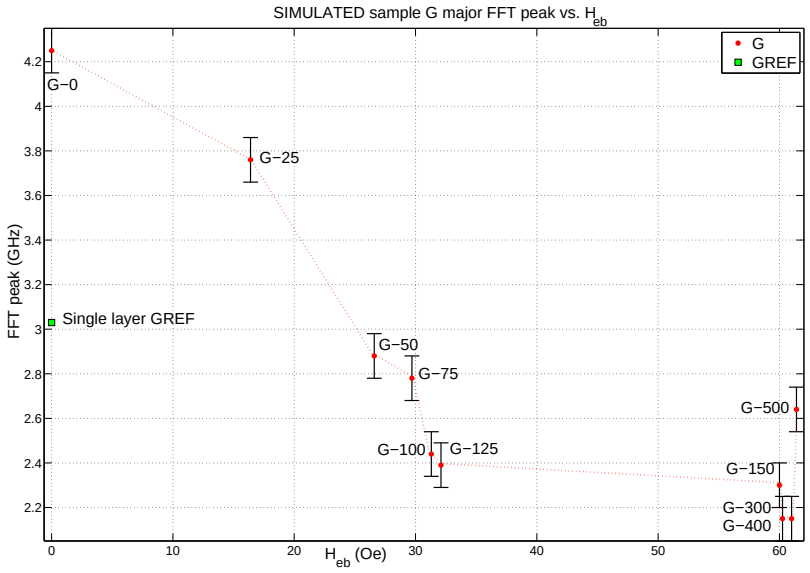

Figure 5.21: Simulated G FFT peak vs. H_{eb}.

In order to understand the physical origins of the observed trends, the spatial distribution of the eigenmode at the major FFT peak frequency (a.k.a. mode frequency) was investigated by plotting the FFT amplitude distribution at the FFT peak frequency over the simulated square for cooling fields between 0 and 1000 Oe, as shown in Fig. 5.22[5]. These were constructed by plotting the modulus of the FFT amplitude A_i of the time-domain magnetization $M_i(t)$ (all 3 components combined) for each unit cell i over the entire simulation grid at the mode frequency [69, 70]. The corresponding cooling field, hysteresis loop shift and mode frequency are shown under each plot for convenience.

[5]These amplitude plots are only approximate representations of the actual eigenmode distribution, the reason being that they are extremely sensitive to frequency variation, and my simulation results have the relatively low frequency resolution of ± 0.1 GHz.

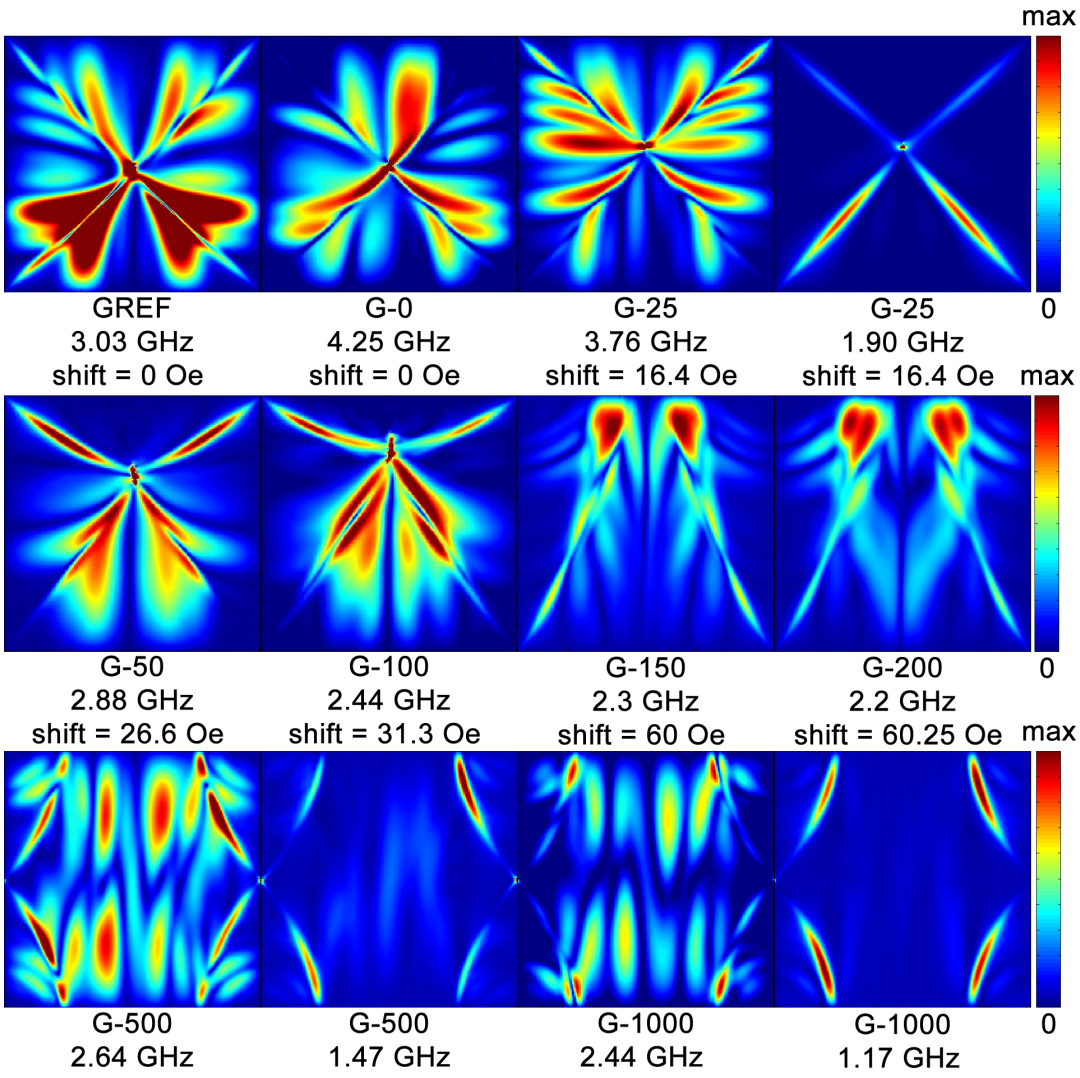

Figure 5.22: FFT amplitude profiles of major eigenmodes in simulated samples subjected to different cooling fields.

Previous simulation studies [15] have shown that spin-wave modes in a square element supporting a fourfold-symmetric Landau state can be broadly classified into three categories with increasing frequency, which are schematically illustrated in Fig. 5.23.

a. Low-frequency modes localized in regions with inhomogeneous magnetization such as the core, the corners and the diagonal domains.

b. Intermediate-frequency modes confined in the domain regions with homogeneous magnetization.

c. High-frequency radial-like and azimuthal-like modes[6], as well as a mixture of both. For these modes, the number of prominent spectral features increase with frequency.

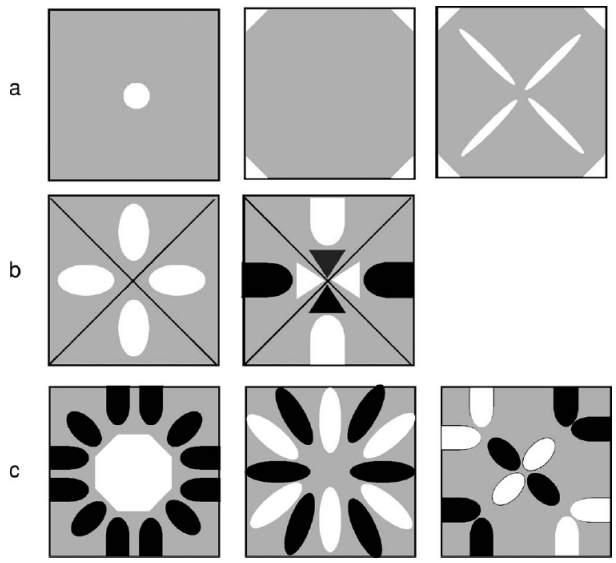

Figure 5.23: Eigenmode classification in square element with remanent Landau state. Black and white indicate regions of different phases while gray represents negligible amplitude. From Yan et al. [15].

Referring to both Fig. 5.22 and Fig. 5.23, we see that simulated samples GREF and G-0 show somewhat similar azimuthal-like modes with spectral features mostly confined within the four quadrant domains. The mode profiles roughly retain the fourfold symmetry of their remanent vortex states, but there is appreciable asymmetry between the modes excited in the top/bottom and left/right quadrants, as a result of the different effective torques on each quadrant due to the different relative orientations between the domain magnetization and the applied excitation pulse. The significant difference between the peak FFT frequencies of GREF and G-0 can be explained as an enhancement in precessional frequency in G-0 due to the additional exchange-bias field H_{eb}, in accordance with the Herring-Kittel formula (1.53).

As the vortex core becomes slightly displaced in sample G-25 (3.76 GHz), the eigenmode exhibits greater asymmetry, and the number of spectral features within each quadrant domain increases. These elongated spectral features are roughly parallel to the domain walls and are reminiscent of the stripe-like standing spin-wave

[6]These are similar to the Damon-Eshbach surface and backward volume modes respectively [15].

mode observed in saturated magnetic squares [71]. A secondary mode, at half the frequency (1.9 GHz) has spin-wave excitation strongly localized in the domain wall regions.

In samples with greater vortex core displacements (G-50, G-100), the major eigenmode is now strongly localized in the domain wall regions, with weak azimuthal-like spectral features appearing in the quadrant domains. The localized domain wall modes are pinned at the corners of the square as well as the vortex core (i.e. nodes at these locations). Since the domain walls bounding the top quadrant are compressed due to vortex core displacement, they are more stable, each showing a single well-defined antinode. On the other hand, the elongation of the lower domain walls due to vortex core displacement result in more complex behavior, and we see the formation of multiple antinodes along their lengths. The observation of multiple antinode formation in domain walls is in agreement with previous studies on permalloy squares supporting vortex magnetization [72].

The modes observed in G-50 and G-100 are extended to the saturated samples G-150 and G-200, where the compressed top domain walls are now completely annihilated by the saturated cooling field, and the major spin-wave mode is now localized in what remains of the original bottom domain walls (dashed lines in Fig. 5.16 left). Multiple antinodes are similarly observed along the lengths of these 'remnant domain wall regions', with a particular concentration of spectral power near the top edge of the square element[7].

Samples with very high cooling fields (G-500, G-1000) show two major mode frequencies corresponding to two different eigenmodes: a lower-frequency mode (G-500 1.47 GHz and G-1000 1.17 GHz) with to spin-wave localization in the 'remnant domain wall regions' (dashed lines in Fig. 5.16 right); and a second mode at roughly double the frequency (G-500 2.64 GHz and G-1000 2.44 GHz) with elongated spectral features parallel to the perpendicular edges of the square over the entire uniformly magnetized central region. The second mode corresponds to the aforementioned standing spin-wave mode in a saturated square element.

The existence of these eigenmodes can be understood as follows. In several samples, we observe strong spatial localization of spin-wave eigenmodes. This type of localization is particular to confined thin-film elements, and has been observed experimentally [14, 22, 73]. Localizations occur in regions with highly inhomogeneous

[7]This corresponds to the large spectral power of the bottom domain wall mode in the vicinity of the vortex core for G-50 and G-100.

internal magnetic fields, such as domain walls in the unsaturated sample G-25 and G-100, and domain wall remnants in the saturated samples G-150 and G-500, as illustrated in Fig. 5.24.

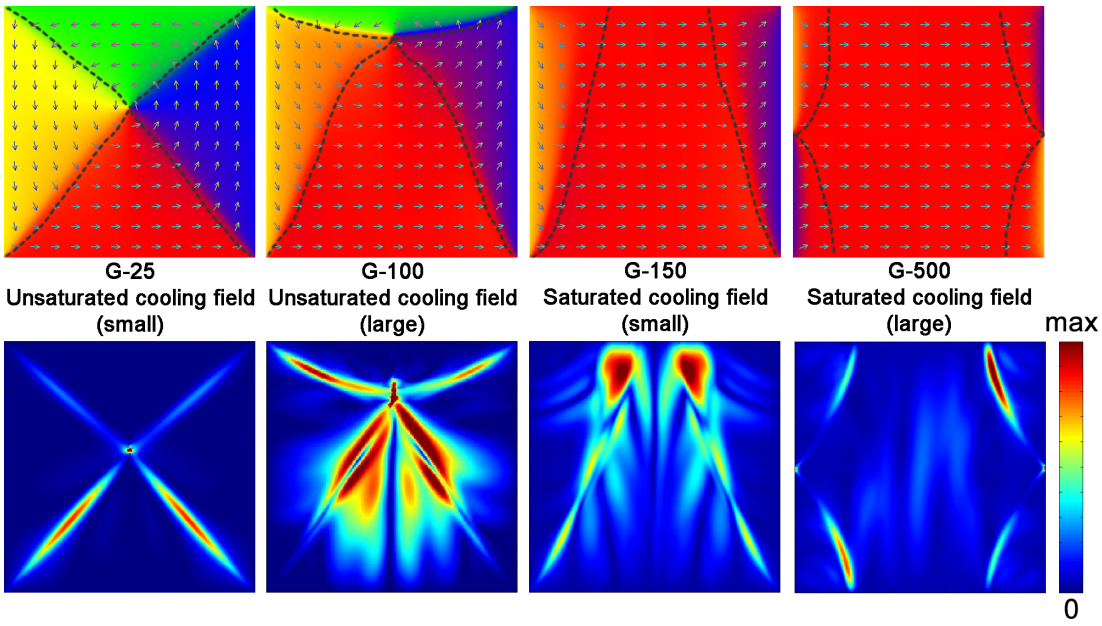

Figure 5.24: Spin-wave localization in regions with inhomogeneous internal fields. Top: remanent domain profiles. Bottom: spin-wave modes.

The inhomogeneous regions (highlighted by dashed lines) form potential wells that 'trap' spin-waves [74]. Furthermore, the highly inhomogeneous nature of the internal magnetic fields in these regions means that the *effective* internal fields in these regions are low, and the modes excited in these regions have low-frequency [14]. This explains the large drop in frequency from the azimuthal-like quadrant domain mode of sample G-25 (3.6 GHz) to the localized domain wall mode of sample G-50 (2.88 GHz) and G-100 (2.44 GHz).

The dashed lines representing domain walls and domain wall remnants in Fig. 5.24 also bound regions with uniform magnetization. Localized oscillations in the domain walls and remnants are therefore expected to strongly influence the formation of spin-wave eigenmodes in these bounded regions [72]. For example, in Fig. 5.22, the observed top/bottom spectral asymmetry of the standing spin-wave mode in the left and right quadrant domains of G-25 (3.76 GHz) is the result of spin-wave excitations by the different oscillations of the top (shorter) and bottom (longer) domain walls that bound the region. In the bottom quadrant, where all temporal measurement were

taken, the lengths of the bounding domain walls increase with increasing cooling fields as the bottom domain expands. This elongation decreases the frequency of the domain wall modes[8], therefore decreasing the measured frequency with increasing cooling field.

Indeed, if the mode frequencies were measured in other domains, as shown in Fig. 5.25, very different results are obtained: sample G-0, with its fourfold symmetric Landau state (left), has equal-sized domains and domain walls. Therefore, the variation of mode frequencies between the quadrant domains is small. In contrast, sample G-100 possesses an asymmetric displaced-vortex state (right), and the mode frequencies measured from the quadrant domains are very different, with a much higher mode frequency found in the top domain confined by shorter domain walls.

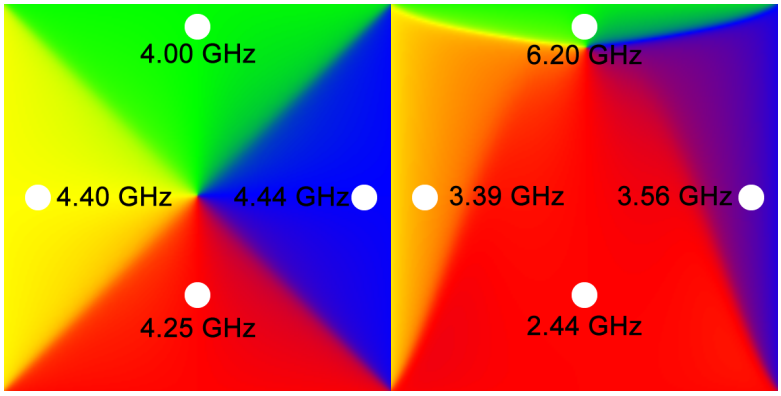

Figure 5.25: Mode frequencies measured over the areas indicated by the white spots in four quadrant domains for G-0 (left) and G-100 (right).

In addition to a localized low-frequency mode, samples G-25, G-500 and G-1000 show a second, standing spin-wave-like mode at roughly double the frequency (see Fig. 5.22). This mode is the result of the frequency-doubling effect of domain wall modes previously reported in Hermsdoerfer et al. [75]. As the domain walls and the domain wall remnants oscillate, they excite spin-waves that propagate throughout the sample. Fig. 5.26 shows both the FFT amplitude (middle and bottom) and phase (top) plots for samples G-25 and G-500. We can clearly see from the phase plots that the regions of spin-wave localization contain antinodes that oscillate in anti-phase to

[8] A complete theoretical description of the dispersion relation in confined magnetic thin films does not exist. However, in general, as feature sizes increase, there will be less exchange and more magnetostatic contribution. And since the former is far stronger over small length scales (i.e. greater stiffness), the characteristic frequency of oscillation is expected to decrease.

each other, hence doubling the effective frequency of the excited spin-waves.

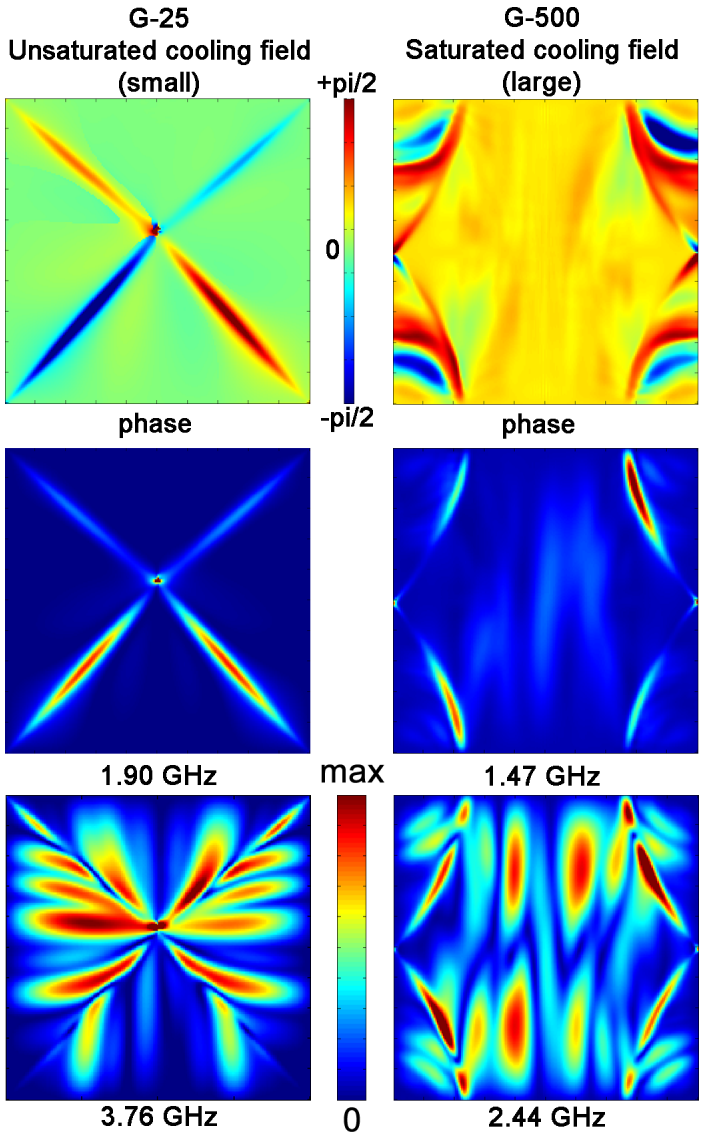

Figure 5.26: Frequency-doubling effect of localized modes. Left: G-25. Right: G-500.

Chapter 6

Conclusions

In this thesis, the quasi-static and dynamic magnetic properties of 10 μm-sized, lithographically patterned FM/AF bilayer squares under varying thermomagnetic annealing conditions using were investigated using MOKE microscopy, XRD and micromagnetic modeling.

It was found that an interfacial exchange-bias field can only be established if the AF layer is deposited on top of the FM layer, which seeds the growth of (111) texture and spin ordering in the AF, which are prerequisites for the establishment of exchange bias.

This exchange-bias field, which closely follows the remanent FM magnetization profile was adjusted through the choice of cooling field. With increasing cooling field, the vortex core in the remanent state was displaced and eventually annihilated, leaving behind a saturated remanent magnetization profile. This adjustment was found to result in an asymmetric shift of the hysteresis loop, quenching improvement of vortex stability and reduction of inhomogeneous effects in the zero-field cooled sample G-0 compared to the reference GREF, as well as an increase in hysteresis loop shift for samples cooled in non-zero cooling fields.

The squares were excited with a 4 ns in-plane magnetic field pulse, and it was found that the addition of exchange-bias in the zero-field cooled sample G-0 significantly increased the precessional frequency in accordance with the Herring-Kittel equation, while subsequent increases in cooling field reduced the precessional frequency measured in the bottom expanding domain.

The details of the dynamic behavior was explored using micromagnetic modeling, in which the effect of the AF layer was represented through a position-dependent pinning field. By looking at the spatial FFT power distribution of spin-wave eigen-

modes, we found that the spin-wave mode excited in a square is strongly influenced by the nature of its domain walls and domain wall remnants. In particular, localized low-frequency spin-wave modes were observed in these regions, and their anti-phase oscillations were found to excite standing spin-waves at double the frequency.

Bibliography

[1] Jian-Gang Zhu, Youfeng Zheng, and Gary A Prinz. Ultrahigh density vertical magnetoresistive random access memory (invited). *Journal of Applied Physics*, 87(9):6668, 2000.

[2] D A Allwood, G Xiong, C C Faulkner, D Atkinson, D Petit, and R P Cowburn. Magnetic domain-wall logic. *Science*, 309(5741):1688–1692, 2005.

[3] G Binasch, P Grünberg, F Saurenbach, and W Zinn. Enhanced magnetoresistance in layered magnetic structures with antiferromagnetic interlayer exchange. *Physical Review B*, 39(7):4828–4830, 1989.

[4] S W Yuan and H N Bertram. Domain-wall dynamics in thick permalloy-films. *Journal of Applied Phys*, 73(10):5992–5994, 1993.

[5] L Landau and E Lifshitz. On the theory of the dispersion of magnetic permeability in ferromagnetic bodies. *Phys Z Sowjetunion*, 8(14):14–22, 1935.

[6] W.F. Brown, Jr. *Micromagnetics*. Interscience Publishers, 1963.

[7] A. Aharoni. *Introduction to the Theory of Ferromagnetism*. Oxford University Press, 2001.

[8] Charles Kittel. Physical theory of ferromagnetic domains. *Reviews of Modern Physics*, 21:541–583, Oct 1949.

[9] Pierre-Ernest Weiss. LHypothese du champ Moleculaire et de la Propriete Ferromagnetique. *J. Phys. Theor. Appl.*, 6:661–690, 1907.

[10] Werner Heisenberg. Zur Theorie der Magnetostriktion und der Magnetisierungskurve. *Z. Phys.*, 69:287–297, 1931.

[11] B. Bandyopadhyay and M. Cahay. *Introduction to Spintronics*. CRC Press, 2008.

[12] M D'Aquino. *Nonlinear magnetization dynamics in thin-films and nanoparticles*. PhD thesis, Universita degli studi di Napoli Federico II, 2004.

[13] J Nogués, J Sort, V Langlais, V Skumryev, S Suriñach, J S Muñoz, and M D Baró. Exchange bias in nanostructures. *Physics Reports*, 422(3):65 – 117, 2005.

[14] Korbinian Perzlmaier, Matthias Buess, Christian H Back, Vladislav E Demidov, Burkard Hillebrands, and Sergej O Demokritov. Spin-wave eigenmodes of permalloy squares with a closure domain structure. *Physical Review Letters*, 94 (5):057202, 2005.

[15] M Yan, G Leaf, H Kaper, R Camley, and M Grimsditch. Spin-wave modes in a cobalt square vortex: Micromagnetic simulations. *Physical Review B*, 73(1):1–7, 2006.

[16] A Hubert and R Schäfer. *Magnetic Domains: The analysis of magnetic microstructures*, volume 24. Springer, 1998. ISBN 9783540641087.

[17] A Wachowiak, J Wiebe, M Bode, O Pietzsch, M Morgenstern, and R Wiesendanger. Direct observation of internal spin structure of magnetic vortex cores. *Science*, 298(5593):577–580, 2002.

[18] Stellan Bohlens, Benjamin Kruger, Andre Drews, Markus Bolte, Guido Meier, and Daniela Pfannkuche. Current controlled random-access memory based on magnetic vortex handedness. *Applied Physics Letters*, 93(14):142508, 2008.

[19] T L Gilbert. A phenomenological theory of damping in ferromagnetic materials, 2004.

[20] Q F Xiao, J Rudge, B C Choi, Y K Hong, and G Donohoe. Dynamics of Vortex Core Switching in Ferromagnetic Nanodisks. *Applied Physics Letters*, 89(26): 262507, 2006.

[21] Q F Xiao, J Rudge, E Girgis, J Kolthammer, B C Choi, Y K Hong, and G W Donohoe. Dynamics of magnetic vortex core switching in Fe nanodisks by applying in-plane magnetic field pulse. *Journal of Applied Physics*, 102(10):103904, 2007.

[22] J P Park, P Eames, D M Engebretson, J Berezovsky, and P A Crowell. Imaging of Spin Dynamics in Closure Domain and Vortex Structures. *Physical Review B*, 67(2):1–4, 2002.

[23] E C Stoner and E P Wohlfarth. A mechanism of magnetic hysteresis in heterogeneous alloys. *Philosophical Transactions of the Royal Society of London Series A Mathematical and Physical Sciences*, 240(826):599–642, 1948.

[24] W.F. Brown, Jr. *Magnetostatic principles in ferromagnetism*, volume 1. North-Holland Publishing Company, 1962.

[25] Dana Elena. *Magnetization Dynamics in Magnetic Nanostructures*. PhD thesis, Université Joseph Fourier, 2004.

[26] R. M. White. *Quantum Theory of Magnetism*. Springer-Verlag, Berlin, 2nd edition, 2007.

[27] Charles Kittel. On the theory of ferromagnetic resonance absorption. *Physical Review*, 73(2):155–161, 1948.

[28] Conyers Herring and Charles Kittel. On the theory of spin waves in ferromagnetic media, 1951.

[29] M.J. Hurben and C.E. Patton. Theory of magnetostatic waves for in-plane magnetized isotropic films. *Journal of Magnetism and Magnetic Materials*, 139(3): 263 – 291, 1995.

[30] M.R. Scheinfein. LLG Micromagnetics Simulator v.2.46, 2009. URL `http://llgmicro.home.mindspring.com/`.

[31] M Ali, C Marrows, M Al-Jawad, B Hickey, A Misra, U Nowak, and K Usadel. Antiferromagnetic layer thickness dependence of the IrMn/Co exchange-bias system. *Physical Review B*, 68(21):1–7, 2003.

[32] W H Meiklejohn and C P Bean. New magnetic anisotropy. *Physical Review*, 105 (3):904–913, 1957.

[33] J Nogués and Ivan K Schuller. Exchange bias. *Journal of Magnetism and Magnetic Materials*, 192(5):203–232, 1999.

[34] H A M Van Den Berg, W Clemens, G Gieres, G Rupp, W Schelter, and M Vieth. Gmr sensor scheme with artificial antiferromagnetic subsystem. *IEEE Transactions on Magnetics*, 32(5):4624–4626, 1996.

[35] S Parkin, Xin Jiang Xin Jiang, C Kaiser, A Panchula, K Roche, and M Samant. Magnetically engineered spintronic sensors and memory, 2003.

[36] B D Terris and T Thomson. Nanofabricated and self-assembled magnetic structures as data storage media. *Journal of Physics D: Applied Physics*, 38(12): R199–R222, 2005.

[37] J Sort, K S Buchanan, V Novosad, A Hoffmann, G Salazar-Alvarez, A Bollero, M D Baró, B Dieny, and J Nogués. Imprinting vortices into antiferromagnets. *Physical Review Letters*, 97(6):067201, 2006.

[38] A Hoffmann, J Sort, K S Buchanan, and J Nogués. Exchange-biased magnetic vortices. *IEEE Transactions on Magnetics*, 44(7):1968–1973, 2008.

[39] M. Tanase, A. K. Petford-Long, O. Heinonen, K. S. Buchanan, J. Sort, and J. Nogués. Magnetization reversal in circularly exchange-biased ferromagnetic disks. *Physics Review B*, 79:014436, 2009.

[40] H Xu, J Kolthammer, J Rudge, E Girgis, B C Choi, Y K Hong, G Abo, Th Speliotis, and D Niarchos. Magnetization process in vortex-imprinted $Ni_{80}Fe_{20}/Ir_{20}Mn_{80}$ square elements. *Journal of Magnetics*, 16(2):83–87, 2011.

[41] R L Stamps. Mechanisms for exchange bias. *Journal of Physics D: Applied Physics*, 33(23):R247–R268, 2000.

[42] Miguel Kiwi. Exchange bias theory. *Journal of Magnetism and Magnetic Materials*, 234(3):584–595, 2001.

[43] S Roy, M R Fitzsimmons, S Park, M Dorn, O Petracic, Igor V Roshchin, Zhi-Pan Li, X Batlle, R Morales, A Misra, X Zhang, K Chesnel, J B Kortright, S K Sinha, and Ivan K Schuller. Depth profile of uncompensated spins in an exchange bias system. *Physical Review Letters*, 95(4):047201, 2005.

[44] A P Malozemoff. Random-field model of exchange anisotropy at rough ferromagnetic-antiferromagnetic interfaces. *Physical Review B*, 35(7):3679–3682, 1987.

[45] A P Malozemoff. Mechanisms of exchange anisotropy (invited). *Journal of Applied Physics*, 63(8):3874–3879, 1988.

[46] A P Malozemoff and J C Slonczewski. *Magnetic domain walls in bubble materials*, volume 1 of *Advances in materials and device research*. Academic Press, 1979.

[47] V. K. Sankaranarayanan, S. M. Yoon, D. Y. Kim, C. O. Kim, and C. G. Kim. Exchange bias in NiFe/FeMn/NiFe trilayers. *Journal of Applied Physics*, 96(12): 7428, 2004.

[48] J Martín. Ordered magnetic nanostructures: fabrication and properties. *Journal of Magnetism and Magnetic Materials*, 256(1-3):449–501, 2003.

[49] C Lu, A W Czanderna, and Alan Townshend. Applications of piezoelectric quartz crystal microbalances. *Analytica Chimica Acta*, 199(0):279, 1987.

[50] Norbert Kaiser. Review of the fundamentals of thin-film growth. *Applied Optics*, 41(16):3053–3060, 2002.

[51] J Kerr. On rotation of the plane of polarization by reflection from the pole of a magnet. *Philosophical Magazine*, 3(19):321, 1877.

[52] Gustav Bihlmayer. *Handbook of Magnetism and Advanced Magnetic Materials III*, volume 320. Wiley, 2007.

[53] S.B. Palmer and M.S. Rogalski. *Advanced University Physics*. Gordon and Breach Publishers, 1996.

[54] H J Williams, F G Foster, and E A Wood. Observation of Magnetic Domains by the Kerr Effect. *Physical Review*, 82(1):119–120, 1951.

[55] B.C. Choi and M.R. Freeman. *Ultrathin Magnetic Structures III*. Springer, 2005.

[56] M.R. Freeman, R.R. Ruf, and J. Gambino, R. Picosecond Pulsed Magnetic Fields for Studies of Ultrafast Magnetic Phenomena. *IEEE Transactions on Magnetics*, (6):4840, 1991.

[57] W L Roth. Magnetic Structures of MnO, FeO, CoO, and NiO. *Physical Review*, 110(6):1333–1341, 1958.

[58] B D Cullity and S R Stock. *Elements of X-Ray Diffraction*. Addison-Wesley series in metallurgy and materials. Prentice Hall, 2001.

[59] Jodi Liu, Robert E Saw, and Y-H Kiang. Calculation of effective penetration depth in X-ray diffraction for pharmaceutical solids. *Journal of Pharmaceutical Sciences*, 99(9):3807–3814, 2010.

[60] Geoff Anderson, Yiming Huai, and Lena Miloslawsky. Cofe/irmn exchange biased top, bottom, and dual spin valves. *Journal of Applied Physics*, 87(9):6989, 2000.

[61] J. van Driel, F. R. de Boer, K.-M. H. Lenssen, and R. Coehoorn. Exchange biasing by $Ir_{19}Mn_{81}$: dependence on temperature, microstructure and antiferromagnetic layer thickness. *Journal of Applied Physics*, 88(2):975, 2000.

[62] A J Devasahayam, P J Sides, and M H Kryder. Magnetic, temperature, and corrosion properties of the NiFe/IrMn exchange couple. *Journal of Applied Physics*, 83(11):7216, 1998.

[63] Marian Fecioru-Morariu, Gernot Guntherodt, Manfred Ruhrig, Alessio Lamperti, and Brian Tanner. Exchange coupling between an amorphous ferromagnet and a crystalline antiferromagnet. *Journal of Applied Physics*, 102(5):053911, 2007.

[64] G Malinowski, M Hehn, S Robert, O Lenoble, A Schuhl, and P Panissod. Magnetic origin of enhanced top exchange biasing in py/irmn/py multilayers. *Physical Review B*, 68(18):1–8, 2003.

[65] Himanshu Fulara, Sujeet Chaudhary, Subhash C Kashyap, and Dinesh K Pandya. Positive exchange bias in as-deposited ion-beam sputtered irmncofeb system. *Journal of Applied Physics*, 110(9):093916, 2011.

[66] A L Patterson. The Scherrer formula for X-ray particle size determination. *Physical Review*, 56(10):978–982, 1939.

[67] H S Jung, W D Doyle, and S Matsunuma. Influence of underlayers on the soft properties of high magnetization feco films. *Journal of Applied Physics*, 93(10): 6462, 2003.

[68] H Xu, E Girgis, J Rudge, Th Speliotis, C A Ross, H Miyagawa, Y K Hong, and B C Choi. Magnetization dynamics in vortex-imprinted $Ni_{80}Fe_{20}/Ir_{20}Mn_{80}$ square elements. *IEEE Magnetics Letters*, 3:3500204–3500207, 2012.

[69] M Buess, R Höllinger, T Haug, K Perzlmaier, U Krey, D Pescia, M R Scheinfein, D Weiss, and C H Back. Fourier transform imaging of spin vortex eigenmodes. *Physical Review Letters*, 93(7):077207, 2004.

[70] C.H. Back, D. Pescia, and M. Buess. *Chapter "Vortex Dynamics", Spin Dynamics in Confined Magnetic Structures III*, volume 9 of *Topics in Applied Physics*. Springer, 2006. ISBN 9783540201083.

[71] B C Choi, M Belov, W K Hiebert, G E Ballentine, and M R Freeman. Ultrafast magnetization reversal dynamics investigated by time domain imaging. *Physical Review Letters*, 86(4):728–731, 2001.

[72] M Bailleul, R Höllinger, K Perzlmaier, and C Fermon. Microwave spectrum of square permalloy dots: Multidomain state. *Physical Review B*, 76(22):1–14, 2007.

[73] A Barman, V V Kruglyak, R J Hicken, J M Rowe, A Kundrotaite, J Scott, and M Rahman. Imaging the dephasing of spin wave modes in a square thin film magnetic element. *Physical Review B*, 69(17):1–5, 2004.

[74] J Jorzick, S O Demokritov, B Hillebrands, M Bailleul, C Fermon, K Y Guslienko, A N Slavin, D V Berkov, and N L Gorn. Spin wave wells in nonellipsoidal micrometer size magnetic elements. *Physical Review Letters*, 88(4):047204, 2002.

[75] Sebastian J Hermsdoerfer, Helmut Schultheiss, Christopher Rausch, Sebastian Schaefer, Britta Leven, Sang-Koog Kim, and Burkard Hillebrands. A spin-wave frequency doubler by domain wall oscillation. *Applied Physics Letters*, 94(22):8, 2009.

[76] W Pauli. The Connection Between Spin and Statistics. *Physical Review*, 58(8): 716–722, 1940.

[77] Michiel Hazewinkel. *"Determinan", Encyclopedia of Mathematics*. Springer, 2001.

[78] R S Mulliken. Spectroscopy, molecular orbitals, and chemical bonding. *Science*, 157(784):13–24, 1967.

[79] M. A. Ruderman and C. Kittel. Indirect exchange coupling of nuclear magnetic moments by conduction electrons. *Physics Review*, 96:99–102, Oct 1954.

Appendix A

The Hartree-Fock Method

Exchange interaction arises from the exchange symmetry of wavefunctions of identical particles. The notion of exchange symmetry is based on the fact that no physical observable should change after identical particles undergo spatial exchange. If the spatial part of the total wavefunction of two identical particles is $\Psi(\mathbf{r}_1, \mathbf{r}_2)$, exchange symmetry implies

$$|\Psi(\mathbf{r}_1\mathbf{r}_2)|^2 = |\Psi(\mathbf{r}_2\mathbf{r}_1)|^2, \tag{A.1}$$

hence

$$\begin{aligned} e^{i\theta}\Psi(\mathbf{r}_1\mathbf{r}_2) &= \Psi(\mathbf{r}_2\mathbf{r}_1) \\ \text{and} \quad \Psi(\mathbf{r}_1\mathbf{r}_2) &= e^{i\theta}\Psi(\mathbf{r}_2\mathbf{r}_1) \\ \Rightarrow e^{2i\theta} &= 1, \end{aligned} \tag{A.2}$$

with two possibilities:

$$e^{i\theta} = \begin{cases} 1 & \text{spatial wavefunction symmetric on particle exchange, boson,} \\ -1 & \text{spatial wavefunction anti-symmetric on particle exchange, fermion.} \end{cases}$$

Spin statistics theorem demands that particles with $\frac{1}{2}$ integer spin such as electrons behave as fermions [76].

The origin of exchange interaction can be demonstrated for a system with N va-

lence electrons under the Hartree-Fock approximation. Assume all electrons have an identical set of orthonormal eigenfunctions (φ) with orthonormal spatial (ϕ) and spinor (η) component eigenstates (i.e., ignore spin-orbit coupling). For the j^{th} electron:

$$\varphi_j(\boldsymbol{\rho}_j) = \phi(\boldsymbol{r}_j)\eta(s_j), \tag{A.3}$$

The overall eigenfunction Ψ can be built from individual $\varphi_i(\boldsymbol{\rho}_j)$. The *Slater determinant* can be used to give the simplest N-body wavefunction that satisfies exchange symmetry under the Hartree-Fock approximation:

$$\Psi = \frac{\det[\varphi_k]}{\sqrt{N!}}, \tag{A.4}$$

where

$$\det[\varphi_k] = \det \begin{bmatrix} \varphi_1(\boldsymbol{\rho}_1) & \cdots & \varphi_1(\boldsymbol{\rho}_N) \\ \vdots & \ddots & \vdots \\ \varphi_N(\boldsymbol{\rho}_1) & \cdots & \varphi_N(\boldsymbol{\rho}_N). \end{bmatrix} \tag{A.5}$$

The Hamiltonian is given by

$$\begin{aligned} H &= \sum_N (-\frac{1}{2m_e}\nabla_i^2 + V_i) + \frac{1}{2}\sum_{N,i\neq j}\frac{e^2}{r_{ij}} + H_c \\ &= \sum_N H_i + \frac{1}{2}\sum_{N,i\neq j} H_{ij} + H_c, \end{aligned} \tag{A.6}$$

where V_i is the total potential of the inner electrons and nuclei at the i^{th} valence electron, r_{ij} is the distance between valence electrons i and j, H_c is the Hamiltonian operating on ion cores, henceforth omitted.

The expectation value of energy is given by the standard integral

$$
\begin{aligned}
E = \langle\Psi|H|\Psi\rangle &= \frac{1}{N!}\int \det[\varphi^*_{k'}] H \det[\varphi_k]\,\mathrm{d}\tau_1 \ldots \mathrm{d}\tau_N \\
&= \frac{1}{N!}\int \det[\varphi^*_{k'}]\Big(\sum_N H_i\Big)\det[\varphi_k]\,\mathrm{d}\tau_1 \ldots \mathrm{d}\tau_N \\
&+ \frac{1}{N!}\int \det[\varphi^*_{k'}]\Big(\frac{1}{2}\sum_{N,i\neq j} H_{ij}\Big)\det[\varphi_k]\,\mathrm{d}\tau_1 \ldots \mathrm{d}\tau_N \\
&= \frac{1}{N!}\int \sum_N E_i + \frac{1}{N!}\int \frac{1}{2}\sum_{N,i\neq j} E_{ij}. \qquad \text{(A.7)}
\end{aligned}
$$

The origin of exchange interaction can now be explored using this construct. Consider the two energy terms in (A.7). Using the Leibniz formula for determinants [77] and invoking orthonormality conditions, one can show that they simplify into

$$
\begin{aligned}
E &= \sum_N E_i + \frac{1}{2}\sum_{N,i\neq j} E_{ij} \\
&= \sum_{N,k}\int \varphi^*_k(\boldsymbol{\rho}_1) H_1 \varphi_k(\boldsymbol{\rho}_1)\,\mathrm{d}\tau_1 \\
&+ \frac{1}{2}\sum_{N,k\neq k'}\int |\phi_k(\mathbf{r}_1)|^2 \frac{e^2}{r_{12}} |\phi_{k'}(\mathbf{r}_2)|^2\,\mathrm{d}\mathbf{r}_1\mathrm{d}\mathbf{r}_2 \\
&- \frac{1}{2}\sum_{N,k\neq k'}\int \varphi^*_k(\boldsymbol{\rho}_1)\varphi_k(\boldsymbol{\rho}_2)\frac{e^2}{r_{12}}\varphi^*_{k'}(\boldsymbol{\rho}_2)\varphi_{k'}(\boldsymbol{\rho}_1)\,\mathrm{d}\tau_1\mathrm{d}\tau_2. \qquad \text{(A.8)}
\end{aligned}
$$

The first term in (A.8) is simply the total energy of the N individual electrons in isolation. The second term in (A.8) also easily justifiable, it is the total Coulomb repulsion between electron pairs. The third term however, has no classical interpretation. It emerges out of the Coulomb potential as a consequence of the exchange anti-symmetry property of our particular choice of total eigenfunction. We can regard this term as a quantum mechanical correction to the classical Coulomb interaction for a system of fermions. This quantum mechanical correction is otherwise known as the **exchange interaction**.

The integral in the exchange interaction term in (A.8) contains summation over all orthogonal spin eigenfunctions and vanishes unless if the spins are parallel or anti-parallel. The exchange energy term therefore represents the energy difference

between states of parallel and anti-parallel spins. The effective Hamiltonian, $\mathcal{H}_{\text{ex}}$ of the exchange interaction energy term contains terms proportional to $\mathbf{s}_i \cdot \mathbf{s}_j$, where $\mathbf{s}_i$ is the vector spin operator of the i^{th} electron.

For a simple 2-electron Helium atom, it can be shown that $\mathcal{H}_{\text{ex}}$ takes the form [11]

$$\mathcal{H}_{\text{ex}} = -2J_{12}\,\mathbf{s}_1 \cdot \mathbf{s}_2. \tag{A.9}$$

where J_{12} is some property of the Helium atom. Heisenberg proposed an intuitive generalization of (A.9) for a crystal lattice, known as the **Heisenberg Hamiltonian**

$$\mathcal{H}_{\text{ex}} = -\sum_{k \neq k'} J_{kk'} \mathbf{S}_{\mathbf{k}} \cdot \mathbf{S}_{\mathbf{k}'}, \tag{A.10}$$

where atom situated at a lattice site $\mathbf{k}$ has total unpaired electron spin quantum number S_k. J_{ij} is known as the *exchange integral*, its expression found by extracting the spatial part of the exchange interaction term in (A.8):

$$J_{kk'} = \int \phi_k^*(\boldsymbol{r}_1)\phi_k(\boldsymbol{r}_2)\frac{e^2}{r_{12}}\phi_{k'}^*(\boldsymbol{r}_2)\phi_{k'}(\boldsymbol{r}_1)\,\mathrm{d}\mathbf{r}_1\mathrm{d}\mathbf{r}_2. \tag{A.11}$$

As the effect of exchange interaction decays rapidly with distance due to decreasing wavefunction overlap, it is usually sufficient in practice to consider only interactions between nearest neighbors. Assuming isotropy lattice, the *nearest neighbour exchange integral* (referred to as J throughout my thesis) is index-independent and can be extracted from the summation:

$$\mathcal{H}_{\text{ex}} = -J \sum_{k \neq k'} \mathbf{S}_{\mathbf{k}} \cdot \mathbf{S}_{\mathbf{k}'}. \tag{A.12}$$

$\mathcal{H}_{\text{ex}}$ can be regarded as a first order approximation to the exact Hamiltonian, with the next term in the expansion containing terms proportional to $(\mathbf{S}_{\mathbf{k}} \cdot \mathbf{S}_{\mathbf{k}'})^2$.

The Heisenberg Hamiltonian assumes electron localization in the context of the Heitler-London model. It is not applicable to metallic conductors such as Fe, Ni and Co in which the $3d$ electrons responsible for ferromagnetism are itinerant. In these materials, the delocalized molecular orbital model [78] is employed, and the Ruderman-Kittel-Kasuya-Yosida [79] indirect exchange mechanism is considered.

Appendix B

Parameters and Equipments List

Parameter	**Value**
Layer 1 resist	495 PMMA 6% in anisole 4000 rpm, thickness $\simeq 300$ nm
Layer 2 resist	950 PMMA 4% in anisole 4000 rpm, thickness $\simeq 200$ nm
Pre-bake temperature	~ 170°C
EBL vacuum	3.92×10^{-6} Torr
Electron acceleration voltage	30 kV
EBL Probe current	< 0.1 nA
EBL Write current	$\simeq 0.6$ nA

Table B.1: EBL patterning parameters.

Parameter	**Value**
Initial base pressure	$1.0 - 2.0 \times 10^{-7}$ Torr
Deposition base pressure	$1.0 - 2.0 \times 10^{-6}$ Torr
Gold microcoil thickness and deposition rate	1000 Åand 1 Å/s
Chrome adhesion layer thickness and deposition rate	30 Åand 1 Å/s
Electron acceleration voltage	25 kV

Table B.2: Electron beam evaporation parameters.

Parameter	**Value**
Base pressure	5×10^{-8} Torr
Sputtering gas and pressure	Argon at 3×10^{-3} Torr
Substrate temperature	room temperature
Target to substrate distance	12 cm
Ferromagnet deposition rate	3.3 Å/s
Antiferromagnet deposition rate	2.9 Å/s
Magnetron power density for ferromagnet deposition	1.5 w/cm^2
Magnetron power density for anti-ferromagnet deposition	0.5 w/cm^2
Magnetron stray field at substrate position	0.2-0.3 Oe

Table B.3: Magnetron sputter deposition parameters.

Name	**Manufacture**	**Notes**
Objective lens	Olympus	10×, 10.6 mm W.D., N.A. = 0.25, spot size $\geq 30\,\mu$m
All optical bench stuff	Thor Labs	
Polarizer / Analyzer	Thor Labs	Glan-Thompson prism
Helium-Neon Laser	Uniphase	10 mW, 632.8 nm
Lock-in amplifier	Stanford Research Systems SR830	
Low noise preamplifier	Stanford Research Systems SR560	
Lens	Thor Labs	various focal lengths
Ti:Sapphire pulse laser (Tsunami)	Spectra Physics Model 3941	780 nm, 80 fs, 80 MHz
Pulse selector	Spectra Physics Model 3980	
Pulse generator	Picosecond pulse labs 2600C	
Objective lens	Olympus	80×, 4.1 mm WD, N.A. = 0.75, spot size $\geq 30\,\mu$m
Polarizing beam splitter	Thor Labs	Wollaston prism
Electromagnet	Home-made ferrite core	$\simeq 0.1$ Hz, $\pm$280 Oe sweeping field
Power supply	KEPCO Bipolar power supply	$\pm$4 A, $\pm$50 V
Data Acquisition and control	Ni-DAQ, LabView, NI BNC-2120	

Table B.4: MOKE equipment list.

Appendix C

Magnetic Field Pulse Calculation

Assume the gold coil can be approximated by an infinitely rectangular wire of width w, height h, length L along the y axis ($L \gg$ other dimensions) carrying a uniform current density of

$$J = \frac{I}{wh}. \tag{C.1}$$

We can calculate the current-induced magnetic field around the coil through simple application of the Biot-Savart law, taking into account the rectangular geometry.

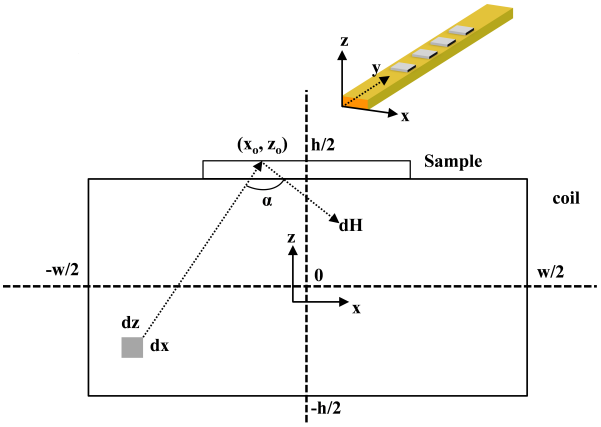

Figure C.1: Magnetic field from current-carrying rectangular coil.

For infinite thin wire carrying current I, the magnetic field H (A/m) at a distance r from the wire is given by

$$H = \frac{I}{2\pi r}. \tag{C.2}$$

Fig. C.1 shows a cross-section of the rectangular wire in the $x-z$ plane. An infinitesimal section of the wire with cross-section area $\mathrm{d}x\mathrm{d}z$ contributes $\mathrm{d}H$ to the overall magnetic field at point (x_o, z_o) on top of the sample (z_o is fixed), which, according to the Biot-Savart law, can be written as

$$\begin{aligned} \mathrm{d}H_x &= \frac{J}{2\pi r}\sin\alpha\,\mathrm{d}x\mathrm{d}z \\ \mathrm{d}H_z &= \frac{-J}{2\pi r}\cos\alpha\,\mathrm{d}x\mathrm{d}z. \end{aligned} \tag{C.3}$$

We can define

$$\begin{aligned} r &= \sqrt{(x-x_o)^2+(z-z_o)^2} \\ \sin\alpha &= \frac{z-z_o}{r} \\ \cos\alpha &= \frac{x_o-x}{r}. \end{aligned} \tag{C.4}$$

The x and z components of the total magnetic field at (x_o, z_o) can now be found by integrating (C.3)

$$\begin{aligned} H_x &= \frac{J}{2\pi}\iint_{x,z=\frac{-w}{2},\frac{-h}{2}}^{x,z=\frac{w}{2},\frac{h}{2}} \frac{z_o-z}{(x-x_o)^2+(z-z_o)^2}\,\mathrm{d}x\mathrm{d}z \\ H_z &= \frac{-J}{2\pi}\iint_{x,z=\frac{-w}{2},\frac{-h}{2}}^{x,z=\frac{w}{2},\frac{h}{2}} \frac{x_o-z}{(x-x_o)^2+(z-z_o)^2}\,\mathrm{d}x\mathrm{d}z. \end{aligned} \tag{C.5}$$

Theoretically, we should calculate the contributions from *both* coils in parallel (see Fig. 3.12), but since each sample square is located directly on top of one coil, the contribution from the second coil is negligibly small. Integrating (C.5) once, we get

$$\begin{aligned} H_x &= \frac{J}{4\pi}\int_{x=\frac{-w}{2}}^{x=\frac{w}{2}} ln\Big((z_o+\frac{h}{2})^2+(x-x_o)^2\Big) - ln\Big((z_o-\frac{h}{2})^2+(x-x_o)^2\Big)\mathrm{d}x \\ H_z &= \frac{J}{4\pi}\int_{z=\frac{-h}{2}}^{z=\frac{h}{2}} ln\Big((x_o-\frac{w}{2})^2+(z-z_o)^2\Big) - ln\Big((x_o+\frac{w}{2})^2+(z-z_o)^2\Big)\mathrm{d}z. \end{aligned} \tag{C.6}$$

(C.6) can be integrated numerically in MatLab using the simple trapezoidal method with 2000 divisions, along with experimental parameters. The results are summarized in Tab. C.1.

Parameter	Value
Coil width w	$20\,\mu$m
coil thickness h	100 nm
Sample thickness $z_o - h/2$	25 nm
Sample width	$10\,\mu$m
Applied voltagpe	45 V
Sample S1-100 resistance	$60.9\,\Omega$
Sample S1-150 resistance	$56.1\,\Omega$
Sample S1-200 resistance	$54.6\,\Omega$
Sample S1-100 H_x	231 Oe
Sample S1-150 H_x	250.8 Oe
Sample S1-200 H_x	257.7 Oe

Table C.1: Field calculation parameters.

The field plots in Fig. C.2 show uniform H_x across the microcoil width.

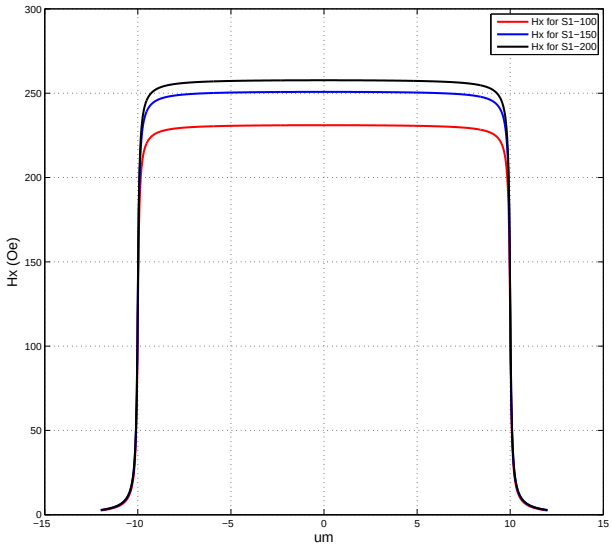

Figure C.2: H_x profile.